DESIGN AND SIMULATION OF A DC ELECTRIC VEHICLE CHARGING STATION INTERCONNECTED WITH A MVDC NETWORK

by

Adam Richard Sparacino

B.S. in Electrical Engineering, University of Pittsburgh, 2011

Submitted to the Graduate Faculty of

Swanson School of Engineering in partial fulfillment

of the requirements for the degree of

Master of Science

University of Pittsburgh

2012

UNIVERSITY OF PITTSBURGH

SWANSON SCHOOL OF ENGINEERING

This thesis was presented

by

Adam Richard Sparacino

It was defended on

November 6, 2012

and approved by

Gregory F. Reed, PhD, Associate Professor, Electrical and Computer Engineering Department

George Kusic, PhD, Associate Professor, Electrical and Computer Engineering

Zhi-Hong Mao, PhD, Associate Professor, Electrical and Computer Engineering

Thesis Advisor: Gregory F. Reed, PhD, Associate Professor, Electrical and Computer Engineering Department

DESIGN AND SIMULATION OF A DC ELECTRIC VEHICLE CHARGING STATION INTERCONNECTED WITH A MVDC NETWORK

Adam Sparacino, M.S.

University of Pittsburgh, 2012

Due to a rapidly aging electric transmission and distribution infrastructure, an increased demand for energy, an increased awareness of climate change and greenhouse gas pollution, and an increased cost of fuel there is a need to produce and deliver energy more efficiently. This thesis attempts to provide a solution to these constraints through advancements in DC power architectures.

Medium Voltage Direct Current (MVDC) infrastructure serves as a platform for the interconnection of renewable electric power generation, including wind and solar. Abundant loads such as industrial facilities, data centers, commercial office buildings, industrial parks, and electric vehicle charging stations (EVCS) can also be powered using MVDC technology. MVDC networks are expected to improve efficiency, through reductions in power electronic conversion steps and by serving as an additional layer between the transmission and distribution level voltage for which generation sources and loads could directly interface with smaller rated power conversion equipment.

This thesis provides an introduction to battery energy storage system technology, and primarily investigates an EVCS powered via a MVDC bus. A bidirectional DC-DC converter with appropriate controls serves as the interface between the EVCS and the MVDC bus. Two scenarios are investigated for testing and comparing EVCS operation: 1) EVCS power supplied by the interconnected MVDC model and 2) EVCS power supplied by an equivalent voltage source. The ability of the battery charger (synchronous buck converter) to isolate faults in next generation DC power systems is explored. Each of the investigated components is modeled and simulated utilizing the PSCAD simulation environment then analytically validated.

TABLE OF CONTENTS

ACKNOWLEDGEMENTS 13

1.0 INTRODUCTION 1

  1.1 MEDIUM VOLTAGE DC NETWORK 2

  1.2 ELECTRIC VEHICLE CHARGING STATION 3

  1.3 PROBLEM STATEMENT AND MOTIVATION 4

  1.4 ORGANIZATION OF DOCUMENT 5

2.0 BATTERY ENERGY STORAGE SYSTEMS 7

  2.1 SURVEY OF BATTERY ENERGY STORAGE SYSTEM TECHNOLOGIES 9

  2.2 BATTERY MODELING 13

    2.2.1 Electrochemical Models 14

    2.2.2 Equivalent Circuit Models 16

3.0 SYSTEM LAYOUT AND DESIGN 18

  3.1 MVDC NETWORK 19

    3.1.1 Wind Power Generation Model Development 19

    3.1.2 Three Level NPC Converter 21

    3.1.3 Industrial Facility 23

  3.2 EV CHARGING STATION 24

    3.2.1 Design Criteria for the EV Charging Station 25

3.2.2 Bidirectional DC-DC Converter 27

3.2.3 Synchronous Buck Converter 36

3.2.4 Electric Vehicle Linear Battery Model 38

3.2.5 Photovoltaic Array and Boost Converter 41

4.0 PSCAD COMPONENT VALIDATION 45

4.1 MVDC SYSTEM COMPONENT VALIDATION 45

4.1.1 5 MW PMSG Wind Turbine 45

4.1.2 Three Level NPC Converter 46

4.1.3 10 kW Induction Machine 47

4.2 EVCS SYSTEM COMPONENT VALIDATION 48

4.2.1 Bidirectional DC-DC Converter 49

4.2.2 Synchronous Buck Converter 55

4.2.3 Linear Battery Model 58

4.2.4 Photovoltaic Array 60

5.0 SYSTEM ANALYSIS, OPERATION, AND RESULTS 63

5.1 RESPONSE OF EVCS WITH AND WITHOUT MVDC GRID MODEL INTERCONNECTION 64

5.2 SYNCHRONOUS BUCK CONVERTER TRANSIENT PROPAGATION 69

5.3 CCM / DCM BUCK MODE OPERATION OF BIDIRECTIONAL DC-DC CONVERTER 75

6.0 CONCLUSIONS AND FUTURE WORK 80

BIBLIOGRAPHY 83

LIST OF TABLES

Table 1. Comparison of Energy Storage Technologies [9-12] 10

Table 2. Wind Turbine & PMSG Parameters [4] 21

Table 3. Logic Table for Switching States of the Three Level Neutral Point Clamp Inverter [4, 43] 22

Table 4. Induction Machine Equivalent Circuit Parameters [43] 24

Table 5. Operating Parameters Bidirectional DC-DC Converter 36

Table 6. Operating Parameters Linear Battery Model 41

Table 7. Kyocera Solar KC125G Module [61] 43

Table 8. Operating Regime for testing of the EVCS During Various Modes of Operation 65

Table 9. Operating Regime for EVCS Fault Test 71

LIST OF FIGURES

Figure 1-1. Medium Voltage DC (MVDC) System Architecture [4] 3

Figure 2-1. Worldwide installed energy storage capacity [9] 8

Figure 2-2. Power rating versus discharge time at rated power for various energy storage technologies [9] 9

Figure 2-3. NaS battery electrochemical reaction [19] 12

Figure 2-4. Ideal battery equivalent circuit model 16

Figure 2-5. Linear battery equivalent circuit model 17

Figure 2-6. Thevenin battery equivalent circuit model 17

Figure 3-1. PSCAD MVDC Interconnected Model 18

Figure 3-2. Three Level NPC Converter [4, 43] 22

Figure 3-3. Three-Level Neutral Point Clamped Converter Single Phase Switching States [4, 43] 23

Figure 3-4. Per-Phase Equivalent Circuit of an Induction Motor [44] 24

Figure 3-5. Electric Vehicle Charging Station One Line Diagram 26

Figure 3-6. Electric Vehicle Charging Station with Solar Generation [52] 26

Figure 3-7. Bidirectional DC-DC Converter 28

Figure 3-8. Bidirectional DC-DC Converter Boost Mode Operating Waveforms 29

Figure 3-9. Boost Mode Converter Current Paths for Operating States 30

Figure 3-10. Bidirectional DC-DC Converter Buck Mode Operating Waveforms 31

Figure 3-11. Buck Mode Converter Current Paths for Operating States 32

Figure 3-12. Controller for Bidirectional DC-DC Converter Buck Mode Voltage Regulation ... 35

Figure 3-13. Bidirectional DC-DC Converter with Pre-charge Circuit and Damping Circuit 36

Figure 3-14. Synchronous Buck Converter 37

Figure 3-15. Constant Power Feedback Controller 37

Figure 3-16. Key Operating Waveforms of Synchronous Buck Converter 37

Figure 3-17. Charging Profile for a Lithium-Ion Phosphate Battery [54] 39

Figure 3-18. Electric Vehicle Linear Battery Model 40

Figure 3-19. PV Array equivalent circuit model [4] 42

Figure 3-20. Comparison of theoretical and simulated V-I curves for a single PV module [4] ... 42

Figure 3-21. Incremental Conductance Maximum Power Point Tracking Algorithm [63]d....... 44

Figure 4-1. Mechanical and Electrical Output Power of Permanent Machine Synchronous Generator.. 46

Figure 4-2. Line-to-Line Input Voltage of Three Level NPC Rectifier 47

Figure 4-3. Instantaneous Power Absorbed by Each Induction Machine 48

Figure 4-4. EVCS PSCAD Implementation 49

Figure 4-5. Bidirectional DC-DC Converter PSCAD Implementation 50

Figure 4-6. Bidirectional DC-DC Converter Buck Mode Constant Voltage Controller 50

Figure 4-7. Buck Mode Gating Signals 51

Figure 4-8. Primary Side Voltage (E_P) and Secondary Side Voltage (E_S) 52

Figure 4-9. Choke Inductor Current (i_L) 53

Figure 4-10. Leakage Inductance Current (i_{LK}) 54

Figure 4-11. High Voltage Side Input Current (i_{HV}) 55

Figure 4-12. Synchronous Buck Converter PSCAD Implementation 56

Figure 4-13. Synchronous Buck Converter Controller and Gating Signal Driver....................... 56

Figure 4-14. Synchronous Buck Converter Output Voltage (V_{LV}) 57

Figure 4-15. Synchronous Buck Converter Output Current (I_{LV})... 57

Figure 4-16. PSCAD Implementation of Linear Battery Model... 58

Figure 4-17. PSCAD Calculation of SOC 58

Figure 4-18. EV Battery 2 Pulse Charge Voltage and Current.. 59

Figure 4-19. Example Li-Ion Battery Pulse Charge [64].. 60

Figure 4-20. PV Array and Boost Converter PSCAD Implementation....................................... 60

Figure 4-21. PSCAD Implementation of Incremental Conductance Algorithm.......................... 61

Figure 4-22. PV Array Output Power Test System 62

Figure 5-1. Regulated MVDC Bus Voltage.. 67

Figure 5-2. Regulated LVDC Bus Voltage... 67

Figure 5-3. EVCS Component Absorbed and Received Power 68

Figure 5-4. Bidirectional DC-DC Converter LVDC Bus Output Current (I_{LV}).......................... 69

Figure 5-5. Line to Line Fault Applied to Terminal of EV During Charging 70

Figure 5-6. EVCS Component Absorbed and Received Power During Fault Operation............ 72

Figure 5-7. LVDC Bus Voltage and Synchronous Buck Converter Output Voltage During Fault Operation 72

Figure 5-8. Synchronous Buck Converter Output Voltage During Fault Operation 73

Figure 5-9. Synchronous Buck Converter Output Power During Fault Operation...................... 74

Figure 5-10. Fault Current and Contributing Sources 75

Figure 5-11. Buck Converter CCM Inductor Current Ripple [58] 76

Figure 5-12. Buck Converter DCM Inductor Current Ripple [58] 77

Figure 5-13. Choke Inductor Current (I_L) at Various f_S 78

Figure 5-14. Transformer Primary Voltage (E_P) at Various f_S 79

ACKNOWLEDGEMENTS

Primarily, I would like to my parents who have always encouraged me to question and pursue a greater understanding of the world around me and have been influential in helping me achieve success both personally and academically. They have always made it clear that they believe in me and pushed me to be the best I could be. I would also like to give a special thanks to my siblings Courtney and Matthew who have always been there for me and in general being my best friends in the world without them I wouldn't be the person I am today.

I would like to thank my thesis advisor Dr. Reed for giving me the opportunity to pursue an advanced degree and for being there to provide career and life advice. Dr. Kusic for being an excellent source of knowledge and for the fun times we've had together. Dr. Mao for his constant encouragement to be the best you can be. Dr. McDermott who joined the department in the last semester of my Masters education has provided guidance as well as been there to listen and help formulate the ideas that have gone into the creation of this document.

I would like to thank my graduate student peers. These are the people who make it possible and enjoyable to come to work every day. These people have helped me immeasurably over the last year and a half and are all great friends. Listed in no particular order they are Brandon Grainger, Robert Kerestes, Emanuel Taylor, Matthew Korytowski, Rusty Scioscia, Hashim Al Hassan, Hussain Bassi, Patrick Lewis, Ansel Barchowsky, Alvaro Cardoza, Benoit De Courreges, Jean-Marc Coulomb, Raghav Khanna, Raymond Kovacs and Azime Can.

1.0 INTRODUCTION

Due to a rapidly aging electric transmission and distribution infrastructure, an increased demand for energy and an increased awareness of climate change and greenhouse gas pollution, there is a need to produce and deliver energy more efficiently. Current industry and government solutions point to the development of a smart grid. The electric power energy research for grid infrastructure (EPERGI) team at the University of Pittsburgh defines smart grid as "The implementation of various enabling power technologies that allow real-time interoperability between end-users and energy producers, in order to enhance efficiency in utilization decision-making based on energy resource availability and economics." d Based upon investigation of representative approaches of various independent entities, utilities, and manufacturers, gaps within existing smart grid enabling technology were identified. These gaps included: improved control of transmission and distribution, energy storage, renewable integration, information and incentives for both the end-user and the utility [1]. This thesis attempts to establish how next generation DC power systems, and power conversion devices can be used to provide enhanced control, utilization, and efficiency as a key enabling technology of the smart grid. Two main topics in particular are investigated and simulated using PSCAD, a medium voltage direct current (MVDC) network, and a common direct current (DC) bus electric vehicle charging station (EVCS).

1.1 MEDIUM VOLTAGE DC NETWORK

Over the past five decades high voltage direct current (HVDC) technology has proven its merit as a reliable and efficient method of delivering bulk power over long distance / under water, and linking asynchronous power networks [2]. At the medium voltage levels, DC power systems have received usage within naval power systems [3]. Beyond these limited applications, DC systems have not found widespread use. The medium voltage direct current (MVDC) concept is conceived as a collection platform which will provide an additional layer of infrastructure between transmission and distribution to help integrate renewable generation (photovoltaic, wind), energy storage, and various end-use loads (industrial facilities, data centers). A general overview of the proposed MVDC architecture is shown in Figure 1-1. It should be noted that the MVDC system is not a simple scaling of voltage level from HVDC and has distinct applications. MVDC systems will help to reduce the number of conversion stages necessary for integrating the lower voltage output of renewable generation resources to the electric grid operating at a much higher voltage whereas HVDC is used for interconnection of asynchronous grids and long distance transmission of power.

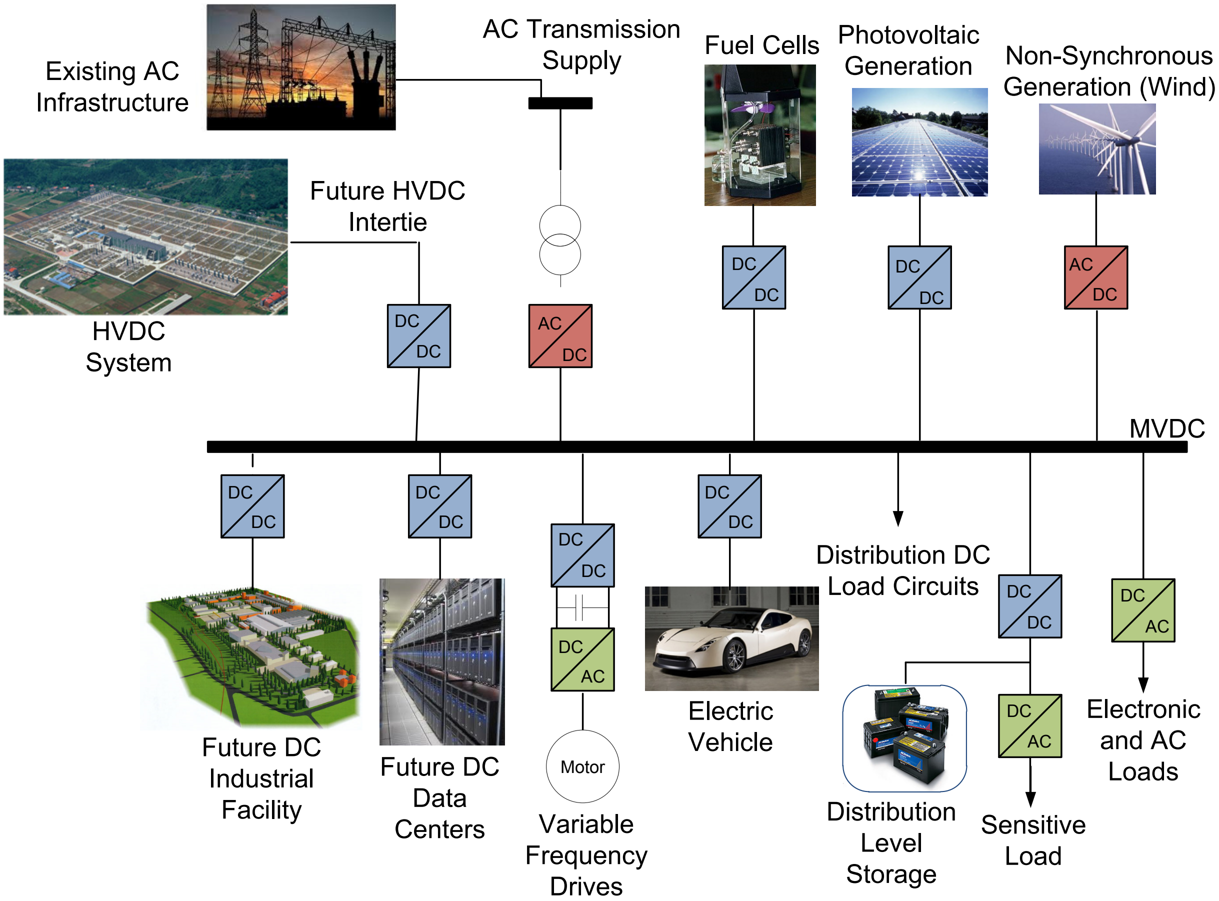

Figure 1-1. Medium Voltage DC (MVDC) System Architecture [4]

1.2 ELECTRIC VEHICLE CHARGING STATION

Presently, the vast majority of energy consumption by the transportation sector comes from petroleum [5]. Vehicles with unconventional fuel systems (flex-fuel, diesel, hybrid-electric) constituted 15 percent of new vehicles sales in 2009 [5]. While electric vehicles make up a small percentage of vehicles sold, consumers are comfortable with buying vehicles containing alternative fuel systems. Auto manufacturers large (General Motors and Nissan) and small (Tesla

Motors) are beginning to manufacture and produce full electric vehicles. The United States government predicts that over one million electric vehicles will be on the road in the United States by 2015 [6]. These predictions of increased electric vehicle penetration are more than just predictions, serious investments are being made in the industry; for example, Google has invested $10 million in EV research, the U.S. government has in its goal of one million EV by 2015 agreed to over $2 billion in stimulus spending [7]. To meet this increased penetration of plug-in hybrid electric vehicles (PHEV) and electric vehicles (EV), new infrastructure is required from charging stations to enhanced electric distribution networks.

1.3 PROBLEM STATEMENT AND MOTIVATION

The overall MVDC concept is a large multi-year endeavor currently being explored by the research group at the University of Pittsburgh, more complete and thorough understanding of the architecture from the component level up to and including system architecture is necessary for the concept to become a reality, as well as the determination of applications in which it can be proven more efficient, reliable, or cost effective than comparable AC systems. In the world of commercial data centers the merit of DC architecture over AC has proven its merit and is beginning to see full scale implementations [8]. This thesis serves two main goals, first to determine the applicability of the common DC bus system for use in next generation level 2 DC electric vehicle charging stations. Secondly, the interaction of the MVDC bus with active loads needs to be determined. The EVCS is a unique application in itself in that it combines renewable generation, power electronic converters, and battery energy storage systems all together. Lessons learned from the work performed in this thesis can be extrapolated to projects containing any combination of those three smart grid enabling devices. The objectives of this thesis include:

- Literature survey of state-of-the-art battery energy storage systems, battery modeling techniques, and power electronic converters.
- Design of models for various forms of renewable generation, power electronic conversion devices, and battery energy storage systems.
- Design of a next generation common DC bus electric vehicle charging station which utilizes on site renewable generation, level 2 DC quick chargers, a DC bus for component connection as well as a MVDC tie.
- Evaluation of system level equipment interaction during various modes of operation to determine applicability of the common DC bus EVCS as well as the applicability of the MVDC network to serve DC loads. Determination of the ability of battery chargers (synchronous buck converter) to help mitigate transient propagation in DC power systems. The lessons learned within this thesis will help to identify design criteria and help steer future research initiatives.

1.4 ORGANIZATION OF DOCUMENT

Chapter 2.0 provides a thorough overview of battery energy storage systems. This chapter provides general information on the uses of battery energy storage systems (BESS), the penetration of grid level BESSs, installation costs of grid energy storage systems, and presents an introduction to battery modeling techniques. Section 2.1 provides a survey of battery energy storage system technologies and costs. Section 2.2 gives the reader an introduction to battery modeling in particular equivalent circuit battery modeling which is utilized in this thesis for the simulation of the EV battery during charging.

Chapter 3.0 provides a general background of the power electronic converters and sources of generation and load utilized within both the MVDC and EVCS models. Section 3.1 gives an overview of the simulated MVDC network while providing background, design and theory for the individual components within the MVDC architecture. In particularly, the PMSG wind turbines, neutral point clamped inverters and induction machines are presented in this section. Section 3.2 yields the background, design and theory behind the components within the EVCS; which includes the PV array, bidirectional DC-DC converter, battery charger (synchronous buck converter) and EV battery are discussed. Chapter 4.0 provides validation of the operation of the individual components used in the overall simulation of the MVDC and EVCS networks.

Chapter 5.0 of this thesis presents simulation results and analysis. In section 5.1, the response of the EVCS with and without interconnection to the full MVDC network model is explored to validate the use of an ideal voltage source as a representation of the MVDC network and to explore and validate overall system interaction and operation. Section 5.2, explores how the battery charger (synchronous buck converter) can be used to mitigate the propagation of transients in next generation DC power systems. Section 5.3 explores CCM / DCM operation of the bidirectional DC/DC converter during buck operation at various switching frequencies. Finally, Chapter 6.0 yields a discussion of conclusions and future work identified through completion of this thesis.

2.0 BATTERY ENERGY STORAGE SYSTEMS

Battery energy storage systems (BESS) provide solutions to many of the goals of a smart grid. BESS can be used for:

- Renewable integration
- Stationary capital investment deferral at the generation, transmission and distribution level
- Transportable capital investment deferral
- Peak shaving and load leveling
- Peak shifting
- Distributed energy storage systems (DESS)
- Power quality management
- Spinning reserve and area regulation
- Emergency backup power [9]

Electricity is stored on a large scale (greater than 1kW) in various ways including pumped hydro, secondary battery technologies (Lead-Acid, Nickle-Cadmium, Sodium-Sulfur), and compressed air energy storage (CAES). Secondary battery technologies range in maturity from commercial and industry tested installations to those that are still in research and development; however, these technologies have not gained widespread use due to not meeting the fundamental requirements of high capacity and long discharge times whilst remaining cost effective or without special site considerations. The primary drawback to mechanical forms of energy storage such as pumped hydro, and CAES, is that they both require special geological locations to be feasible, and many times these locations are far from where the storage is needed.

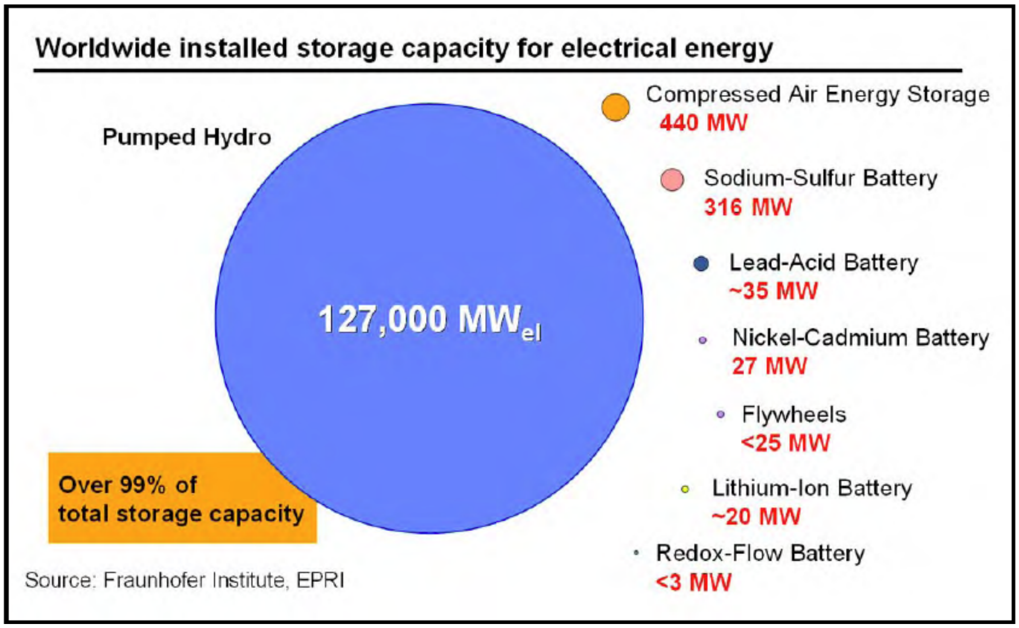

Figure 2-1. Worldwide installed energy storage capacity [9]

Globally, pumped hydro and CAES are the two forms of energy storage which are used the most, as shown in Figure 2-1. Due to the fact that pumped hydro and CAES can only be employed in particular locations the future of grid level energy storage is battery technology. Different energy storage technologies vary in maturity from commercial and industry tested (Lead-Acid, Pumped Hydro) to those that are still in an experimental design phase (Zinc-Bromine Flow) [9]. Bulk energy storage (greater than 1 kW) is employed for various purposes including but not limited to power quality management, grid level support, and bulk power management. Energy storage technologies vary in: installation sizes ranging from kilowatts to gigawatts, and discharge time ranging from seconds to hours, in order to fill the wide range of uses of energy storage. This trend is pictorially represented in Figure 2-2.

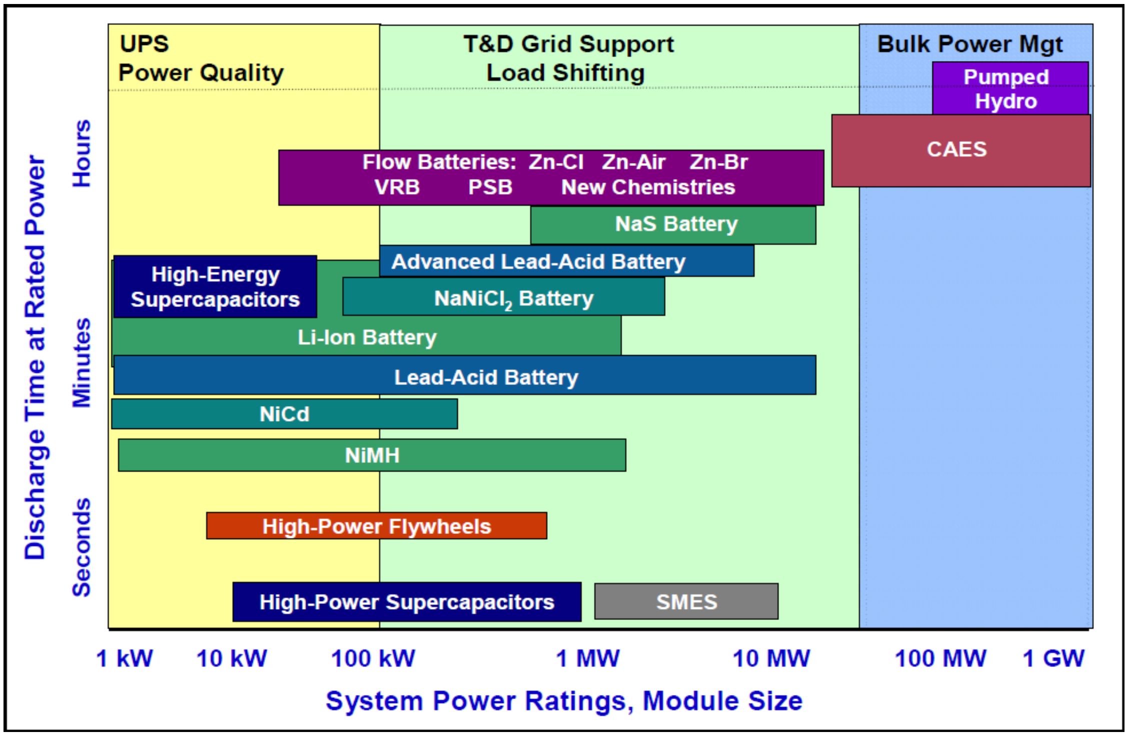

Figure 2-2. Power rating versus discharge time at rated power for various energy storage technologies [9]

2.1 SURVEY OF BATTERY ENERGY STORAGE SYSTEM TECHNOLOGIES

There is a wide variety of energy storage technologies, each with their own set of benefits including varying: energy densities, self-discharge rates, calendar lives, and costs. Summarized in Table 1 is a comparison of pertinent metrics for select energy storage technologies.

Table 1. Comparison of Energy Storage Technologies [9-12]

Storage Technology	**Maturity**	**Power (MW)**	**Duration (hrs)**	**Capacity (MWh)**	**% Efficiency (total cycles)**	**Total Cost ($/kW)**	**Self Discharge**	**Response Time**
Lead-Acid	Commercial	50	6	300	85-90 (2200)	3100-3300	Low	ms
Na-S	Commercial	1	7.2	7.2	75 (4500)	3200-4000	--	ms
Zn/Br Flow	Demo	1	5	5	70-76 (2000-3000)	1670-2015	--	ms
Li-ion	Demo	1-100	.25-1	.25-25	87-92 (>100,000)	1085-1550	Med	ms
Vanadium Redox	Demo	1	4	4	65-75 (>10,000)	3000-3310	Negligible	ms
Pumped Hydro	Mature	250-530	6-10	1680-5300	80-82 (>13,000)	2500-4300	Negligible	min
CAES	Commercial	135	8	1080	60-70	1000	--	sec

The use of lead-acid batteries dates back to the mid-1800s. They are most commonly used in automobiles or as a form of backup power such as in an uninterruptible power supply [13]. Lead-acid batteries have a non-linear power output, and their lifetime varies greatly based off of usage, discharge rate, and number of deep discharge cycles [9]. Their price is dependent upon and highly influenced by the price of lead [9]. Lead-acid batteries have traditionally been used for backup power, and power quality management for control systems and switching components [9].

During charging, lead sulfate is converted to spongy lead via an electrochemical reaction, at the negative electrode while lead dioxide is formed at the positive electrode due to the flow of current [13].

Newer lead-acid batteries use advanced materials and technologies to improve life cycle and performance. Some of these advanced lead-acid batteries are being developed specifically to perform transmission and distribution grid level support [9].Lead-acid batteries are the most commercially mature utility scale rechargeable battery technology, with over 20 years of industry usage [1]. The main benefit of lead-acid batteries is their low cost [13]. Examples of lead-acid batteries used for utility level energy management includes the Chino battery energy storage power plant, the Puerto Rico electric power authority battery electric storage system, and the Metlakatla Power and Light battery energy storage system [14, 15]

Due to the short operation life of lead-acid batteries, they are more often used for emergency power and power quality management. During charging, hydrogen is produced at the negative electrode. This means that if the battery is overcharged it will suffer water loss. This is mitigated in utility scale installations through the use of Valve-Regulated Lead-Acid (VRLA) batteries, which automatically allows recombination of charge gas [10]. Lead-acid batteries have a very low energy density when compared to other battery technologies. Lead-acid batteries also suffer from relatively short calendar/cycle lives of approximately 4-5 years/750 cycles, meaning that they are replaced frequently, for heavy usage beyond back up power [16, 17].

The Sodium sulfur battery was originally developed by the Ford Motor Company in the 1960's. It contains sulfur at the positive electrode and sodium at the negative electrode. These electrodes are separated by a solid beta alumina ceramic [18]. Through an electrochemical reaction, electrical energy is stored and released on demand. This effect is shown below in Figure 2-3 [19]. NaS batteries have an operating temperature between 300 and 360 °C [18]. The primary manufacturer of NaS batteries, NGK Insulators, LTD, builds the batteries in 50 kW modules which are combined to make MW class battery systems [20].

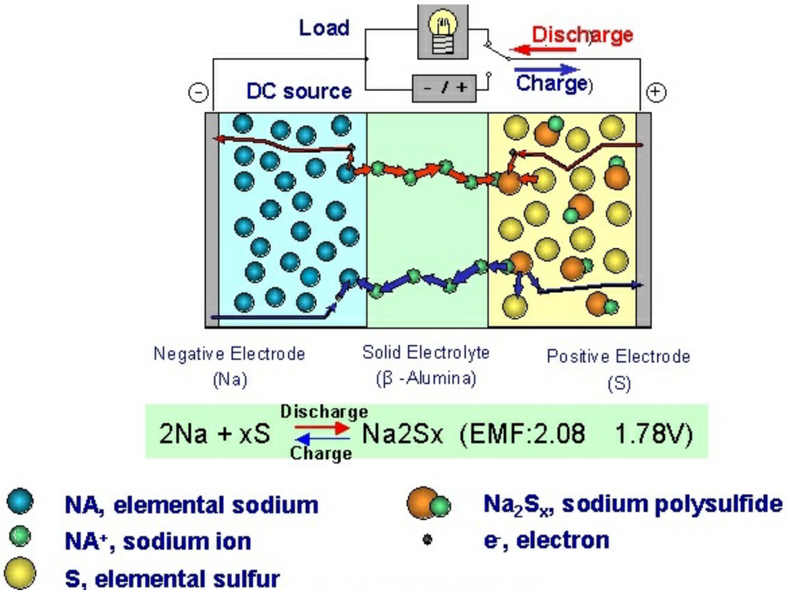

Figure 2-3. NaS battery electrochemical reaction [19]

NaS batteries exhibit high power and high energy density, high coulombic efficiency, good temperature stability, long cycle life, and low material costs [21, 22]. Their energy density is approximately three times that of traditional lead-acid batteries [23]. They have a high DC conversion efficiency of approximately 85% [22]. This high DC conversion efficiency makes sodium sulfur batteries an ideal candidate for implementation into future DC distribution systems [1]. NaS batteries can be used for a wide variety of applications including peak shaving, renewable integration, power quality management, and emergency power. They have the ability to discharge above their rated power, which makes them ideal to operate in both a peak shaving and power quality management environment [20]. NaS batteries are also one of the more commercially mature battery technologies, with use by AEP and TEPCO [19, 24, 25].

Lithium-Ion batteries have traditionally been used to power consumer electronic devices, and more recently for plug-in hybrid electric vehicles [9]. The lithium-ion battery operates by allowing the lithium ions to move between the anode and cathode producing a flow of current. Lithium-ion battery technology is one of the newer technologies examined in this paper (first commercialized in 1991 by Sony Co.) [26]. There are many chemical configurations that are classified as a lithium-ion battery. Each of these configurations has its own power and energy characteristics [26].

Advantages of Lithium-ion batteries include high energy density, no memory effect, long calendar life and a low self-discharge. Having no memory effect means that Li-Ion batteries do not require scheduled cycling [26, 27]. Memory effect decreases a batteries usable capacity over time if it is repeatedly discharged to only a certain percent (greater than zero). Cycling is then used to reset this by forcing the battery to fully discharge. Due to the scarcity of lithium, lithium-ion batteries are more expensive than other battery technologies [10]. Current grid level Li-Ion storage installations include smaller demonstration systems of 1MW or less [9]. According to the U.S. DOE, Li-Ion batteries used for frequency regulation are one of the fastest growing markets for energy storage. The DOE estimates that the installed capacity of Lithium-Ion batteries in the U.S. for Grid level storage is 54 MW [28].

2.2 BATTERY MODELING

The main objective of battery modeling is to provide a representation of a batteries operation via a mathematical equation, equivalent circuit or a combination of the two. There are a few main methods of modeling a battery's operation. These models include mathematical models, electrochemical models and equivalent circuit models. All three methods have their own unique benefits and drawbacks. Mathematical models [29-31], use purely equations to simulate a battery's operation; however, these models are not able to provide the necessary I-V information for system level simulation [32]. A secondary draw back in mathematical models is that their steady state error is on the order of 5%-20%, the highest of the three examined models [32]. Electrochemical models [33-35], take into account the kinetics and thermodynamics of the battery's electrochemical reaction. They are highly complex and require days of simulation to obtain an accurate result; however, they provide the most accurate steady state simulation [32]. Equivalent circuit models [36-40], provide a compromise between mathematical and electrochemical models in terms of accuracy, between 1%-5% [32]. Equivalent circuit models are presented in a way that is easy for electrical engineers to work and integrate with circuit simulation programs.

2.2.1 **Electrochemical Models**

Electrochemical battery models use the chemical, thermodynamic, and physical qualities of the battery and yield the most accurate results, at a sacrifice to simulation time [33-35, 41]. The Peukert relationship displayed in (2.1) is used to determine the state of charge, SOC, of a battery with constant discharge rate [42].

$$I^n * T_i = K \tag{2.1}$$

where:

- I is the discharge current in Amps
- n is a battery constant determined by the battery technology
- K is a fixed constant

Using the Peukert relationship, the battery capacity in ampere-hour at a given discharge rate I_i can be related to a known discharge rate I_n, as shown by (2.2).

$$C_i = C_n (I_n / I_i)^{n-1} \tag{2.2}$$

where:

- C_i is the battery capacity in Ampere-hours
- C_n is a known battery capacity in Ampere-hours
- I_n is a known discharge rate in Amps
- I_i is a given discharge rate in Amps
- n is a battery constant determined by the battery technology

For a constant discharge rate, the SOC as a function of the present discharge rate and capacity can be calculated using (2.3).

$$\begin{aligned} SOC &= 1 - C_{Di} / C_i \\ C_{Di} &= I_i t \end{aligned} \tag{2.3}$$

where:

- C_i is the battery capacity in Ampere-hours
- C_{Di} is the capacity in Ampere-hours at discharge rate I_i and time t
- I_i is a given discharge rate in Amps
- SOC is the battery's current state of charge

For a non-constant discharge rate, which is the case with a real world battery energy storage system implementation, the SOC equation will change so that the relation is evaluated in small time intervals, as shown by (2.4). SOC_K (2.5) is the net state of charge at k-th time interval.

$$\Delta SOC_K = -\frac{I_i \Delta t}{3600 C_n} \left(\frac{I_i}{I_n} \right)^{n-1} \tag{2.4}$$

$$SOC_K = SOC_{K-1} + \Delta SOC_K \tag{2.5}$$

where:

- I_i is a given discharge rate in Amps
- I_n is a known discharge rate in Amps
- C_n is a known battery capacity in Ampere-hours
- n is a battery constant determined by the battery technology
- SOC_K is the net state of charge at the k-th interval

2.2.2 **Equivalent Circuit Models**

Equivalent circuit battery models are typically used for power system simulations. Due to being composed of common circuit components such as voltage sources, resistors and capacitors; equivalent circuit battery models are easier for electrical engineers to work with. There are two main types of equivalent circuit battery models, static and dynamic. Static battery models use predetermined and constant battery characteristics throughout the entire simulation. In a dynamic battery model, the battery voltage, current, charge, and temperature all vary as a function one another which dynamically affects the output.

The most basic equivalent circuit model for batteries is the ideal circuit model shown in Figure 2-4. This model is characterized by a voltage source only, and does not represent internal battery characteristics [38].

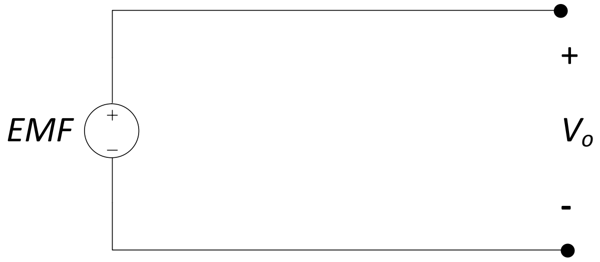

Figure 2-4. Ideal battery equivalent circuit model

The linear model, Figure 2-5, expands upon the ideal circuit model by adding a resistor in series with the voltage source. This resistor, R_{int}, represents the internal resistance of the battery. The voltage source, *EMF*, is the no load voltage of the battery. This model can be improved by making the values of R_{int} and *EMF* dependent upon the battery SOC instead of fixed values [38].

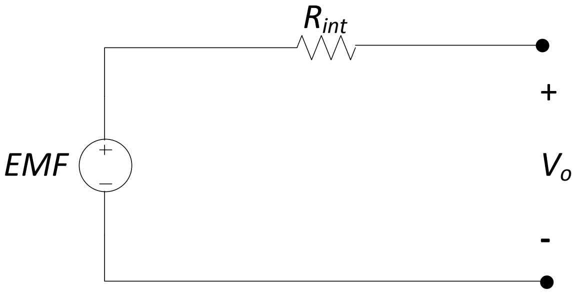

Figure 2-5. Linear battery equivalent circuit model

The Thevenin Model, Figure 2-6, includes the ideal no load voltage, *EMF*, the battery internal resistance, R_2, as well as the addition of capacitance, C_1, and an overvoltage resistance, R_1. Like the linear model, the Thevenin model's accuracy can be improved by making the parameters which determine the internal resistance and electromotive force variable and determined by the battery current SOC [39]

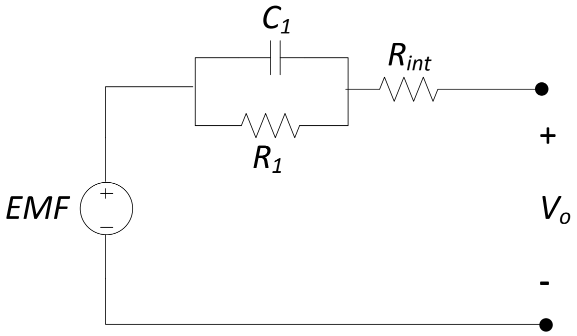

Figure 2-6. Thevenin battery equivalent circuit model

3.0 SYSTEM LAYOUT AND DESIGN

This section presents the design and simulation of a common DC bus electric vehicle charging station (EVCS) which uses solar power in conjunction with a tie to the MVDC network to charge the EVs. The operation of the EVCS is evaluated with and without connection to the MVDC grid model, shown in Figure 3-1. The design of the MVDC grid as a whole is not the focus of this thesis and thus, the control and sizing of components is not discussed in detail. Further information on the design and control of the larger MVDC grid is available in [4, 43].

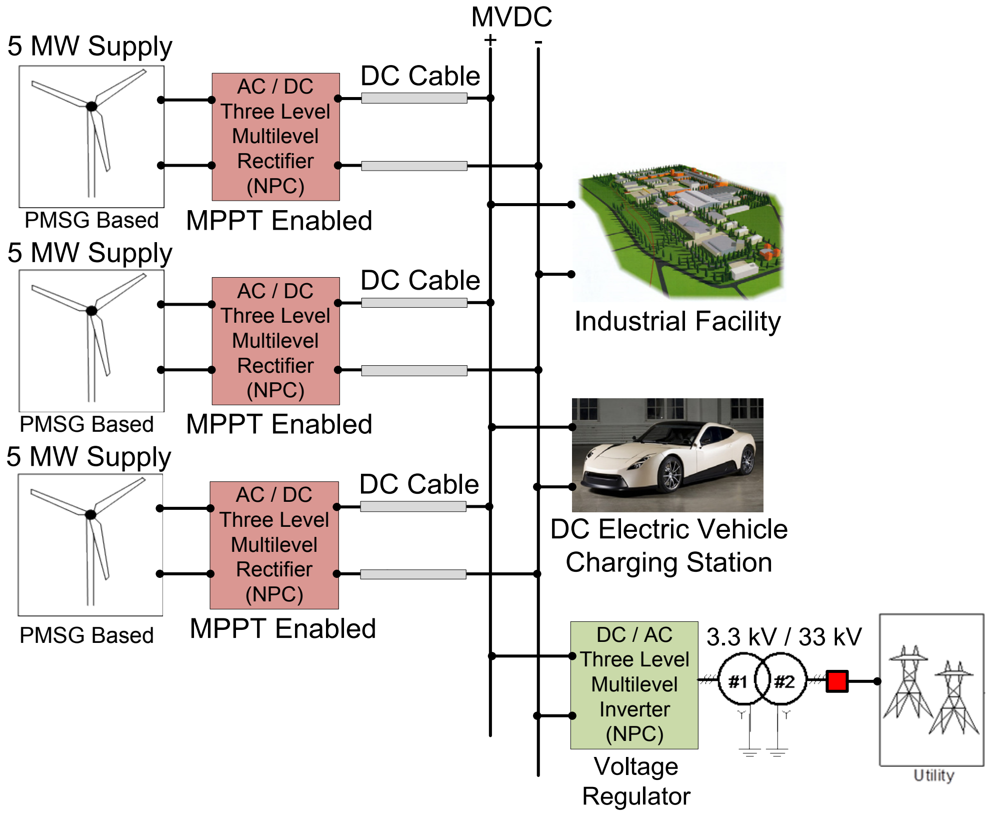

Figure 3-1. PSCAD MVDC Interconnected Model

3.1 MVDC NETWORK

The MVDC network serves as the main source of generation in the interconnected model. The MVDC grid model, Figure 3-1, consists of three 5-MW permanent machine synchronous generators (PMSG) connected to the DC bus via three level neutral point clamped (NPC) rectifiers and DC cable. The industrial facility is modeled as two 10 kW induction machines operating at 60 Hz each of which are interfaced via a three level NPC inverter. The bus reactive power and voltage is regulated via the utility tie three level NPC inverter. The utility is represented as an infinite bus which absorbs the excess power generated by the wind turbines.

3.1.1 **Wind Power Generation Model Development**

The first step in modeling a wind turbine generator is quantifying the mechanical power supplied by the wind. The mechanical power supplied by the wind for a given area swept by a turbine is presented in (3.1). The power coefficient (C_P), is presented in (3.2) and (3.3), the coefficients are experimentally determined, $C_1 = 0.5176$, $C_2 = 116$, $C_3 = 0.4$, $C_4 = 0$, $C_5 = 5$, $C_6 = 21$, and $C_7 = 0.0068$ [4].

$$P_T = \frac{1}{2}\rho A C_P(\beta,\lambda)V_W^3 \tag{3.1}$$

where:

- P_T is the mechanical power supplied by the wind
- ρ is the density of air
- A is the area swept by the blades of the wind turbine
- C_P is an experimentally determined power coefficient
- β is the pitch angle of the wind turbine blades
- λ is the tip speed ratio of the wind turbine blades
- V_W is the wind velocity

$$C_P(\beta,\lambda) = C_1\left(C_2\frac{1}{\Lambda} - C_3\beta - C_4\beta^x - C_5\right)$$
$$\exp(-C_6/\Lambda) + C_7\lambda \tag{3.2}$$

$$\frac{1}{\Lambda} = \frac{1}{\lambda + 0.08\beta} - \frac{0.035}{1+\beta^3} \tag{3.3}$$

The wind turbine simulated within this thesis is based off of a permanent magnet synchronous generator (PMSG). The PMSG wind turbine model utilizes a dq machine model in the simulation. The electromechanical model of the PMSG is represented by (3.4) through (3.6). (3.4) and (3.5) are used to simulate the electrical characteristics of the PMSG, while (3.6) represents the mechanical model of the turbine. Lastly, the electromagnetic torque of the PMSG is calculated via (3.7) [4]. The parameters utilized in simulating the PMSG wind turbine are presented below in Table 2.

$$V_d = R_s i_d + L_s\frac{di_d}{dt} - \omega_r L_s i_q \tag{3.4}$$

$$V_q = R_s i_q + L_s\frac{di_q}{dt} + \omega_r L_s i_d + \omega_r L_m \tag{3.5}$$

$$T_e - T_m - F\omega_r = J\frac{d\omega_r}{dt} \tag{3.6}$$

$$T_{em} = \frac{3}{2}\frac{P}{2}\left(\lambda_m i_q + \left(L_{ds} - L_{qs}\right)i_d i_q\right) \tag{3.7}$$

where:

- *d* and *q* subscripts represent the direct and quadrautre axis of the machine
- *r* subscript represents the rotor of the machine
- *s* subscript represents the stator of the machine
- *e* subscript represents an electrical parameter
- *m* subscript represents a mechanical parameter

- F is the fiction factor of the machine
- J is the moment of inertia of the rotor
- P number of pole pairs
- λ_m is the flux of the permanent magnet

Table 2. Wind Turbine & PMSG Parameters [4]

Wind Turbine Parameters		PMSG parameters	
Rate power P_n	5 MW	Rate power P_n	5 MW
Rated rotor speed n_r	14.8 rpm	Rated voltage (L-L RMS)	3.3 kV
Rotor diameter D	116 m	Rated current (RMS)	0.92 kA
Hub height	138 m	Power factor	0.95
Hub height mean speed	11.8 m/s	Phase resistor R_s	50 mΩ
Cut in wind speed	2.5 m/s	d-axis inductance $L_{md}+L_\sigma$	3.5218 mH
Cut out wind speed	25 m/s	q-axis inductance $L_{mq}+L_\sigma$	3.5218 mH
Rated wind speed	11.8 m/s	PM flux	14.3522Wb
Optimum tip speed ratio γ	7.6179	Number of pole pairs	118
Maximum power coefficient C_p	0.4746	Inertia factor	2.5e5 kg.m^2
Air density	1.225 kg/m^3	Friction factor	2.26e4 N.m.s

3.1.2 Three Level NPC Converter

In the MVDC model, three level NPC rectifiers and inverters are utilized as the power conversion equipment of choice. This section will focus on the discussion of the NPC inverter once understanding the operation of the inverter, the operation of the rectifier is intuitive. At its most basic, a single phase three level NPC inverter is made up of a series combination of two two-level voltage source inverters. The two-level voltage source inverters are connected via two clamping diodes per phase. This “neutral clamp” serves to divide the DC-link voltage into two equal halves. Splitting the link voltage among double the switching devices allows for the use of lower rated semiconductors. A three phase three level NPC converter is presented in Figure 3-2.

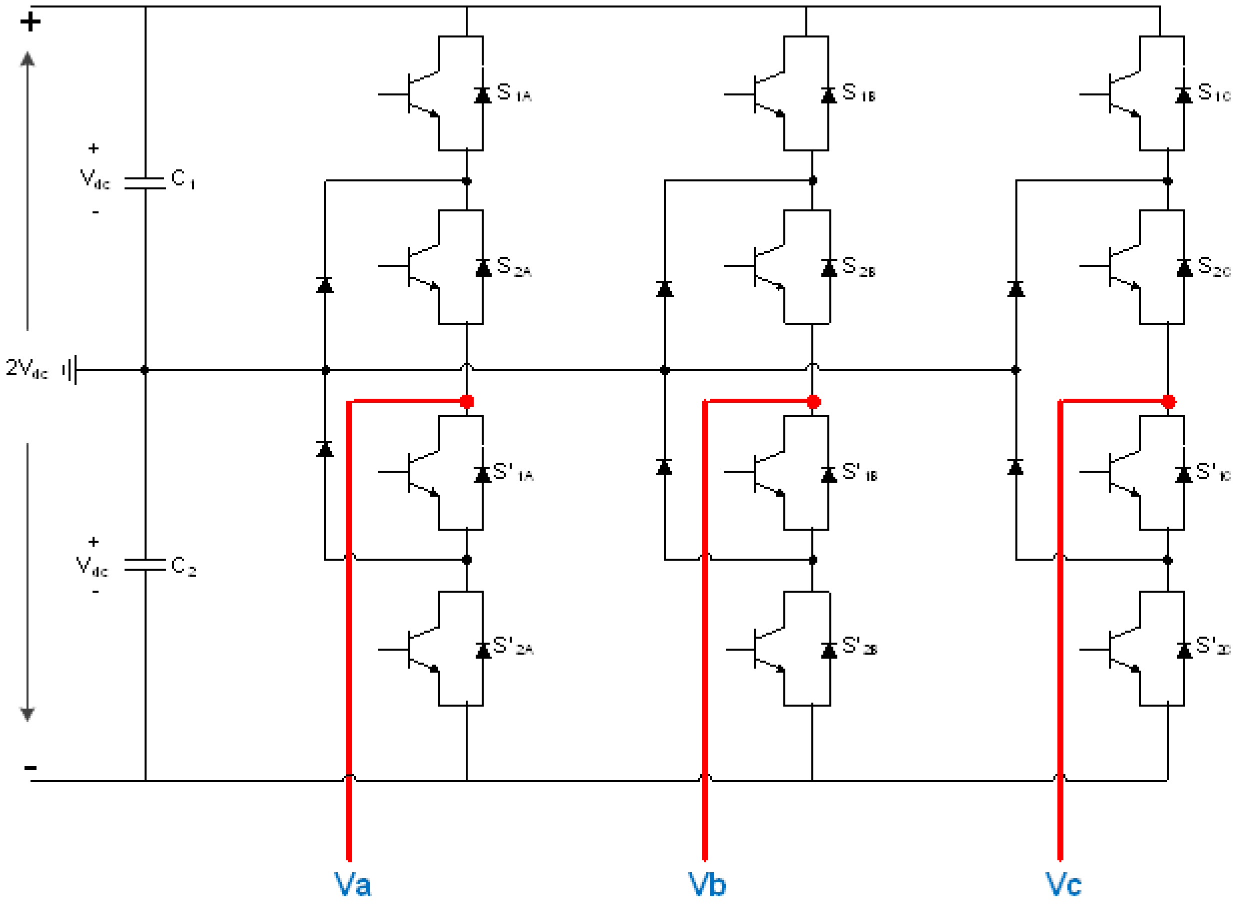

Figure 3-2. Three Level NPC Converter [4, 43]

Each phase of phase of the three level NPC converter contains three switching states. The three switching intervals for a "leg" of the NPC converter is presented in Table 3. This table is visually represented in Figure 3-3. Each phase of the NPC converter contains four control signals S_1, S_2 and their compliments; this is done to prevent a short circuit of the DC link. A three phase converter is realized by phase shifting the control signals by 120 degrees [4, 43]

Table 3. Logic Table for Switching States of the Three Level Neutral Point Clamp Inverter [4, 43]

Interval	S_1	S_2	S'_1	S'_2	Voltage
1	1	1	0	0	V_{DC}
2	0	1	1	0	0
3	0	0	1	1	$-V_{DC}$

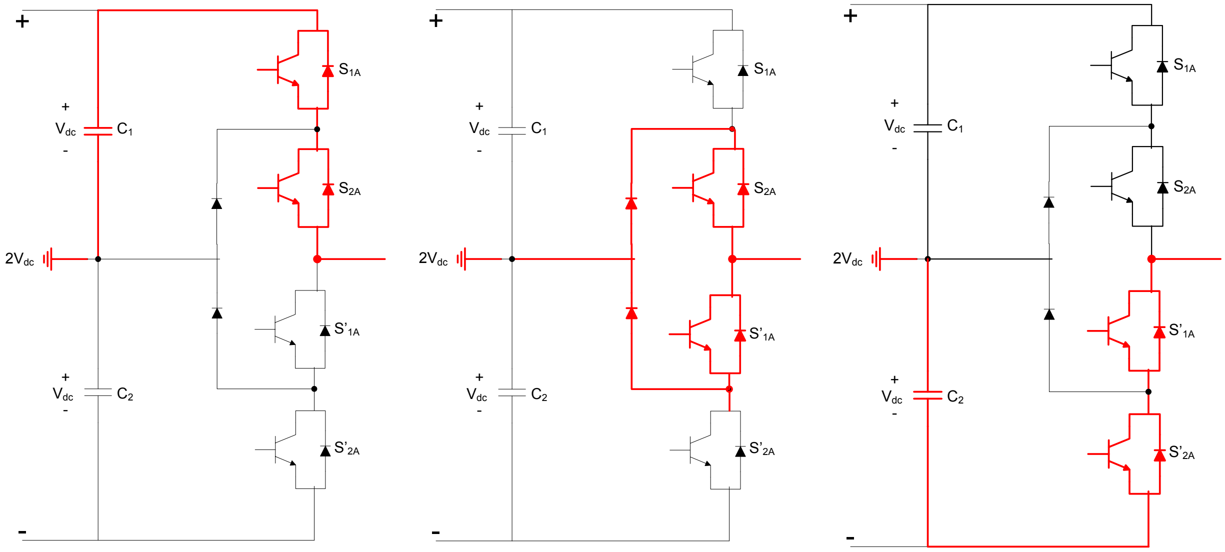

Figure 3-3. Three-Level Neutral Point Clamped Converter Single Phase Switching States [4, 43]

3.1.3 **Industrial Facility**

In the MVDC system model, the industrial facility represents the other load in the system. The industrial facility is modeled using two 10-kW, 460 V (line-to-line rms), three phase, 4-pole induction machines each powered via a three level NPC inverter. The inverter output is 3.3 kV$_{L\text{-}L}$ which is then stepped down via a transformer to the 460 V$_{L\text{-}L}$ power needed for the machine. In this model the inverter is operating similarly to a drive. However, the inverter does not possess the controls necessary to provide regulation and correction beyond steady state feed forward control.

The induction machine parameters used in this simulation are presented in Table 4. These parameters provide the per unit values for the per-phase induction machine equivalent circuit presented in Figure 3-4. In this equivalent circuit, the components specified with a subscript one represent stator components and components with a subscript two represent rotor components.

Utilizing the per-phase equivalent circuit shown above in Figure 3-4, the machines electrical power (P_e), mechanical power (P_{mech}), and electromechanical torque (T_e) can be calculated.

Table 4. Induction Machine Equivalent Circuit Parameters [43]

Stator Resistance (R_1)	0.025
Referred Resistance (R_2)	0.030
Stator Reactance (X_1)	0.10
Referred Reactance (X_2)	0.10
Magnetizing Resistance (R_M)	20
Magnetizing Reactance (X_M)	2.4

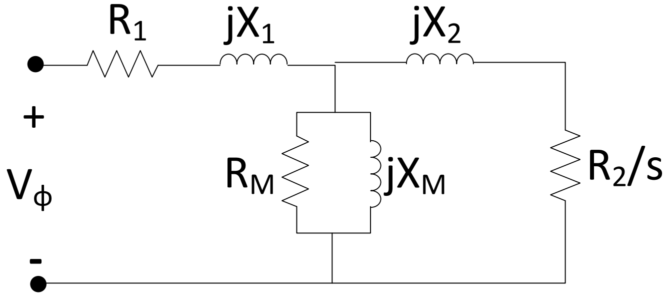

Figure 3-4. Per-Phase Equivalent Circuit of an Induction Motor [44]

3.2 EV CHARGING STATION

Traditional level 2 DC quick charge electric vehicle charging stations (EVCS) utilize a common AC bus architecture, which rectifies power for charging the electric vehicles [7]. An alternative architecture rectifies the power at the input of the charging station and utilizes a common DC bus throughout the EVCS [45, 46]. The system evaluated in this thesis, shown in Figure 3-5, utilizes the common DC bus idea [45-47]. However, this simulation expands upon the idea through connection of the system to a larger MVDC bus via a bidirectional DC-DC converter. A second deviation is through use of detailed and accurate models of power converters as well as the use of the PSCAD simulation environment, which allows simulation at a much smaller time step (12μs was used in all experimentation) to more accurately capture the operation of the power electronic conversion devices and allow for transient level evaluation.

3.2.1 **Design Criteria for the EV Charging Station**

The modeled system, Figure 3-5, consists of a 20 kW solar array, two level 2 DC fast chargers and a tie to the MVDC network via a bidirectional DC-DC converter, which allows for the EVCS to operate as a source of generation when no load is present. This study investigates the power conversion infrastructure present within the EVCS as well as its interaction with the larger MVDC network.

The use of a LVDC bus in the EVCS allows for greater system efficiency by removing the inversion step which would otherwise be necessary at the output of the solar panels. The DC EVCS also reduces footprint by replacing the large 60Hz input transformer with a smaller high frequency transformer present within the bidirectional DC-DC converter while still providing galvanic isolation. Figure 3-6 presents a typical EVCS with roof mounted solar panels. A bus voltage of 800 V_{DC} was chosen for the LVDC bus. A standard LVDC bus voltage has not been determined and many voltage levels exist in literature [48-50]. The DC bus was grounded via capacitive coupling at the sources and loads as described in [51].

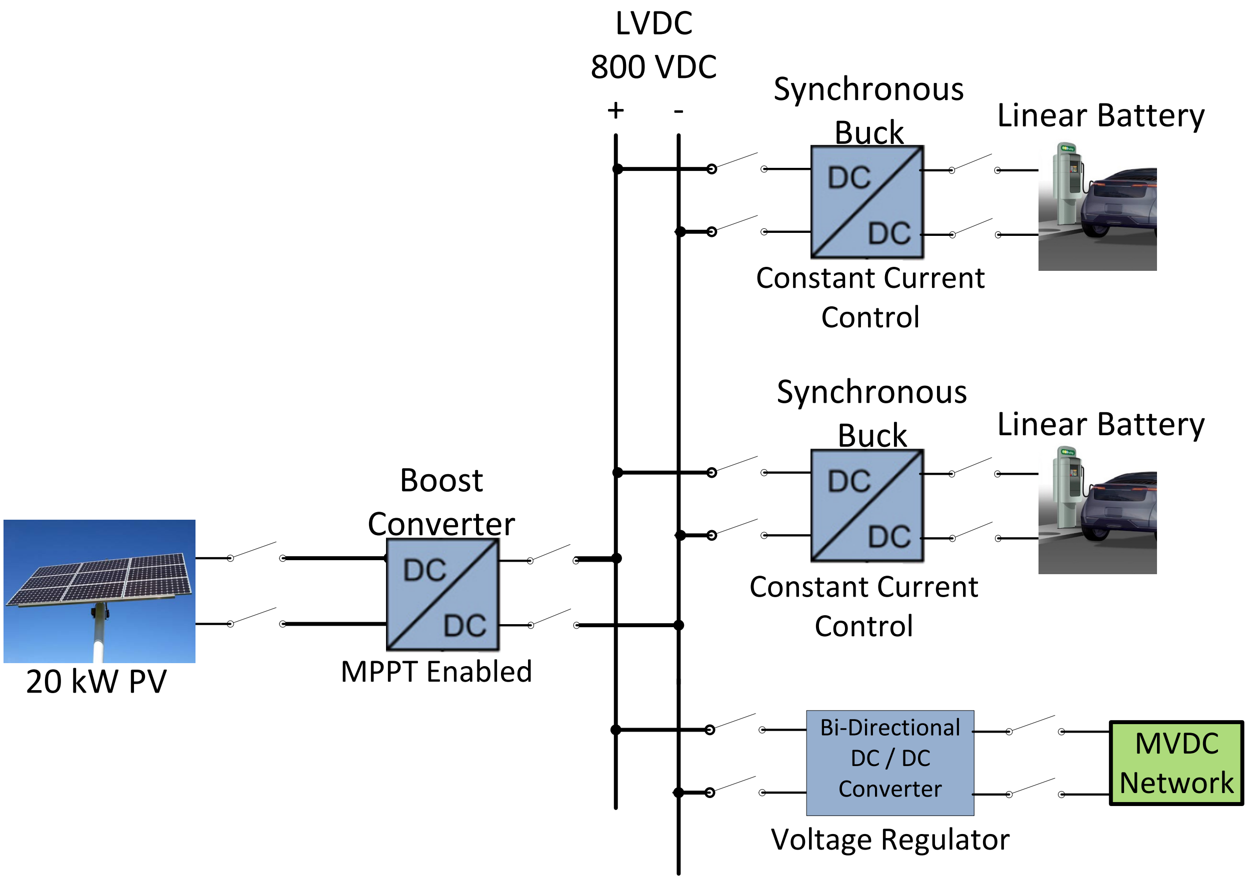

Figure 3-5. Electric Vehicle Charging Station One Line Diagram

Figure 3-6. Electric Vehicle Charging Station with Solar Generation [52]

The designed system utilizes level 2 DC vehicle charging. Level 2 DC charging utilizes 50-70 kW of charging power and is capable of fully charging an electric vehicle in 15-50 minutes. Current charging systems are classified as level 1 and level 2 AC. Level 1 AC charges at 1.4 kW and takes 18 hours to charge. Level 2 AC chargers provide 3.3 or 6.6 kW of power and takes 8 or 4 hours to charge respectively [7, 53, 54]. At 50 kW of charging power, a level 2 DC fast charger will almost exclusively be installed at commercial / industrial locations, such as the system presented in this study.

3.2.2 **Bidirectional DC-DC Converter**

The bidirectional DC-DC converter allows for a bidirectional flow of power to utilize grid power when necessary and to supply power to the grid when excess power is generated, shown in Figure 3-7. Applications of bidirectional DC-DC converters include battery energy storage systems, next generation motor drives, interconnecting load centers that possess on site generation [48, 55-57]. The bidirectional DC-DC converter used in this section is based off of the one designed in [48, 57].

In this chapter the bidirectional DC-DC converters operation within the context of the EVCS, Figure 3-5, will be considered. In buck mode, the bidirectional DC-DC converter, Figure 3-7, utilizes constant voltage control to operate as a voltage regulator for the LVDC bus.

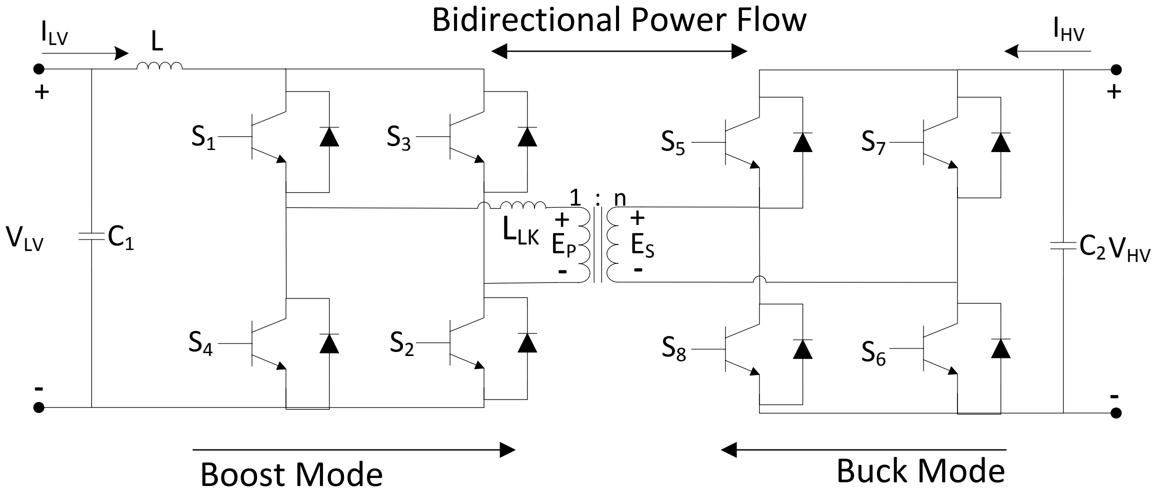

Figure 3-7. Bidirectional DC-DC Converter

The gating signals and key operating waveforms as well as the converter current paths for the boost and buck modes of operation for the bidirectional DC-DC converter are presented in Figure 3-8, Figure 3-9, Figure 3-10, and Figure 3-11 respectively. The currents I_{HV} and I_{LV} are measured using the reference of ‘going into the converter’ as the positive direction, which is why I_L is negative in buck mode and positive in boost mode. In boost mode only one current wave form is displayed, Figure 3-8, because the ideal input current is also the inductor current. I_{HV} represents the current entering/leaving the high voltage side of the converter, I_{LV} is the current entering/leaving the low voltage side of the converter and I_L is the current through the choke inductor, L. The gating signals shown in Figure 3-8 and Figure 3-10 are based off of those presented in [57].

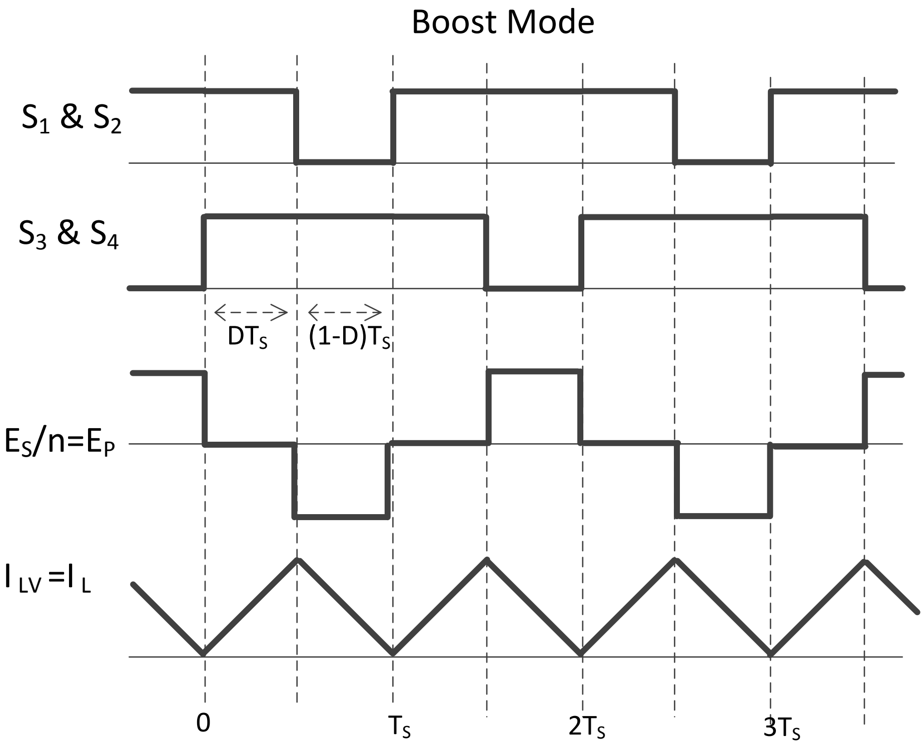

Figure 3-8. Bidirectional DC-DC Converter Boost Mode Operating Waveforms

In boost mode the bidirectional DC-DC converter increases the input voltage from the LVDC bus voltage of 800V to the MVDC bus voltage of 4.25 kV. As shown in Figure 3-9 switches 1, 2, 3, and 4 are used to generate a sinusoidal waveform which is then rectified via blocks 5, 6, 7, and 8. In interval 1 the flow of current is shown in Figure 3-9A. During intervals 1 and 3, switches 1, 2, 3, and 4 are all on and power is stored in the choke inductor (*L*). In interval 2, Figure 3-9B, switches 1 and 2 turn off and power is transferred from the low voltage side through the transformer, rectified via blocks 7 and 8 and transferred into the load. Interval 4, Figure 3-9C, once again transfers power stored in the choke inductor to the load.

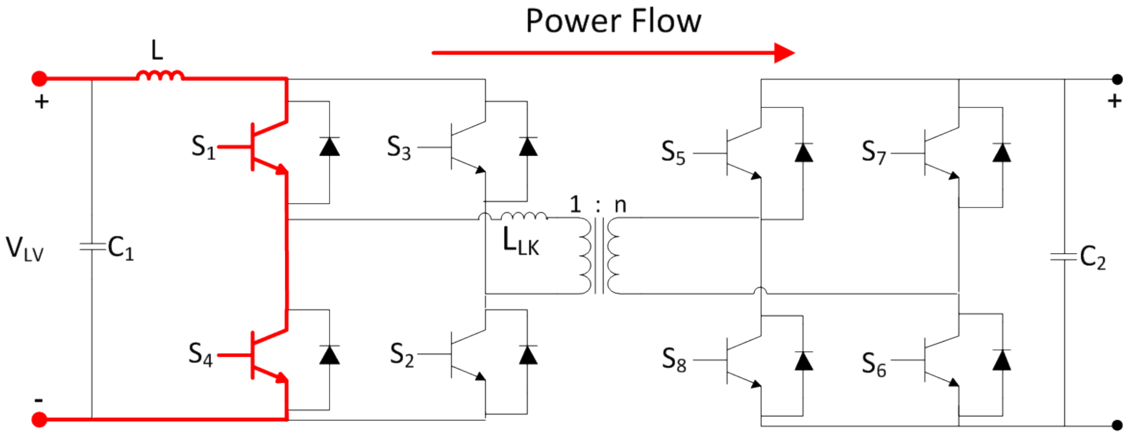

(A) Interval 1: $0 < t < DT_S$ / Interval 3: $T_S < t < (T_S + DT_S)$

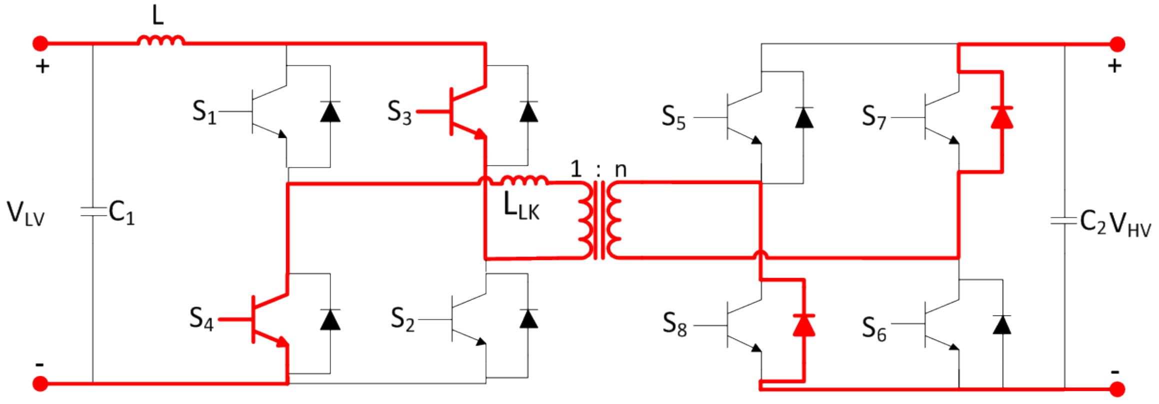

(B) Interval 2: $DT_S < t < T_S$

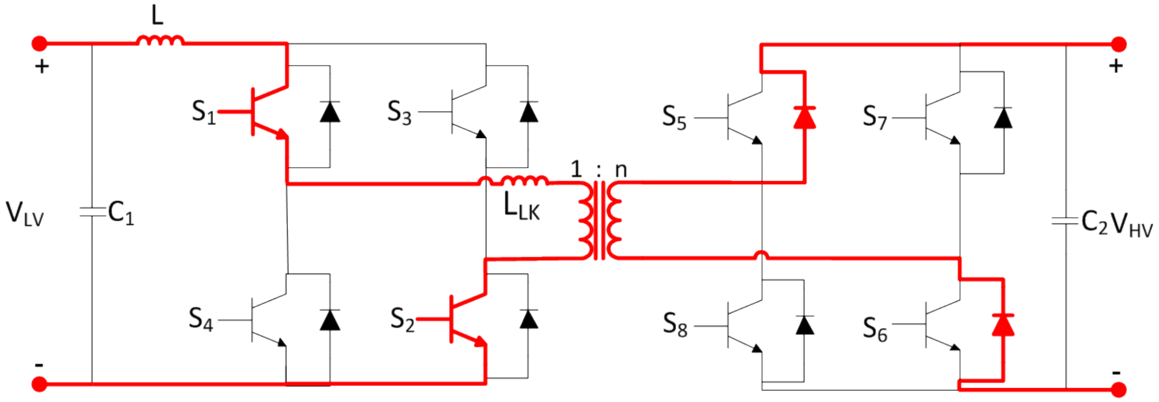

(C) Interval 4: $(T_S + DT_S) < t < 2T_S$

Figure 3-9. Boost Mode Converter Current Paths for Operating States

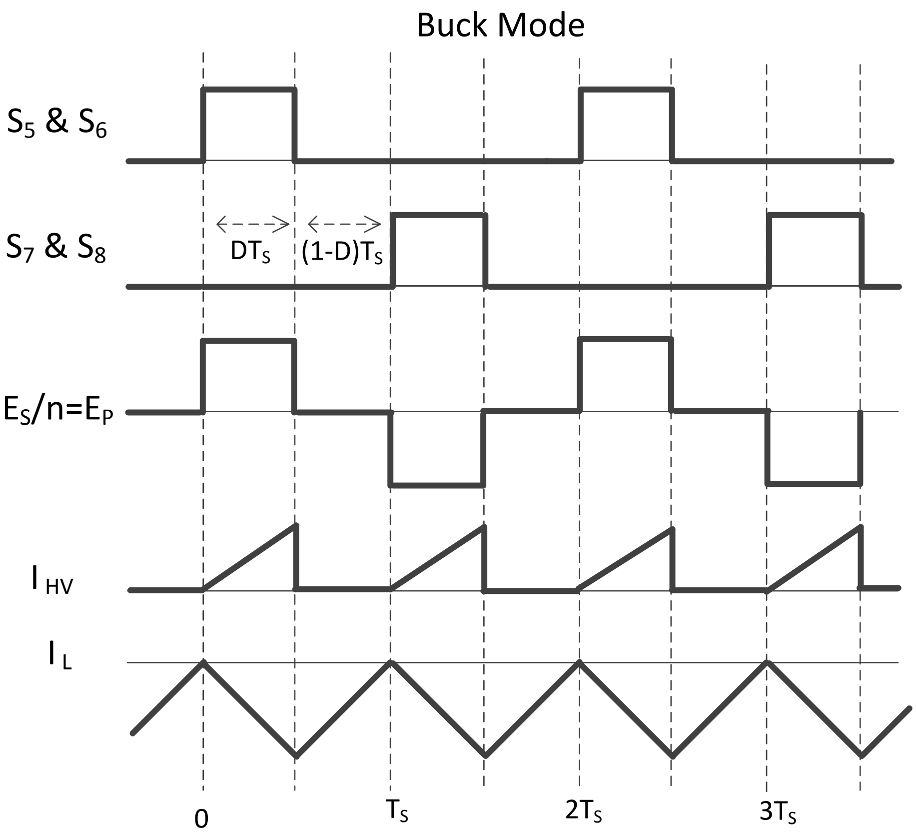

Figure 3-10. Bidirectional DC-DC Converter Buck Mode Operating Waveforms

In buck mode the bidirectional DC-DC converter reduces the input voltage from the MVDC bus voltage of 4.25 kV to the LVDC bus voltage of 800 V. As shown in Figure 3-10, switches 5, 6, 7, and 8 are used to generate a sinusoidal waveform which is then rectified via blocks 1, 2, 3, and 4. In interval 1 the flow of current is shown in Figure 3-11A. During interval 1, power is transferred from the high voltage side through the transformer and stored in the choke inductor (*L*). In Interval 2 and 4, Figure 3-11B, all switches are off and power is cycled through the primary side of the circuit and onto the LV bus. Interval 3, Figure 3-11C, once again transfers power from the high voltage side of the circuit and stores it in the choke inductor.

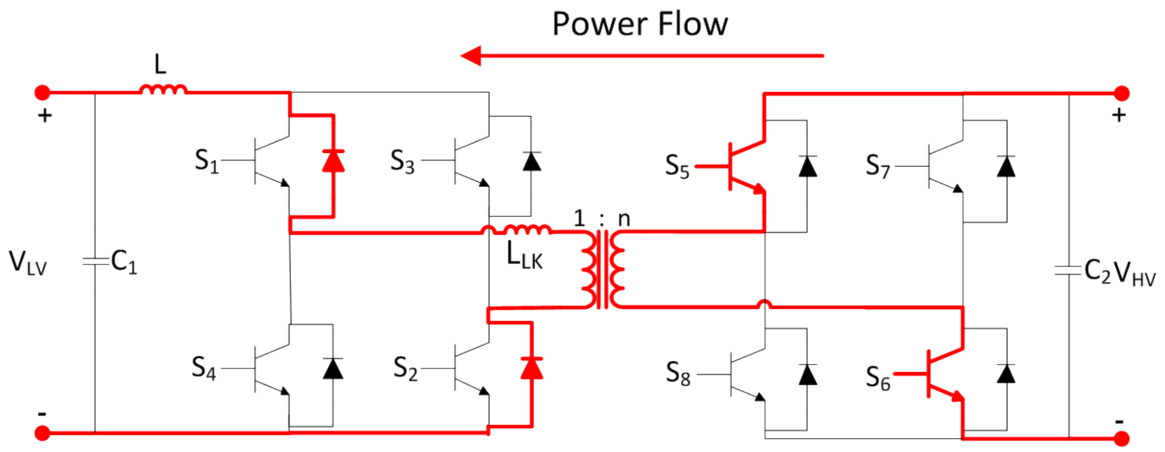

(A) Interval 1: $0 < t < DT_S$

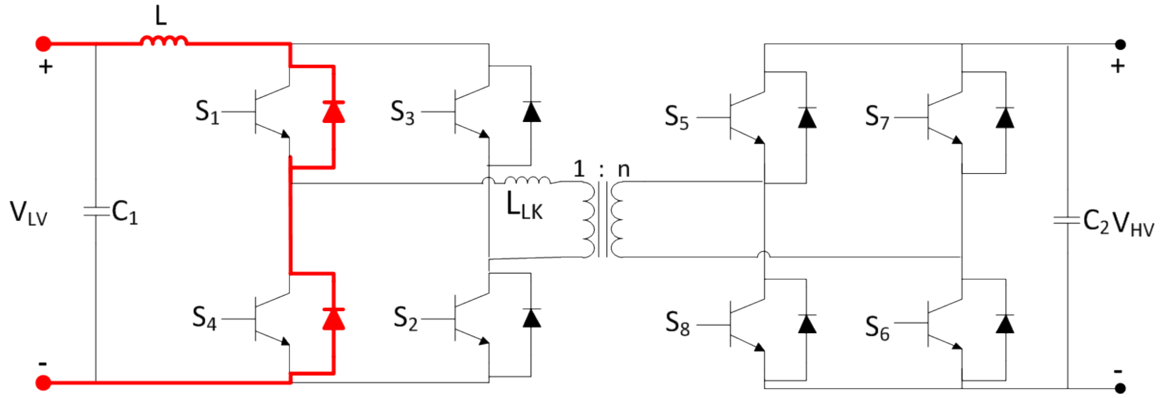

(B) Interval 2: $DT_S < t < T_S$ / Interval 4: $(T_S + DT_S) < t < 2T_S$

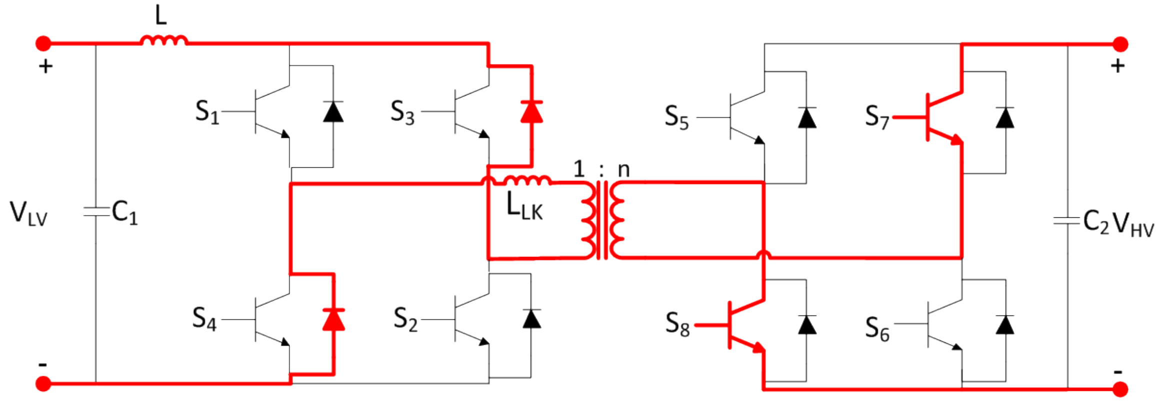

(C) Interval 3: $T_S < t < (T_S + DT_S)$

Figure 3-11. Buck Mode Converter Current Paths for Operating States

In order to predict the steady state output of the converter, inductor volt-seconds balance, capacitor charge balance, and the small-ripple approximation are utilized in determining the average output voltage and current [58]. Analysis is performed using the buck mode operating states presented in Figure 3-11. During interval 1, Figure 3-11A, KVL was performed to calculate the voltage across the choke inductor (v_L), (3.8). KCL was performed at the node above C_1 to calculate the current through the capacitor (i_C), (3.9)

$$v_L = \frac{V_{HV}}{n} - V_{LV} \tag{3.8}$$

$$i_C = I - \frac{V}{R} \tag{3.9}$$

During interval 2, Figure 3-11B, KVL and KCL were again performed at the same points yielding the voltage across the choke inductor, (3.10), and the current through the capacitor, (3.11).

$$v_L = -V_{LV} \tag{3.10}$$

$$i_C = I - \frac{V}{R} \tag{3.11}$$

Performing, KVL and KCL during interval 3 Figure 3-11C, and interval 4, Figure 3-11B, yields the same results as in (3.8) / (3.9) and (3.10) / (3.11) respectively. Utilizing the properties of volt-seconds balance and capacitor charge balance the average inductor voltage, $<v_L>$ and average capacitor current, $<i_C>$, are calculated. Equation (3.12) shows the calculation of average inductor current over one switching period, which is then employed to calculate the output voltage V_{LV}, (3.13), given the input voltage (V_{HV}), the duty cycle (D), and the transformer turns ratio (n).

$$\langle v_L \rangle = \frac{1}{T_S}\int_0^{T_S} v_L(t)dt$$

$$\langle v_L \rangle = \frac{\left(\frac{V_{HV}}{n} - V_{LV}\right)DT_S + \left(-V_{LV}\right)D'T_S}{T_S} \tag{3.12}$$

$$V_{LV} = \frac{V_{HV}D}{n} \tag{3.13}$$

The calculation of average capacitor current over a switching period is shown in equation (3.14). (3.15) is simplified to calculate the DC value of the inductor current (*I*), given the output voltage (V_{LV}) and the load resistance (*R*).

$$\langle i_C \rangle = \frac{1}{T_S}\int_0^{T_S} i_C(t)dt$$

$$\langle i_C \rangle = \frac{\left(I - \frac{V}{R}\right)DT_S + \left(I - \frac{V}{R}\right)D'T_S}{T_S} \tag{3.14}$$

$$I = \frac{V_{LV}}{R} \tag{3.15}$$

In buck mode, the bidirectional DC-DC converter provides voltage regulation for the LVDC bus. The regulation is accomplished utilizing voltage feedback control, Figure 3-12. The controller measures the LVDC bus voltage and compares it to a reference value. A PI block is used to adjust the converters steady-state error and response time. A reference carrier operating at (T_S/2) compared with the PI blocks output is used to generate the systems gating signals

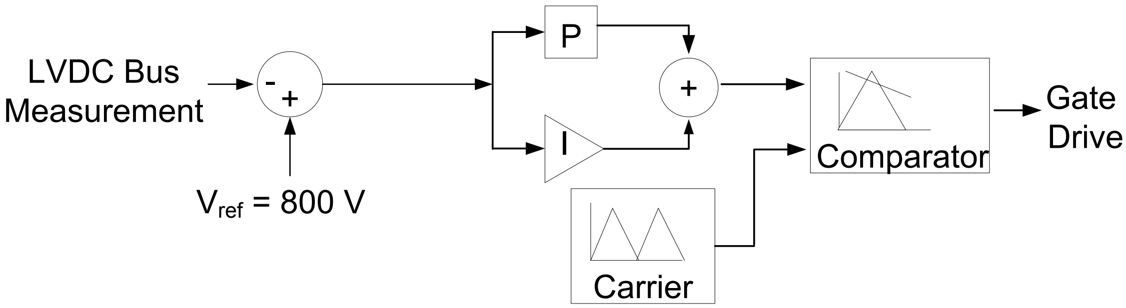

Figure 3-12. Controller for Bidirectional DC-DC Converter Buck Mode Voltage Regulation

In the interconnected model, due to limited power within the system, the need for a pre-charge circuit was emphasized. The pre-charge circuit limits the input capacitor's (C2) inrush current, which is needed due to the fact that an uncharged capacitor behaves as a short circuit, which in turn leads to a collapse of the MVDC bus. In this simulation the simplest form of pre-charge circuit is utilized. Two resistors are added in series with the capacitor, Figure 3-13, to limit the inrush current and are removed via a switch once the DC link capacitor reaches the appropriate level of charge. Also, notice the addition of the damping circuit to the bidirectional dc-dc converter shown in Figure 3-13, the damping circuit consisting of a damping resistor (R_{Damp}) and a controlled switch (S_D), which is used to actively limit the bus voltage during transient loss of load and steady state no load conditions, minimizing overshoot and steady state error. Table 5 contains the operating parameters of all components in the bidirectional DC-DC converter, these components are based off of the values presented in [48].

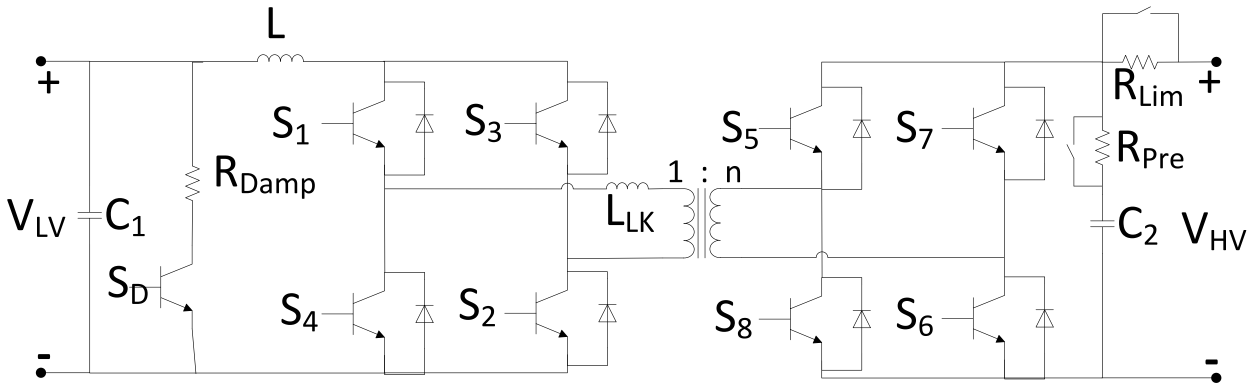

Figure 3-13. Bidirectional DC-DC Converter with Pre-charge Circuit and Damping Circuit

Table 5. Operating Parameters Bidirectional DC-DC Converter

Choke Inductance (*L*)	1 mH
Leakage Inductance (L_{LK})	27 µH
Low Voltage Filter Capacitor (C_1)	2 mF
High Voltage Filter Capacitor (C_2)	2.7 mF
Pre-charge Resistor (R_{Pre})	47 Ω
Inrush Limit Resistor (R_{Lim})	25 Ω
Damping Resistor (R_{Damp})	11 Ω
Transformer Turns Ratio (*n*)	3

3.2.3 Synchronous Buck Converter

The synchronous buck converter is used to simulate the battery charger in the electric vehicle charging station model. The synchronous buck converter, Figure 3-14, is used to regulate the charging power at the desired level (in the case of level 2 DC fast charging, 50 kW). The synchronous buck converter operates similarly to a traditional buck converter. The main difference being that, rather than using a diode to naturally commutate during the *D'* section of the switching period, a second switch (S_2) is used, graphically portrayed in Figure 3-16. To regulate charging power at 50 kW the synchronous buck converter utilizes constant current feedback control, shown in Figure 3-15.

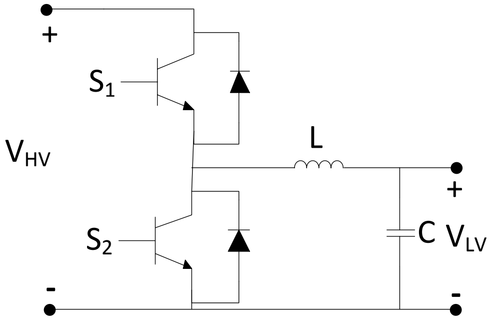

Figure 3-14. Synchronous Buck Converter

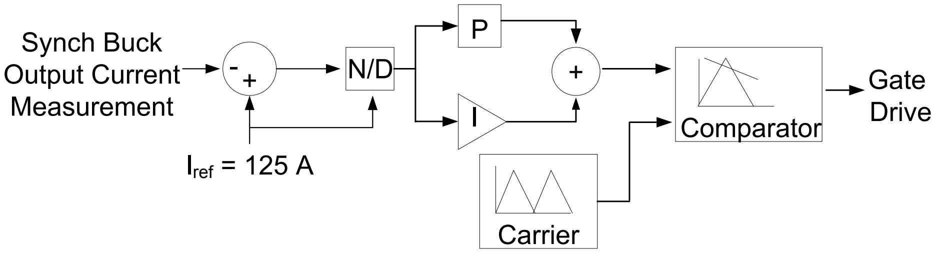

Figure 3-15. Constant Power Feedback Controller

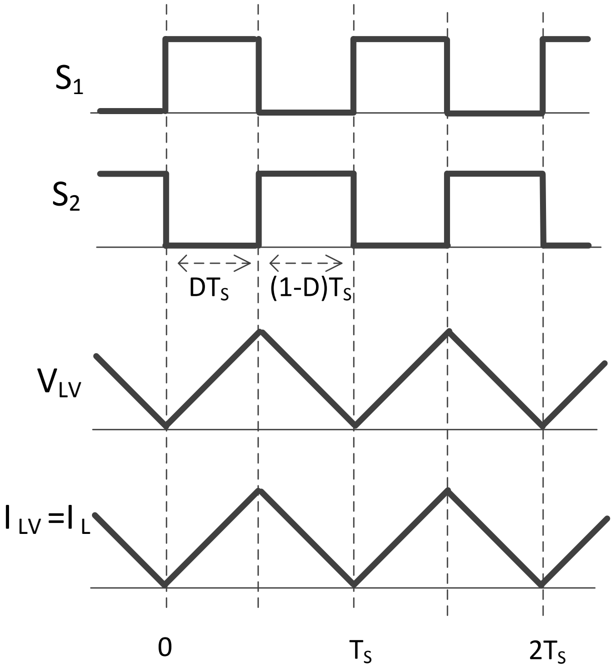

Figure 3-16. Key Operating Waveforms of Synchronous Buck Converter

The main benefit of using a synchronous buck converter over a regular buck converter is the reduced conduction losses due to the use of IGBTs during both portions of the switching period [59]. An example of a synchronous buck converter being used for EV battery charging is implemented in hardware and presented in [60]. The values of L (25.3303 mH) and C (1 μF) were chosen such that they would filter out harmonic content above 1 kHz, according to (3.16), (3.17), and (3.18).

$$\frac{V_O}{V_{in}} = \frac{\omega_o^2}{(j\omega)^2 + \omega_o^2} \tag{3.16}$$

$$\omega_o^2 = \frac{1}{LC} \tag{3.17}$$

$$f_{LP} = \frac{1}{2\pi\sqrt{LC}} \tag{3.18}$$

where:

- ω_o is the cutoff frequency of the filter in rad/s
- f_{LP} is the cutoff frequency of the filter in Hz

3.2.4 **Electric Vehicle Linear Battery Model**

The level 2 DC fast charging is anticipated to be a *game changer* in the EV industry [53]. Traditional EV charging methods such as level 1 and 2 chargers take between four and sixteen hours to fully charge a depleted battery, which is only feasible for overnight or at work charging. Level 2 DC fast chargers allow for charging of a EVs battery in as little as fifteen minutes [53]. A 50 kW level 2 fast charger operating at 400 V_{DC} will have a charging current of 125 A_{DC}.

An example charging profile of a lithium-ion phosphate (LFP) battery which are widely used in automotive applications is presented in Figure 3-17 [54]. A typical battery charge cycle consists of two modes constant current (CC) charging and constant voltage (CV) charging. For a LFP battery used in automotive applications the CC charging time takes 75% of the total charging time and reaches a SOC of approximately 95%. The remaining 25% of the charge time the battery is charged utilizing CV charging. From inspection of the charging profile presented in Figure 3-17, that maximum charging power occurs at the end of CC charging, for this reason the battery charging simulation assumes 90% SOC.

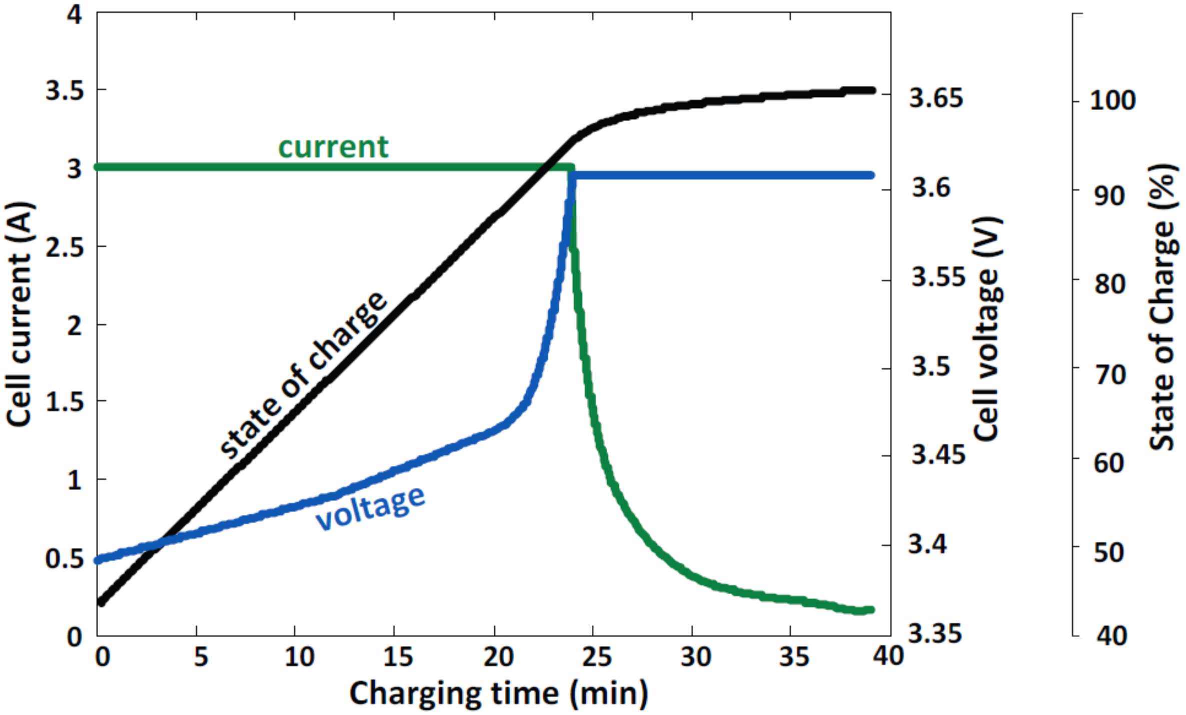

Figure 3-17. Charging Profile for a Lithium-Ion Phosphate Battery [54]

The electric vehicle battery is represented using a linear battery model. The simulation assumes that all vehicles have the same size battery (22.1 Ah). As explained earlier to maximize system load the simulation assumes that the EV batteries are at the end of the CC charging cycle at 95% state of charge. Due to the size and complexity of the entire EVCS and MVDC model, the simulation is only run for a few seconds (2.1 seconds), and during those few seconds the battery is charged for approximately 1.0 second. As shown in Figure 3-17, over any one second interval, the charging of a lithium-ion phosphate battery can be approximated as being linear. The linear battery model used in this simulation, Figure 3-18, consists of a dependent voltage source (*EMF*) in series with a variable resistance (R_{int}).

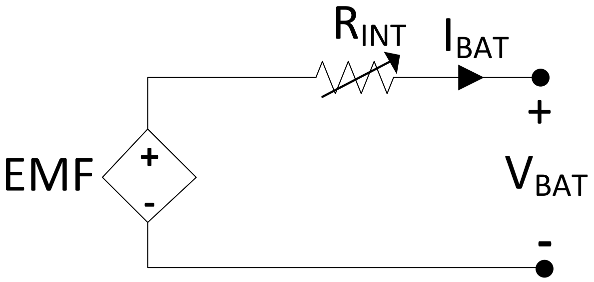

Figure 3-18. Electric Vehicle Linear Battery Model

The linear battery model is designed to have a fully charged terminal voltage of 600 V_{DC} and charge at around 88.3 A_{DC}. Due to constant power charging, the battery will have a higher current at the beginning of charge due to a lower terminal voltage. The electromotive force (*EMF*) and internal resistance (R_{int}) both adjust linearly as a function of the battery's state of charge as shown in (3.19), (3.20), (3.21), and (3.22). State of charge refers to the percentage full the battery is, a SOC of 0.5 represents a battery that is 50% full. The values for V_{min} (battery voltage at 0% SOC), R_{int} (battery internal and terminal resistance), K_V, and K_R (constants determined by battery type) were approximated to yield the desired operation.

$$\text{EMF} = V_{\min} + (K_{\text{V}} SOC) \qquad (3.19)$$

$$R_{\text{int}} = R_{\min} + (K_{\text{R}} SOC) \qquad (3.20)$$

$$Q_e = -\int_0^t I_{bat}(\tau) d\tau \qquad (3.21)$$

$$\text{SOC} = \frac{Q_e}{C_{\max}} \qquad (3.22)$$

The values of *EMF* and R_{int} are both functions of the battery's state of charge (SOC). The battery's extracted charge, Q_e, and SOC are calculated via (3.21) and (3.22). C_{max} is the battery's maximum capacity in Amp-seconds. The linear battery model parameters are presented in Table 6.

Table 6. Operating Parameters Linear Battery Model

Capacity	22 Ah
V_{min}	366 V
R_{min}	1 mΩ
K_v	0.34
K_c	$90*10^{-6}$

3.2.5 **Photovoltaic Array and Boost Converter**

In the electric vehicle charging station model a roof mounted photovoltaic array is modeled and simulated. The PV array serves as a source of on-site generation for the EVCS. The PV array is simulated at the module level, via representation as a current source in antiparallel with a diode and a resistance followed by a resistor in series, Figure 3-19. The equivalent circuit representation of the PV module allows for a piece-wise linear approximation of the PV module's V-I curve. The piece-wise linear approximation allows for accurate simulation at key operating points along the V-I curve. The comparison of the theoretical V-I curve and the one approximated using the equivalent circuit, shown in Figure 3-19, is shown below in Figure 3-20 [4].

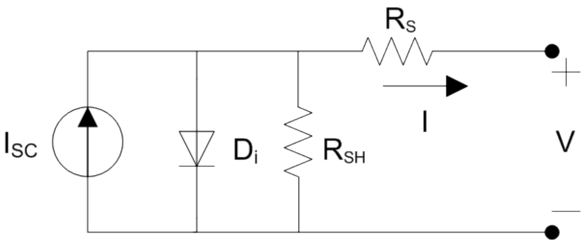

Figure 3-19. PV Array equivalent circuit model [4]

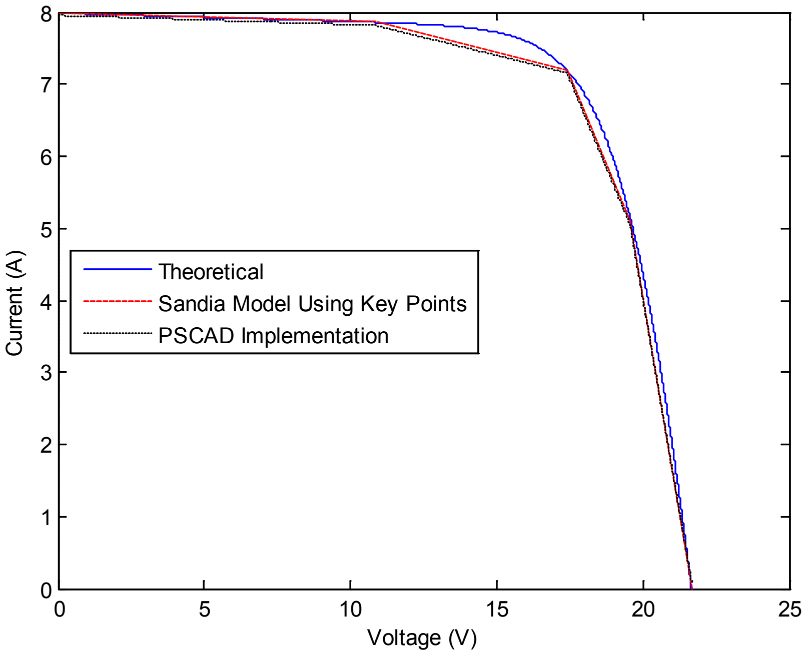

Figure 3-20. Comparison of theoretical and simulated V-I curves for a single PV module [4]

The PV array in the EVCS was designed to output 20 kW. The design specification of the solar modules were taken from production solar panels [61]. The relevant information from the datasheet is presented below in Table 7.

Table 7. Kyocera Solar KC125G Module [61]

Parameter Descriptor	**Parameter Value**
Short-Circuit Current	$I_{sc} = 8.0$ A
Current at $0.5V_{oc}$	$I_x = 7.86$ A
Current for maximum power point	$I_{mp} = 7.2$ A
Current at $0.5(V_{oc} + V_{mp})$	$I_{xx} = 5.1$ A
Open-circuit Voltage	$V_{oc} = 21.7$ V
Voltage for maximum power point	$V_{mp} = 17.4$ V
Number of modules in series to get V_{oc}	$N_{sbase} = 36$
Series resistance of the Sandia model	$R_s = 0.4216\ \Omega$
Shunt resistance of the Sandia model	$R_{sh} = 77.5\ \Omega$

The output of the PV array is scaled utilizing scaling factors n_s and n_p which represent the number of modules connected in series and parallel respectively. The PV array was designed to have a 600 V_{DC} output voltage, and output 20 kW. The output current of the PV array was calculated at 33.3 A_{DC} utilizing P=VI. Each series string of modules produces $17.4 \bullet n_S$ V_{DC} and each string of modules configured in parallel produces $7.2 \bullet n_P$ A_{DC} [4].The calculation of n_s and n_p is shown in equations (3.23) and (3.24).

$$n_S = \frac{600\ V_{DC}}{17.4\ V_{DC}} = 34.48 \approx 35 \qquad (3.23)$$

$$n_P = \frac{33.3\ A_{DC}}{7.2\ A_{DC}} = 4.62 \approx 5 \qquad (3.24)$$

The output of the PV array is conditioned to the proper voltage level for interconnection into the LVDC bus (800 V_{DC}) via a boost converter. The boost converter utilizes a maximum power point tracking (MPPT) algorithm to maintain maximum power output of the PV array at a constant 20 kW. The incremental conductance MPPT algorithm was chosen as the method of MPPT to be utilized in the PV array. According to literature the incremental conductance MPPT is an adequate and superior method of MPTT [62, 63]. Figure 3-21, presents a flow chart of the incremental conductance MPPT algorithm utilized [63]. The incremental conductance algorithm operates by determining the point where the derivative of the power curve for the PV array is zero, which indicates the point of maximum power. The value of L and C were set to 10 mH and 1 mF respectively, these values were chosen to minimize output ripple.

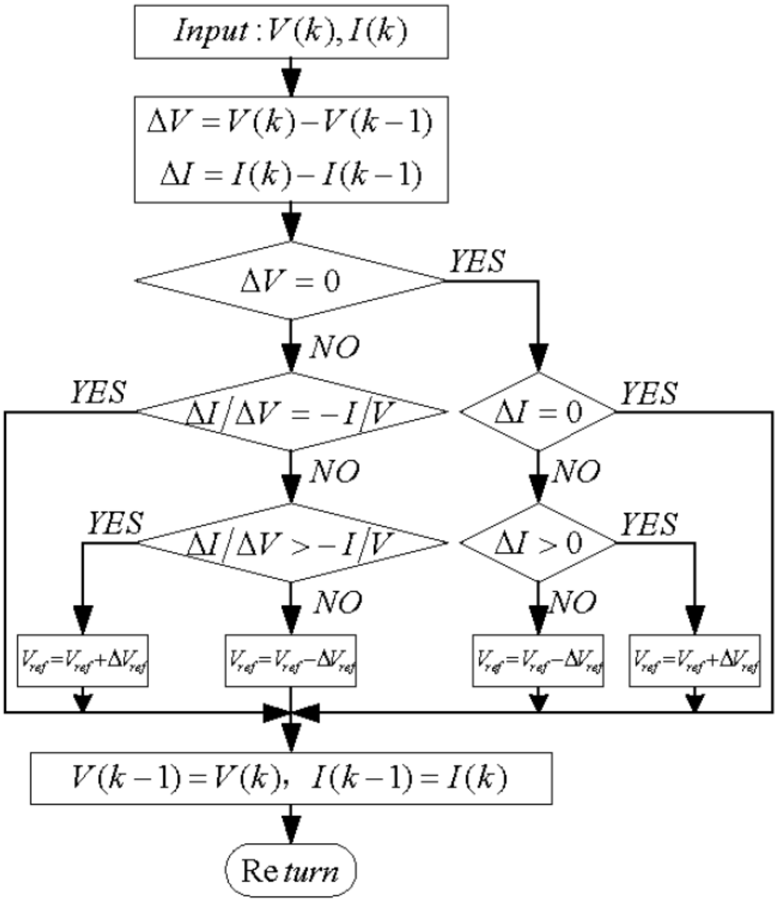

Figure 3-21. Incremental Conductance Maximum Power Point Tracking Algorithm [63]d

4.0 PSCAD COMPONENT VALIDATION

In this chapter individual components within the MVDC, Figure 3-1, and EVCS, Figure 3-5, system models are built within the PSCAD/EMTDC simulation environment and their operation is validated in accordance with the predicted results presented in chapter 3.

4.1 MVDC SYSTEM COMPONENT VALIDATION

Within the MVDC system, the operation of three major components is discussed in chapter 3, and are thus explored and validated in this section, the 5 MW permanent machine synchronous generator (PMSG) wind turbine, the three level neutral point clamped (NPC) converter, and the 10 kW induction machine utilized in the industrial facility model. The design and operation of the MVDC grid is not the primary focus of this thesis and as such will not be discussed in the level of depth and detail that the electric vehicle charging station and related models will. More information on the modeling of the MVDC system components can be found in [4].

4.1.1 **5 MW PMSG Wind Turbine**

Figure 4-1, shows the mechanical and electrical output power of one wind turbine verifying the 5 MW output power in the interconnected model. In the simulation the 5 MW PMSG wind turbines are all designed to operate at their maximum output power and do not vary during simulation. As such, all three wind turbines have the same output as the one presented in Figure 4-1.

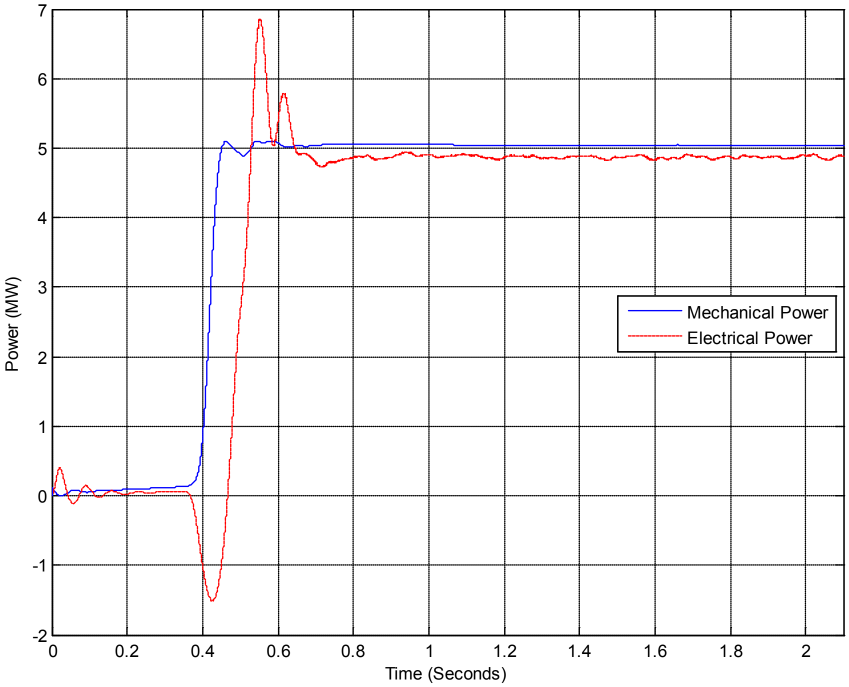

Figure 4-1. Mechanical and Electrical Output Power of Permanent Machine Synchronous Generator

4.1.2 **Three Level NPC Converter**

Figure 4-2, displays the line-to-line input voltage of the three level NPC rectifiers. The number of steps in the line-to-line voltage for an *n* level NPC converter, can be determined as *2n-1*. Since the converter utilizes a three topology, the expected number of steps is 5 [4].

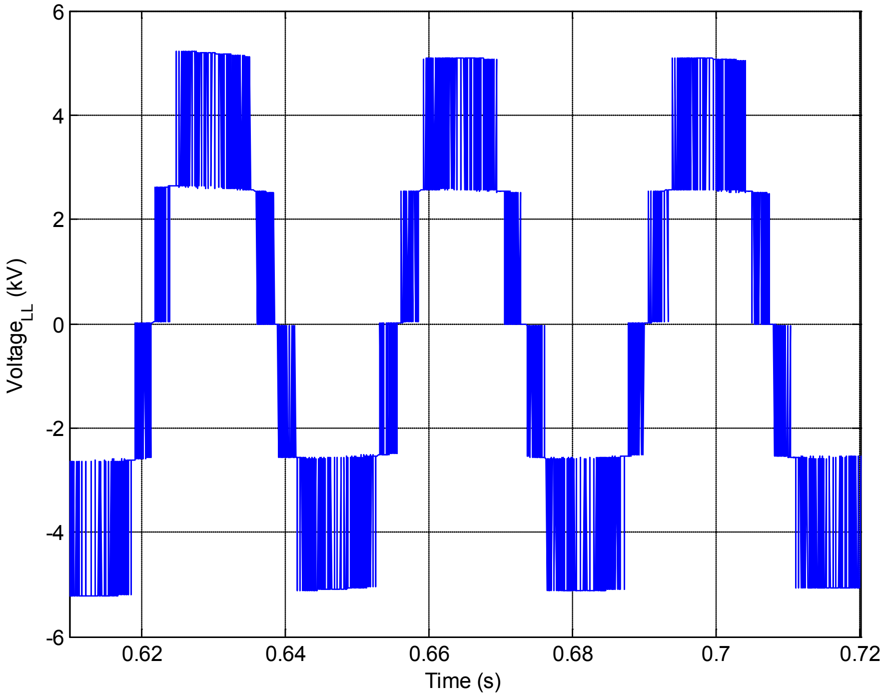

Figure 4-2. Line-to-Line Input Voltage of Three Level NPC Rectifier

4.1.3 **10 kW Induction Machine**

Figure 4-3, provides a graph showing the instantaneous power into the induction machine during simulation. The breakers to the industrial facility close at 0.5 seconds connecting the industrial facility to the MVDC grid, which is why the power is zero before 0.5 seconds. Notice that the machine quickly regulates to a steady state value of 10 kW as desired. The industrial facility contains two 10 kW induction machines and each operates in the same manner.

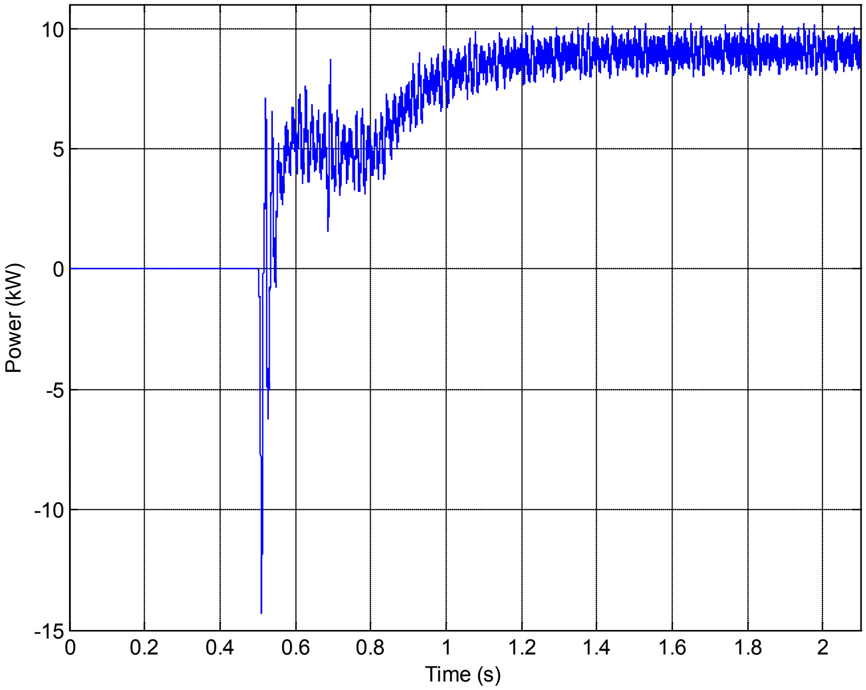

Figure 4-3. Instantaneous Power Absorbed by Each Induction Machine

4.2 EVCS SYSTEM COMPONENT VALIDATION

Within this section, the operation of the PSCAD based models of the individual components within the electric vehicle charging station (EVCS) is validated. The modeling and operation of five main components is discussed and validated in accordance with the operation described in chapter 3. These five main components include the bidirectional DC-DC converter, the synchronous buck converter, the linear battery model, the boost converter, and the photovoltaic array. Figure 4-4, shows the PSCAD model of the EVCS. Each of the individual components is represented as a page module. The model shown in Figure 4-4 is specifically for the non-interconnected case; however, in the interconnected model the ideal voltage sources at high side of the bidirectional DC-DC converter are replaced with connections to the MVDC bus. The 1 nΩ resistors throughout the model are added so that certain nodes are not shorted. The DC system is grounded via capacitive coupling on both the positive and negative rails at all sources and loads.

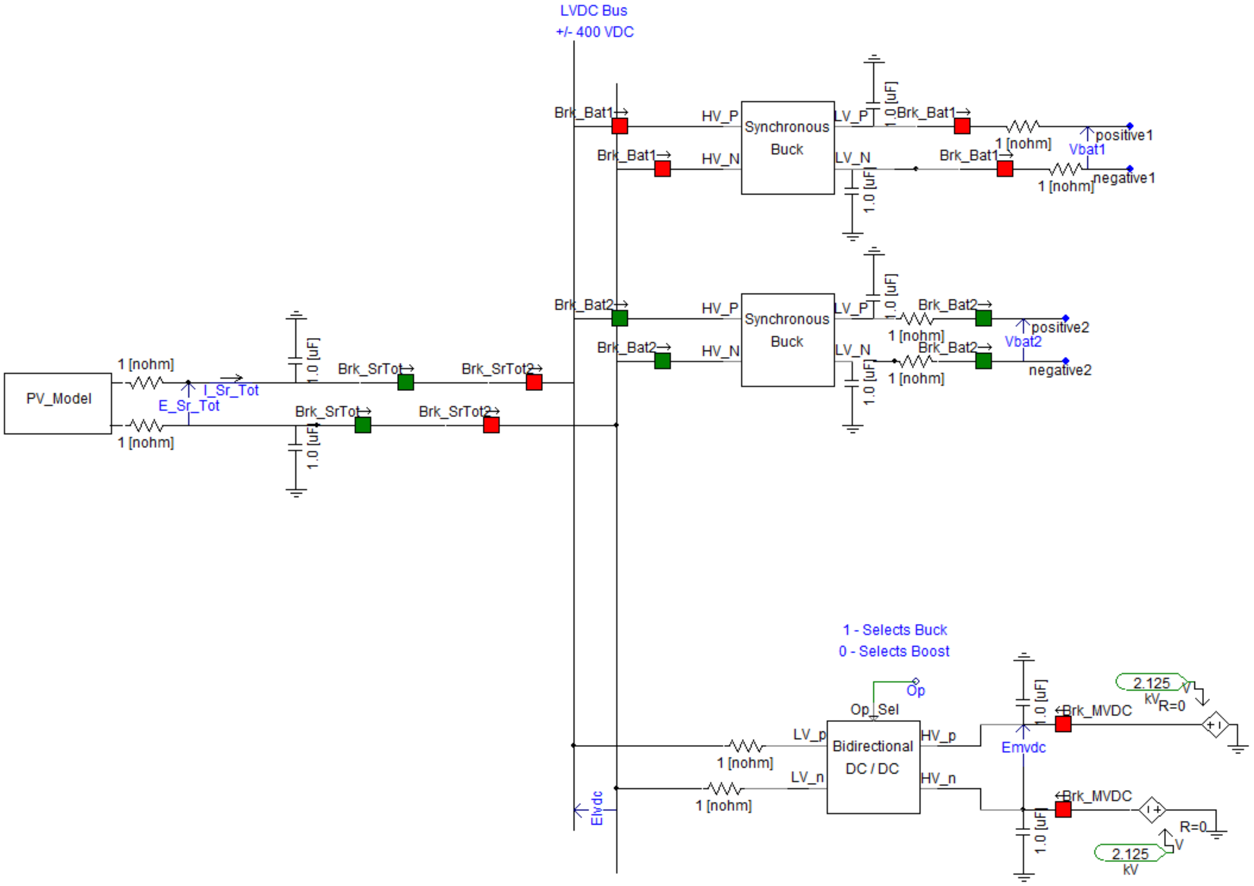

Figure 4-4. EVCS PSCAD Implementation

4.2.1 Bidirectional DC-DC Converter

The bidirectional DC-DC converter is analyzed analytically in section 3.2.2, this section serves to validate the operation of the bidirectional DC-DC converters buck mode of operation in PSCAD utilizing the theoretical analysis performed in section 3.2.2. The waveforms presented in this section are compared against the ones theoretically predicted in Figure 3-10. Figure 4-5, shows the bidirectional DC-DC converter as it was represented in PSCAD as well as where measurements were performed. Notice that the inrush and pre-charge resistors were represented as variable resistances. After the DC link capacitor C2 reaches a desired level of charge they are changed to 1 nΩ, essentially a short circuit.

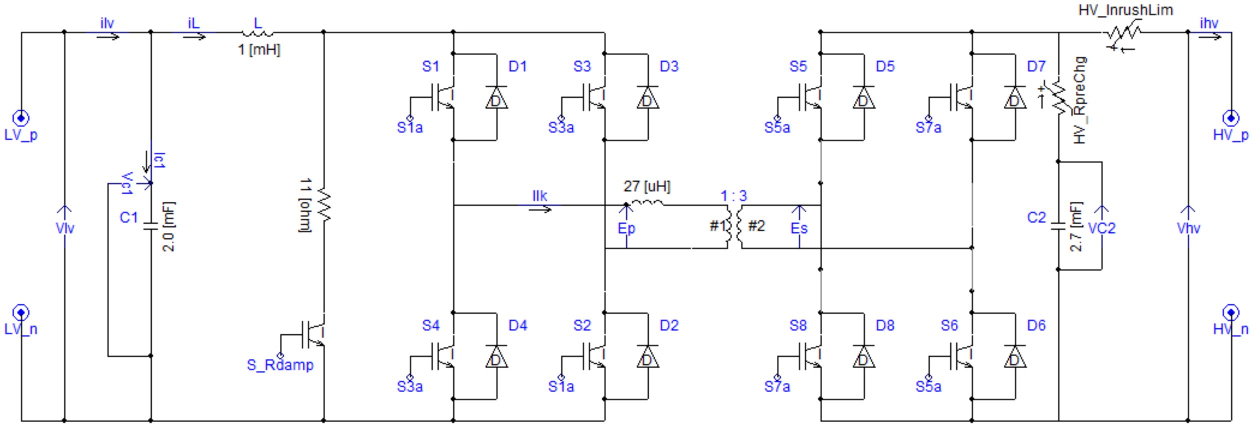

Figure 4-5. Bidirectional DC-DC Converter PSCAD Implementation

The contestant voltage feedback controller is implemented in PSCAD as shown in Figure 4-6. In buck mode, the LV side of the converter is used as a passive rectifier and the IGBTs are set to off the entire time. The HV side utilizes PWM to generate the desired AC wave. The time delay block is utilized so that S_7 and S_8 actuate exactly one switching period after S_5 and S_6.

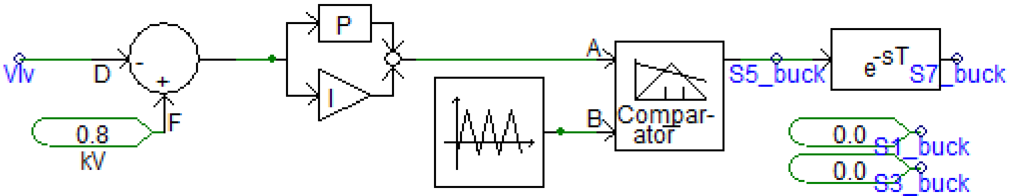

Figure 4-6. Bidirectional DC-DC Converter Buck Mode Constant Voltage Controller

As derived in section 3.2.2, the equation determining the average output voltage (V_{LV}) given a set input voltage (V_{HV}), duty cycle (D) and turns ratio (n) is (4.1). (4.1) can be rewritten as (4.2) to allow for the calculation of the duty cycle. Using $V_{LV} = 800$ V, $V_{HV} = 4.25$ kV, and $n = 3$, D is calculated using (4.2) to be 0.565.

$$V_{LV} = \frac{V_{HV} D}{n} \tag{4.1}$$

$$D = \frac{n V_{LV}}{V_{HV}} \tag{4.2}$$

Figure 4-7, shows the gating signals for the buck mode operation of the converter during steady state operation. Using the gating signals from the steady state operation of the PSCAD model of the converter, the duty cycle is measured to be 0.552. This is close to the theoretically calculated value of 0.565. The difference is caused by the fact that at steady state the converter has a low frequency ripple, caused by various interacting controllers and system dynamics, super imposed over the high frequency (2 kHz) switching ripple.

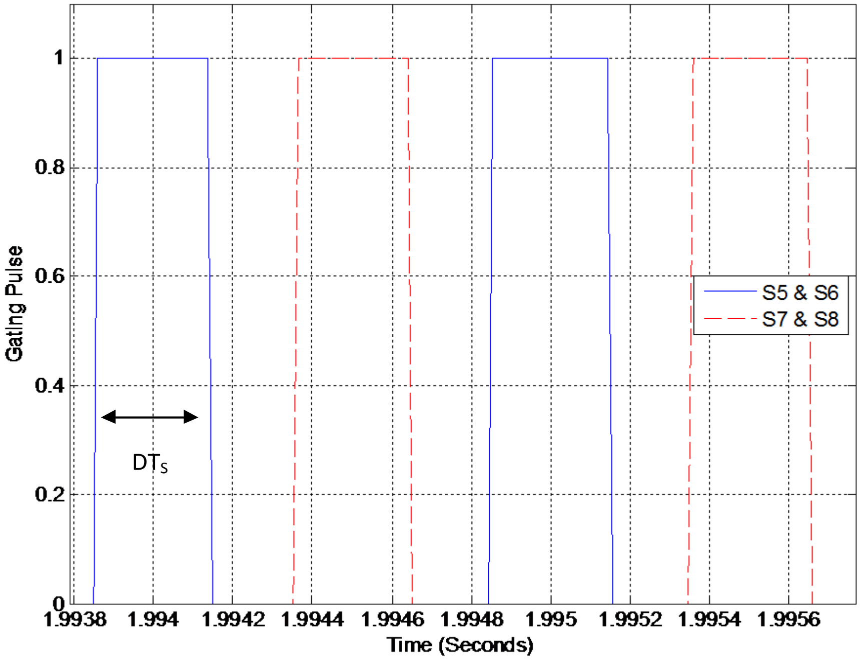

Figure 4-7. Buck Mode Gating Signals

The primary (EP) and secondary (ES) winding voltages across the high frequency transformer are presented in Figure 4-8. During the "ON" period of the high voltage side switches, a +/- VHV is applied across the primary winding of the transformer. When S5 & S6 are

"ON" a + VHV is applied across EP and during the next switching period when S7 & S8 are "ON" a - VHV is applied across EP. In the simulated cases VHV is 4.25 kV. The voltage across the secondary winding should be EP/n, in the case of the simulated converter, n is equal to 3, meaning that ES should approximately be equal to 1.4 kV.

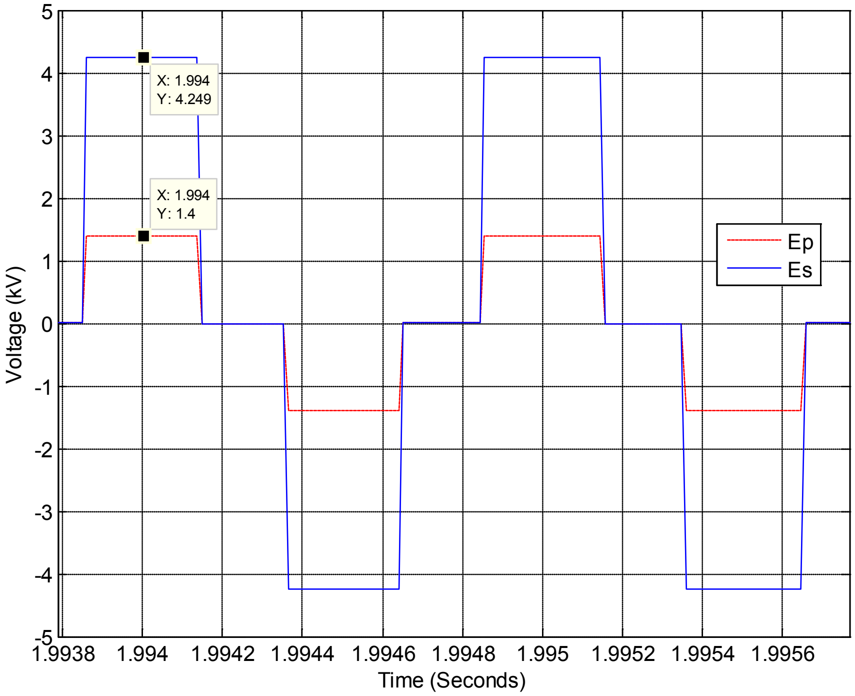

Figure 4-8. Primary Side Voltage (E_P) and Secondary Side Voltage (E_S)

Figure 4-9, presents the choke inductor current ripple over four periods of operation. When the "ON" interval of the switching period, either S_5 & S_6 are "ON" or S_7 & S_8 are "ON", the inductor current decreases about 180 A from a peak of approximately 190 A to a minimum of approximately 13 A. Then during the "OFF" interval the current increases by approximately the same amount so that the average current over any one period is zero maintaining the inductor volt-seconds balance theory. Even though the system is operating at steady state in Figure 4-9,d there is a low frequency ripple superimposed over the high frequency (2 kHz) switching ripple which makes it so that between switching periods the converter does not reach the same peak currents.

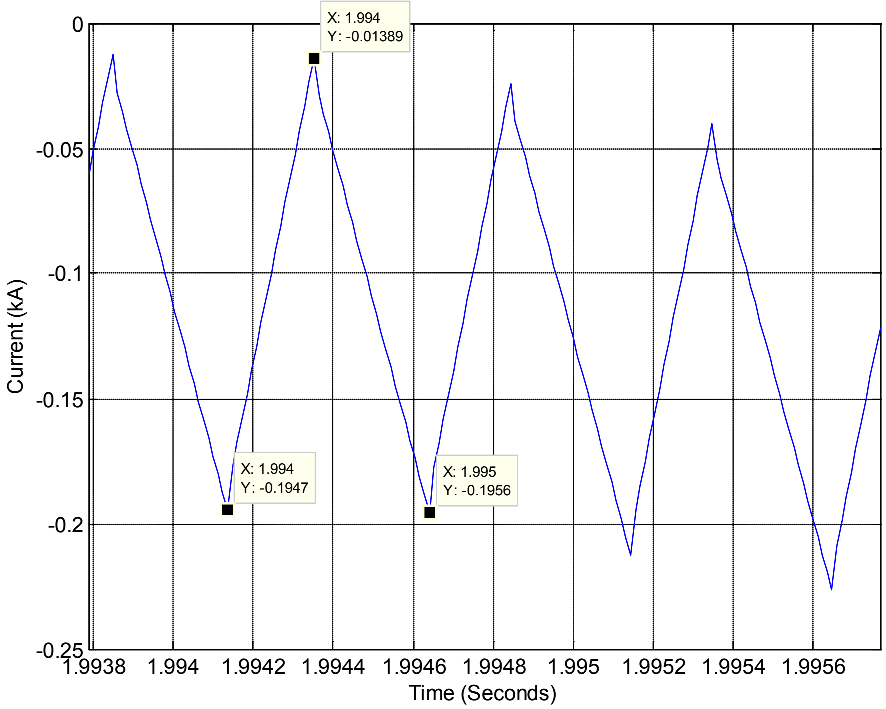

Figure 4-9. Choke Inductor Current (i_L)

The transformer leakage inductance current (i_{LK}) is shown in Figure 4-10. The leakage inductance current is non-zero only during the "ON" interval of the switching period and is during that time the current that is flowing through the choke inductor. During the S5 & S6 "ON" intervals, the leakage inductor current is exactly equal to the choke inductor current. Conversely, during S7 & S8 "ON" interval, the leakage inductor current is the negative of the choke inductor current. This is caused by the polarity difference across the transformer which is graphically represented via the operating paths shown in Figure 3-11.

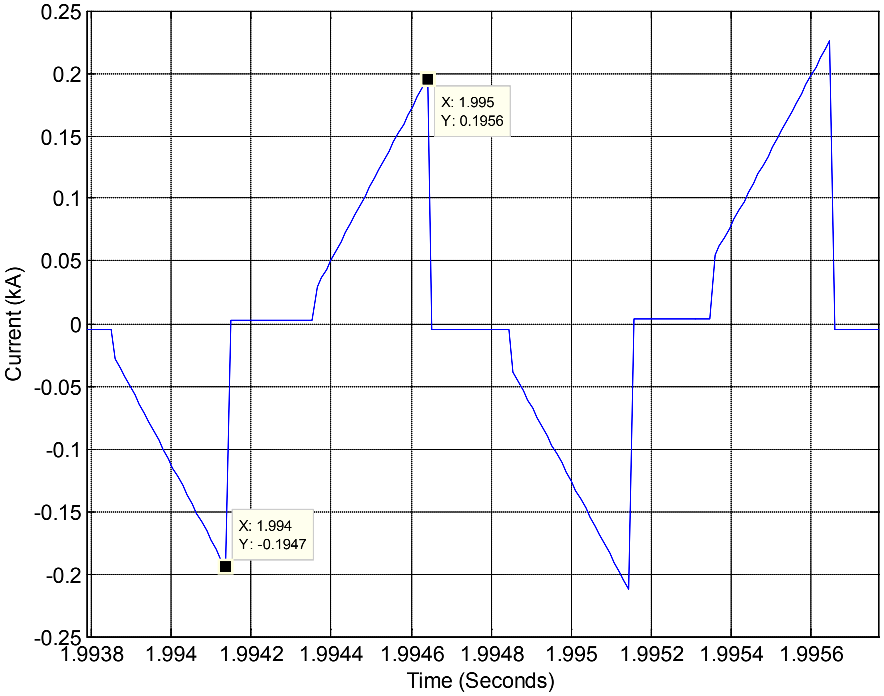

Figure 4-10. Leakage Inductance Current (i_{LK})

The bidirectional DC-DC converters buck mode input current (i_{HV}) over four switching periods is presented in, Figure 4-11. The input current exists during the "ON" interval of the switching period only, as illustrated in Figure 3-11. The current in the low voltage side of the circuit is approximately equal to ni_{HV}.

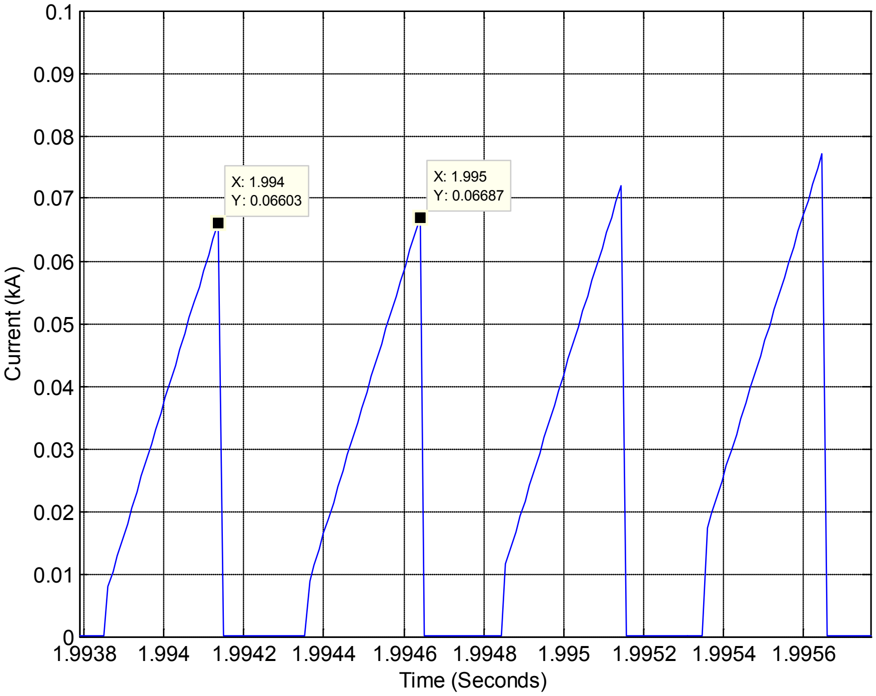

Figure 4-11. High Voltage Side Input Current (i_{HV})

4.2.2 Synchronous Buck Converter

The theoretical operation of the synchronous buck converter is presented in section 3.2.3. This section will show that the PSCAD implementation of the synchronous buck converter is in agreement with the predicted theoretical operation. The PSCAD model for the synchronous buck converter is presented in Figure 4-12. The one nΩ resistor is necessary so that the two electrical connections HV_N and LV_N are not connected to the same node. When two electrical connections are connected to the same node an error is created in PSCAD.

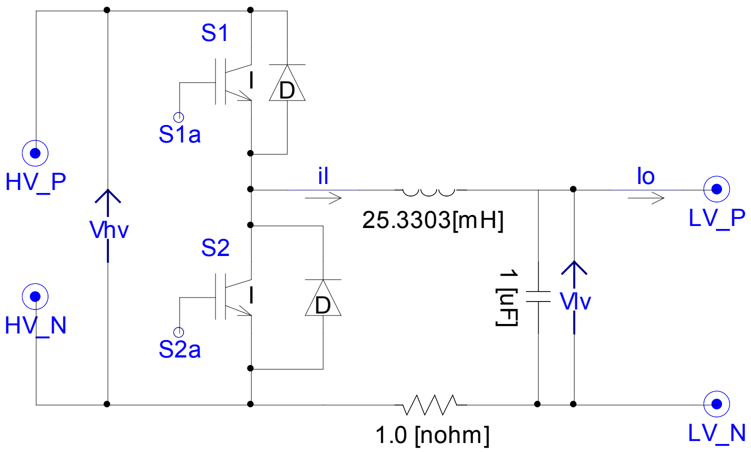

Figure 4-12. Synchronous Buck Converter PSCAD Implementation

The synchronous Buck Converter utilizes constant current control to output the desired charging current for the electric vehicle batteries. The feedback controller is also utilized to generate the gating signals for the converter.

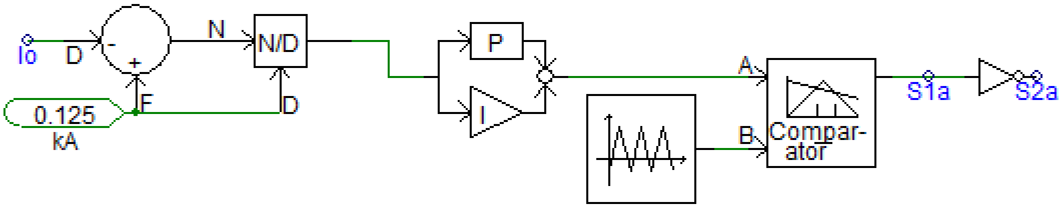

Figure 4-13. Synchronous Buck Converter Controller and Gating Signal Driver

The synchronous buck converter output voltage and current have a triangular ripple which are both in phase and have a positive slope when S_1 is “ON” and a negative slope when S_2 is “ON”. This is illustrated in Figure 3-16. The synchronous converters output voltage is presented in Figure 4-14, and the output current is presented in Figure 4-15. These operate as expected and provide an average output power of approximately 50 kW.

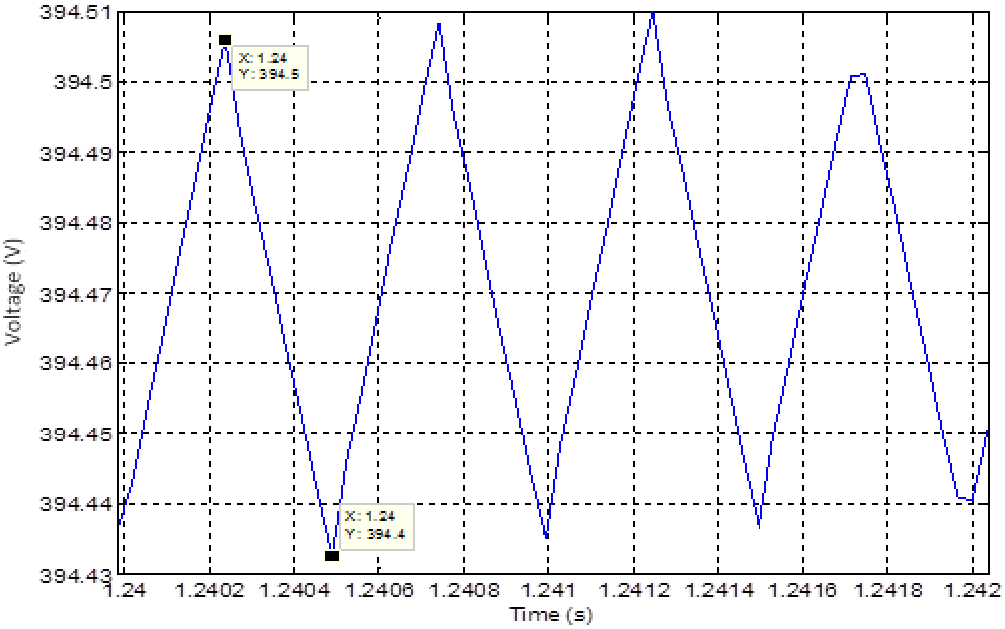

Figure 4-14. Synchronous Buck Converter Output Voltage (V_{LV})

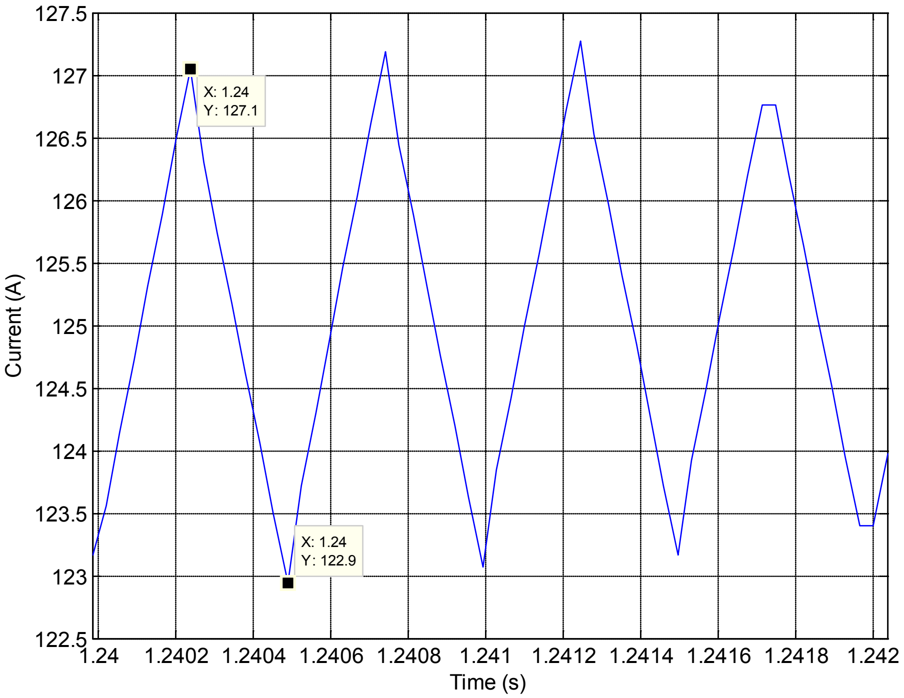

Figure 4-15. Synchronous Buck Converter Output Current (I_{LV})

4.2.3 Linear Battery Model

The linear battery model is used to simulate the battery of the electric vehicle. It is represented as a variable voltage source in series with a variable resistance, both of which vary linearly with the batteries present state of charge. The linear battery model is represented in PSCAD as shown in Figure 4-16.

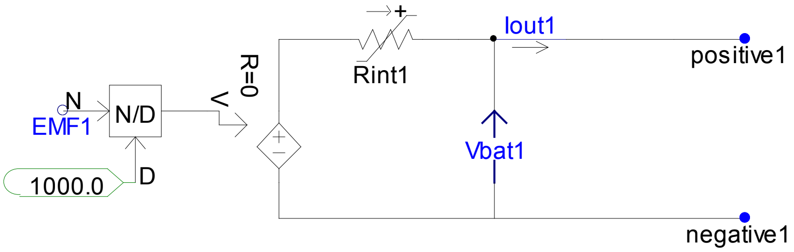

Figure 4-16. PSCAD Implementation of Linear Battery Model

The battery's state of charge (SOC) is calculated in accordance with the equations presented in section 3.2.4. Figure 4-17, is the PSCAD implementation of the equations presented in section 3.2.4.

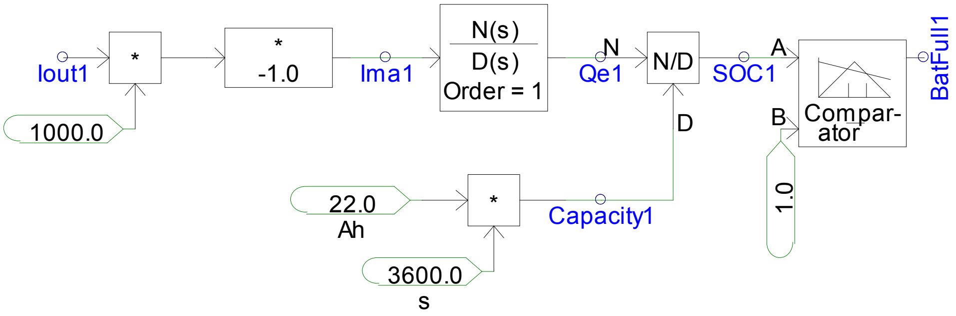

Figure 4-17. PSCAD Calculation of SOC

Figure 4-18 displays the voltage and current for a pulse charge on EV battery 2. The pulse charge lasts for 0.55 seconds. During that time the battery charges at a constant current of 125 A_{DC} and a voltage of about 394.25 V_{DC} (49.3 kW) which is increasing linearly according to the equations presented in section 3.2.4. This pulse charge is captured towards the end of constant current charging at 95% SOC. A reference pulse charge is presented in Figure 4-19, notice how the simulated pulse charge shown in Figure 4-18 matches the general shape of the reference pulse charge. They two pulse charges are not meant to be representative of the same battery the reference pulse charge (Figure 4-19) is charging at a different current, state of charge and voltage than the simulation and will not match perfectly. Only the non-interconnected model battery charging voltage and current is presented.

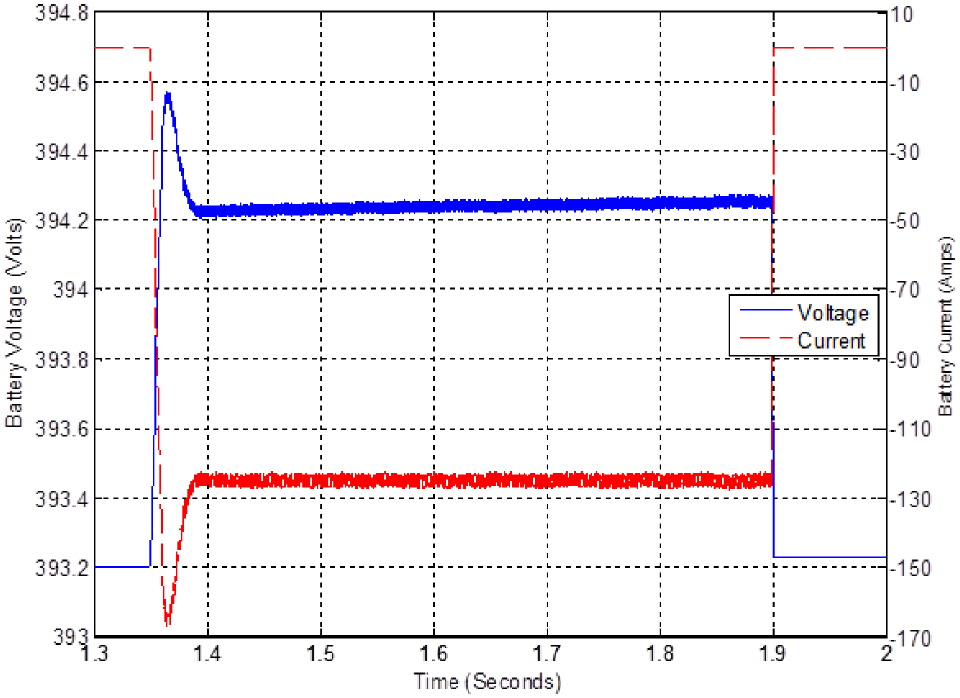

Figure 4-18. EV Battery 2 Pulse Charge Voltage and Current

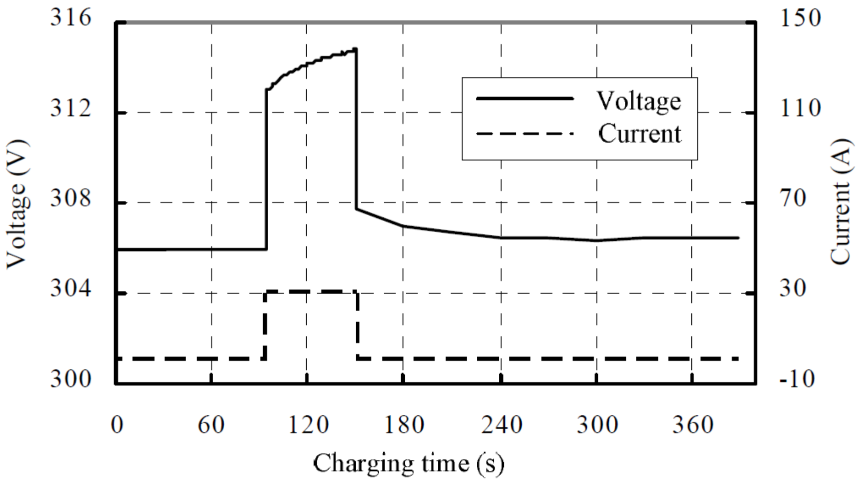

Figure 4-19. Example Li-Ion Battery Pulse Charge [64]

4.2.4 **Photovoltaic Array**

The PV array and boost converter are modeled in PSCAD as shown below in Figure 4-20. The PV array component is a modified version of the generic model shown in Figure 3-19. The three anti-parallel diodes in combination with their parallel resistors are tuned to provide accurate operation and key operating points along the PV's output curve, Figure 3-20. The operation of the PV array is validated in more detail in [4].

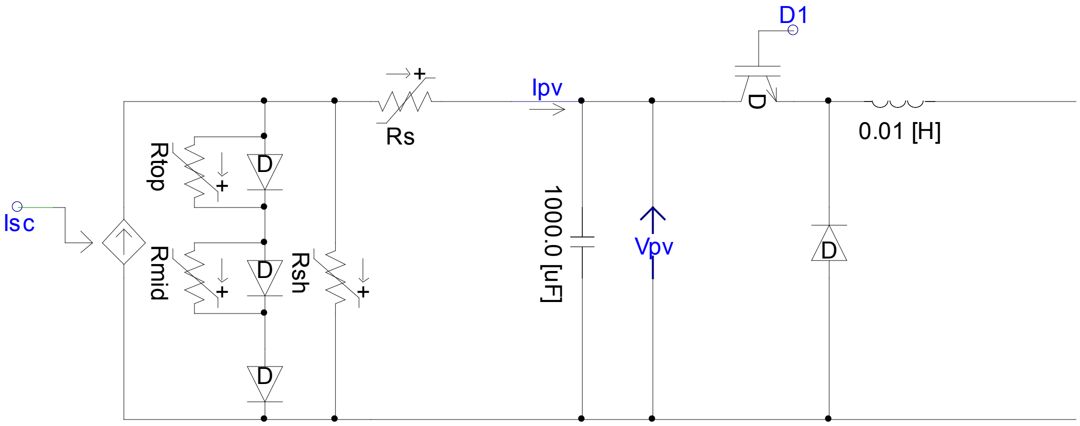

Figure 4-20. PV Array and Boost Converter PSCAD Implementation

The incremental conductance MPPT algorithm was implemented in PSCAD utilizing logic gates as shown in Figure 4-21. The MPPT algorithm is used to calculate the reference voltage which is utilized in determining the duty cycle of the boost converter tied to output of the PV array.

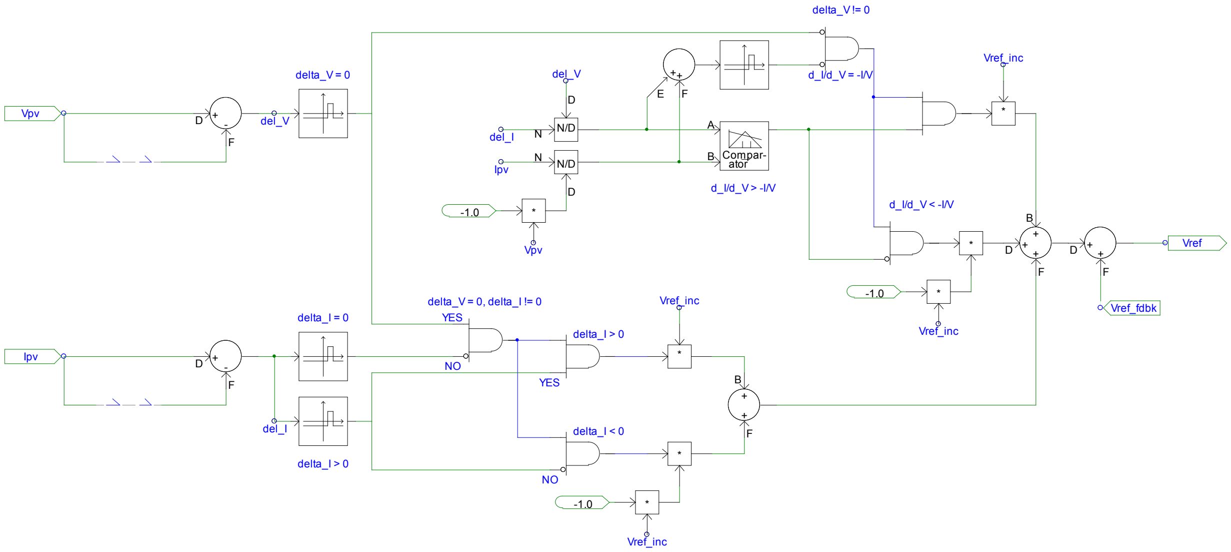

Figure 4-21. PSCAD Implementation of Incremental Conductance Algorithm

Figure 4-22, below shows the output power of the PV array and boost converter in a test system across a 100 Ω load resistor. The PV array output power is slightly higher than the designed 20 kW more around 21 kW. This is due to rounding up of the number of series connected panels. In accordance with the equations in section 3.2.5, the theoretical output power of the PV array is $17.4 \bullet n_S \bullet 7.2 \bullet n_p = 21.9$ kW ($n_p=5$ and $n_s=35$).

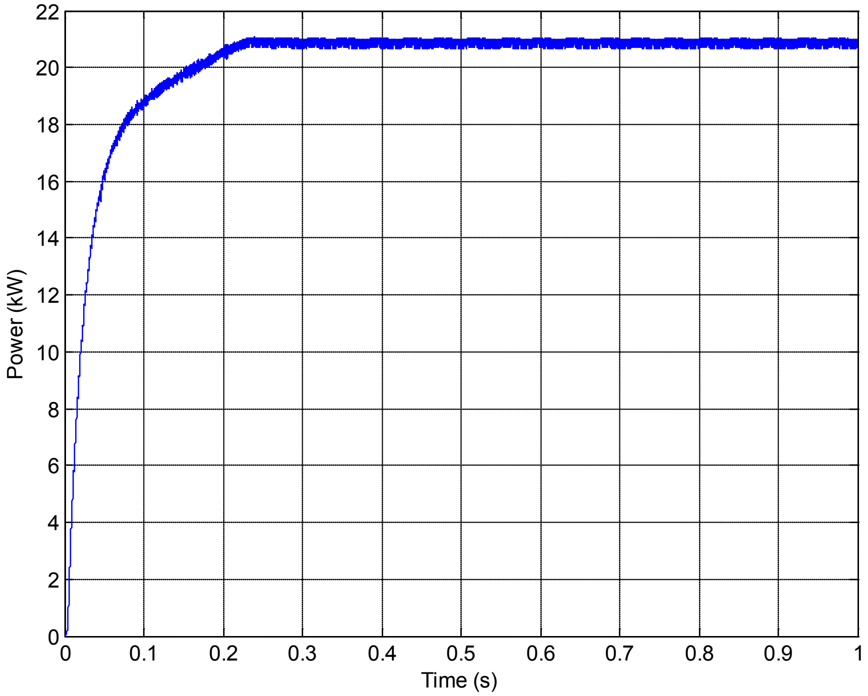

Figure 4-22. PV Array Output Power Test System

5.0 SYSTEM ANALYSIS, OPERATION, AND RESULTS

In Chapter 5, the system level interaction and operation of the electric vehicle charging station with and without interconnection to the full MVDC network will be evaluated during the EVCSs various modes of operation. The electric vehicle charging station has two primary modes of operation, when serving purely as a load (charging of electric vehicles and PV array ON or OFF) and when acting as a source of generation (no EVs present and PV array ON). In this chapter, two models will be referenced, the interconnected model, in which the EVCS is connected to the MVDC grid model, and the non-interconnected model, in which the MVDC grid is represented by an ideal voltage source. The two different models are utilized to validate the use of an ideal voltage source as an appropriate representation of the MVDC grid to allow for quicker and more intricate simulations, as well as determine what problems are unique to the MVDC grid model containing realistic generation sources. In, section 5.2 effect of the battery chargers (synchronous buck converter) operation during a battery pole to pole (short circuit) fault is explored. In particular the ability of the converter to block or propagate the transmission of faults based off of the power electronic switching control is investigated. In, section 5.3, the continuous conduction mode (CCM) and discontinuous conduction mode (DCM) operation of the bidirectional DC-DC converter is discussed as it is not emphasized in literature [48, 57]. In order to accurately simulate and capture the power electronic switching, a small time step is utilized (12μs). A larger solution time step of (30μs) is necessary to reduce the amount of memory required for simulation. All simulations are performed utilizing the same time step previously mentioned. Due to memory limitations caused by the large interconnected model containing five electric machines, ten power electronic converters, a solar array and two battery models, simulation time was limited to 2.1 seconds. The 2.1 second simulation time allows for capturing of transient and steady state operation across all modes of operation.

5.1 RESPONSE OF EVCS WITH AND WITHOUT MVDC GRID MODEL INTERCONNECTION

In Chapter 4.0 the operation of the individual components was validated independently. In section 5.1 the operation of the electric vehicle charging station is validated in all modes of operation, when serving purely as a load (charging electric vehicles), serving purely as a source (supplying power to grid) and combinations of the two. System level simulation of the EVCS, confirms intermeshed component operation, reveals interactions between parallel connected converters, and is utilized to validate the use of an ideal voltage source as an accurate representation of the MVDC grid due to the isolation capability of the isolated bidirectional DC-DC converter. In this chapter, two models will be referenced: the interconnected model, in which the EVCS, Figure 3-5, is powered via direct connection to the MVDC grid model, Figure 3-1, and the non-interconnected model, in which the MVDC grid is represented by an ideal voltage source.

The simulation of the EVCS capturing the various modes of operation is run for 2.1 seconds and follows the operating regime presented in Table 8. The letters in the ‘State’ column are used to provide a visual cue in figures as to when mode transitions are occurring. Both the interconnected and non-interconnected models follow the operation outlined in Table 8.

Table 8. Operating Regime for testing of the EVCS During Various Modes of Operation

Time (Seconds)	State	Operation	Mode
0.00	A	Wind turbines begin 'warm-up'	Standby
0.50	B	MVDC grid connected to EVCS	Standby
0.61	C	PV array ON	Power to grid
1.00	D	PV array OFF	Standby
1.15	E	EV battery 1 begins charging	Power from grid
1.20	F	PV array ON	Power from grid and PV - 1 bat chg
1.35	G	EV battery 2 begins charging	Power from grid and PV - 2 bat chg
1.75	H	PV array OFF	Power from grid – 2 bat chg
1.9	I	EV battery 2 stops charging	Power from grid – 1 bat chg

In the interconnected model, the first 0.5 seconds of simulation time is necessary for the wind turbines to ramp up to full power operation. At 0.5 seconds (state B) in both models (interconnected and non-interconnected) the MVDC grid is connected to the EVCS system, Figure 3-5, and begins to charge the input capacitor of the bidirectional DC-DC converter. In the interconnected model, the MVDC bus reaches a steady state voltage of 4.25 kV, Figure 5-1. This steady state MVDC bus voltage is used as the input voltage in the non-interconnected model to maintain congruence between simulations. As previously discussed in section 3.2.2, a pre-charge circuit was added to the bidirectional DC-DC converter. The pre-charge circuit is necessary because an uncharged capacitor is essentially a short circuit, and without a distinct pre-charge circuit the uncharged capacitor will collapse the MVDC bus. Through the addition of the resistors in series with the capacitor, the bidirectional DC-DC converters inrush current is limited. At 0.61 seconds (state C), the solar array is connected to the LVDC bus, and begins supplying 20 kW of power, this is highlighted in the power flow shown in Figure 5-3, the bidirectional DC-DC converter operating in boost mode will supply power to the MVDC grid while regulating LVDC bus voltage at 1 p.u. (800 V_{DC}) Figure 5-2, with a 0.12 p.u. overshoot. Notice that Figure 5-2 is on a different time scale, this is to provide maximum resolution over the operating range of the LVDC bus. At 1.00 seconds (state D) the PV array turns off and the EVCS enters a standby mode in which minimal power is flowing in the system; notice that during this standby period the LVDC bus voltage, Figure 5-2, is regulated to 1.0 p.u. via the damping circuit, with a 0.11 p.u. transient overshoot. At 1.15 seconds (state E) the first EV begins charging at approximately 50 kW causing a 0.09 p.u. undershoot. At 1.20 seconds (state F), the PV array turns ON supplying 20 kW of power. Once again, the bidirectional DC-DC converter regulates the LVDC bus voltage to 1.0 p.u. with a 0.07 p.u. overshoot. At 1.35 seconds (state G), the second EV begins charging at approximately 50 kW causing a 0.06 p.u. undershoot. At 1.75 seconds (state H) the PV array turns off meaning that all 100 kW of load is being supplied via the bidirectional DC-DC converter. During this period the voltage ripple of the LVDC bus reaches 6.625%. Lastly, at 1.9 seconds (state I), EV 2 quits charging. Notice, that in both the non-interconnected and the interconnected models the bidirectional DC-DC converter is able to properly regulate the LVDC bus voltage, Figure 5-2, both with and without ideal input voltage, Figure 5-1. The bidirectional DC-DC converter is able to properly provide isolation between the load step changes occurring on the LVDC bus and the MVDC bus which is shown in Figure 5-1. The only perturbation of the MVDC bus voltage caused by the EVCS is when the bidirectional DC-DC converter input side pre-charge circuit turns off; the MVDC bus has a brief drop in voltage to 0.8 p.u. which corresponds a transient undershoot of .25 p.u., Figure 5-1.

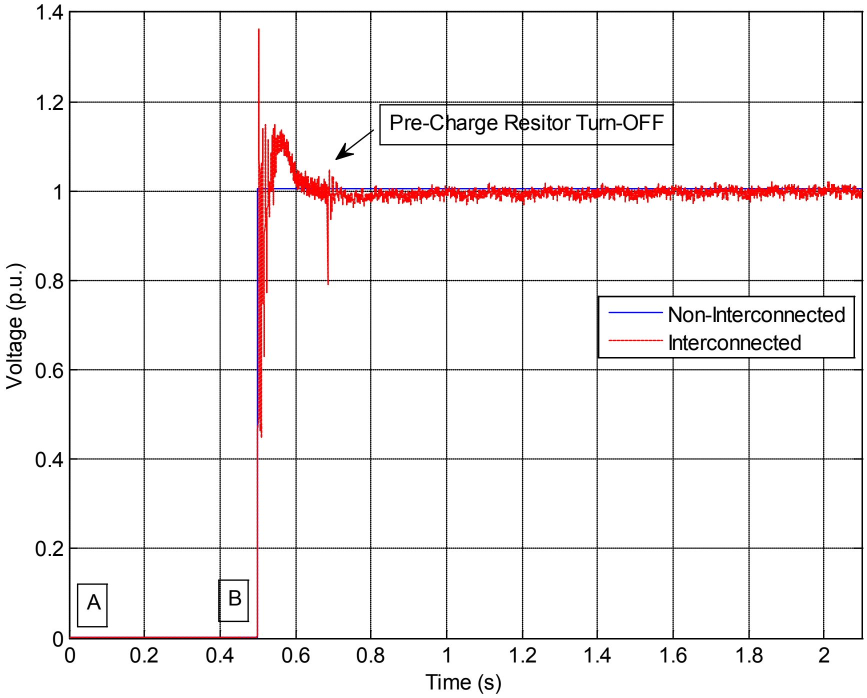

Figure 5-1. Regulated MVDC Bus Voltage

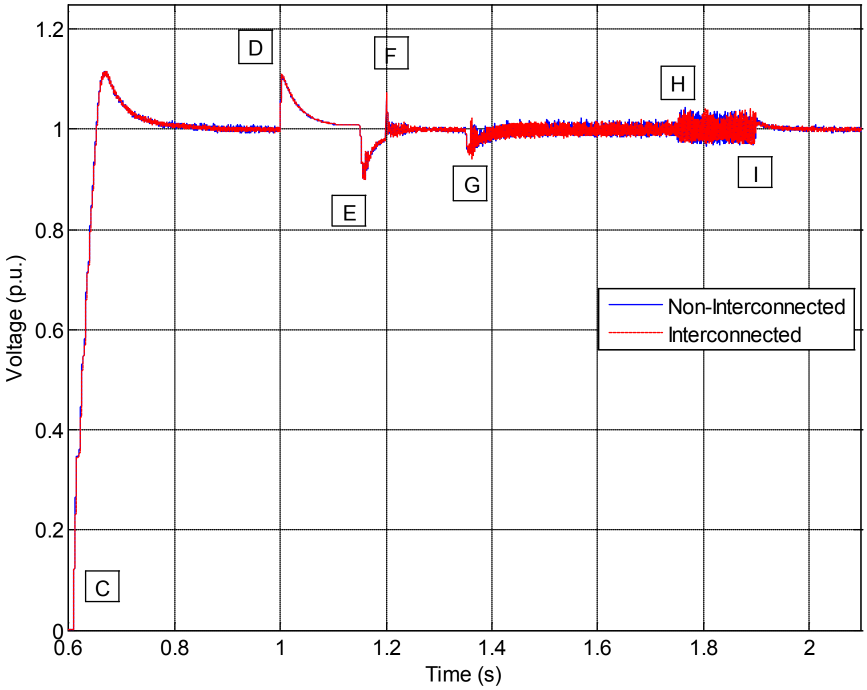

Figure 5-2. Regulated LVDC Bus Voltage

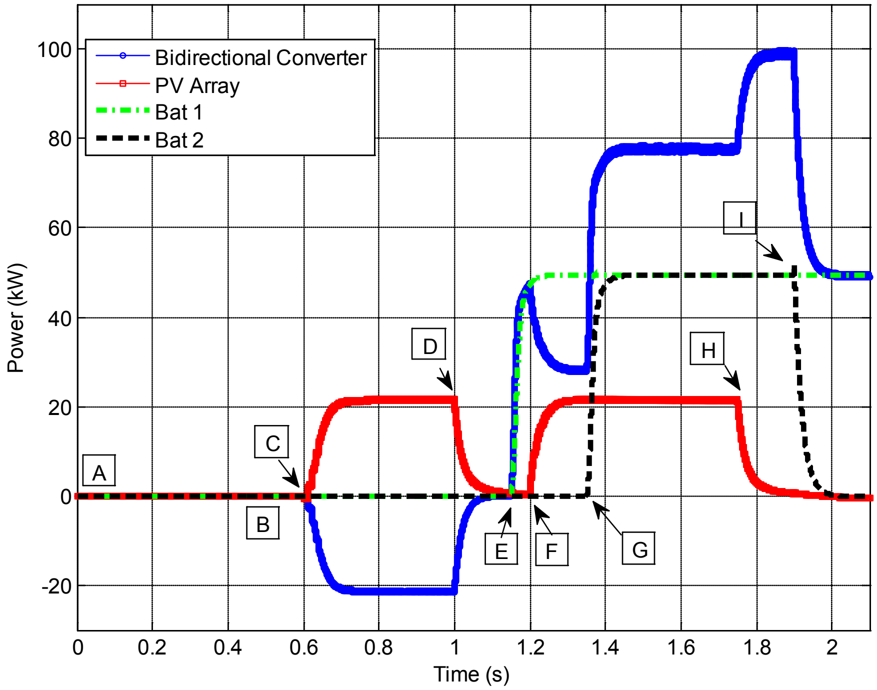

Figure 5-3. EVCS Component Absorbed and Received Power

As previously discussed, the EVCS system was tested using both an ideal voltage source (non-interconnected model) and the MVDC network (interconnected model). The MVDC network provides a regulated bus voltage of 4.25 kVDC. The MVDC network model, Figure 3-1, uses PMSG wind turbines as the source of power, which causes the MVDC bus voltage to be non-ideal and possess harmonic content. As previously shown in Figure 5-2, in both the interconnected and non-interconnected model the bidirectional DC-DC converter regulates the LVDC bus voltage to the desired value of 800 VDC. In the non-interconnected model the input current into the bidirectional DC-DC converter is highly ideal and is expected to be such, Figure 3-10. However, in the interconnected model, the input current is non-ideal. Despite the very different input currents, the bidirectional DC-DC converter properly regulates the output current in both systems, shown in Figure 5-4.

Regardless of input, the bidirectional DC-DC converter properly regulates the output voltage and current, meaning that the use of an ideal voltage source is a valid method for testing systems downstream of the converter.

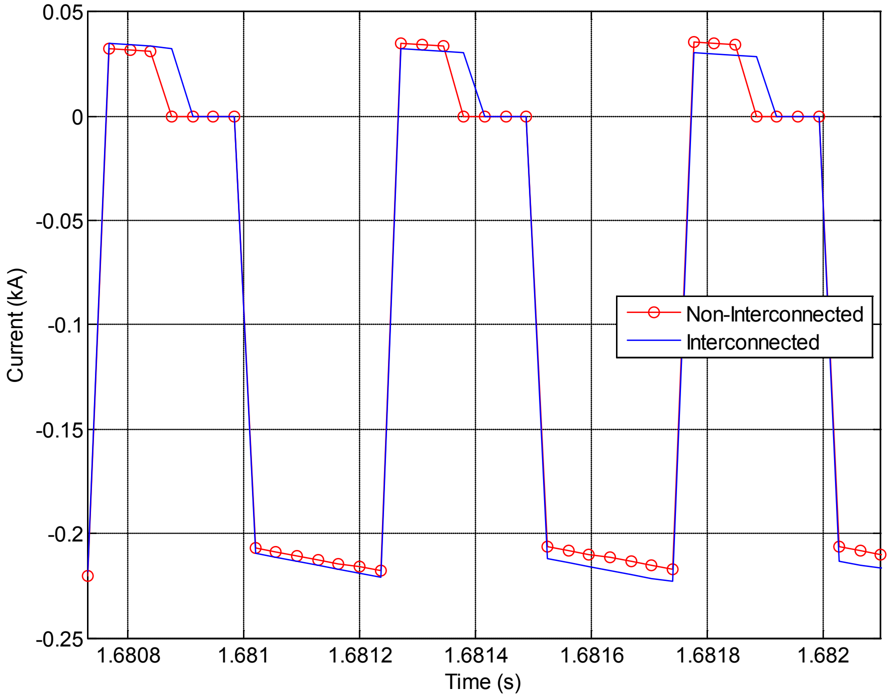

Figure 5-4. Bidirectional DC-DC Converter LVDC Bus Output Current (I_{LV})

5.2 SYNCHRONOUS BUCK CONVERTER TRANSIENT PROPAGATION

In this section the effect of a line to line fault (short circuit) at the input terminal of the electric vehicle battery during charging is investigated, in particular, the effect the synchronous buck converters power electronic switching state has on the propagation of the fault is examined. Figure 5-5 shows the EVCS system configuration at the time of the fault. All switches in the EVCS are closed and two EVs are charging at 50 kW, 20 kW of power is being supplied by the

PV array with the remaining 80 kW of power being supplied by the MVDC grid, and the system is at steady state conditions. At 0.5 seconds, a short circuit is applied across the terminals of EV battery 1. At 0.6 seconds the synchronous buck converter (Figure 3-14) stops power electronic switching with both switches open. At 0.7 seconds the fault is cleared, then at 0.8 seconds the synchronous buck converter resumes operation. The fault operation is outlined in Table 9. This simulation assumes that the battery is able to withstand a 0.2 second fault without catastrophic failure or a fuse blowing. In a real world application, the fault detection and operation stoppage of the synchronous buck converter would occur faster than 0.1 seconds.

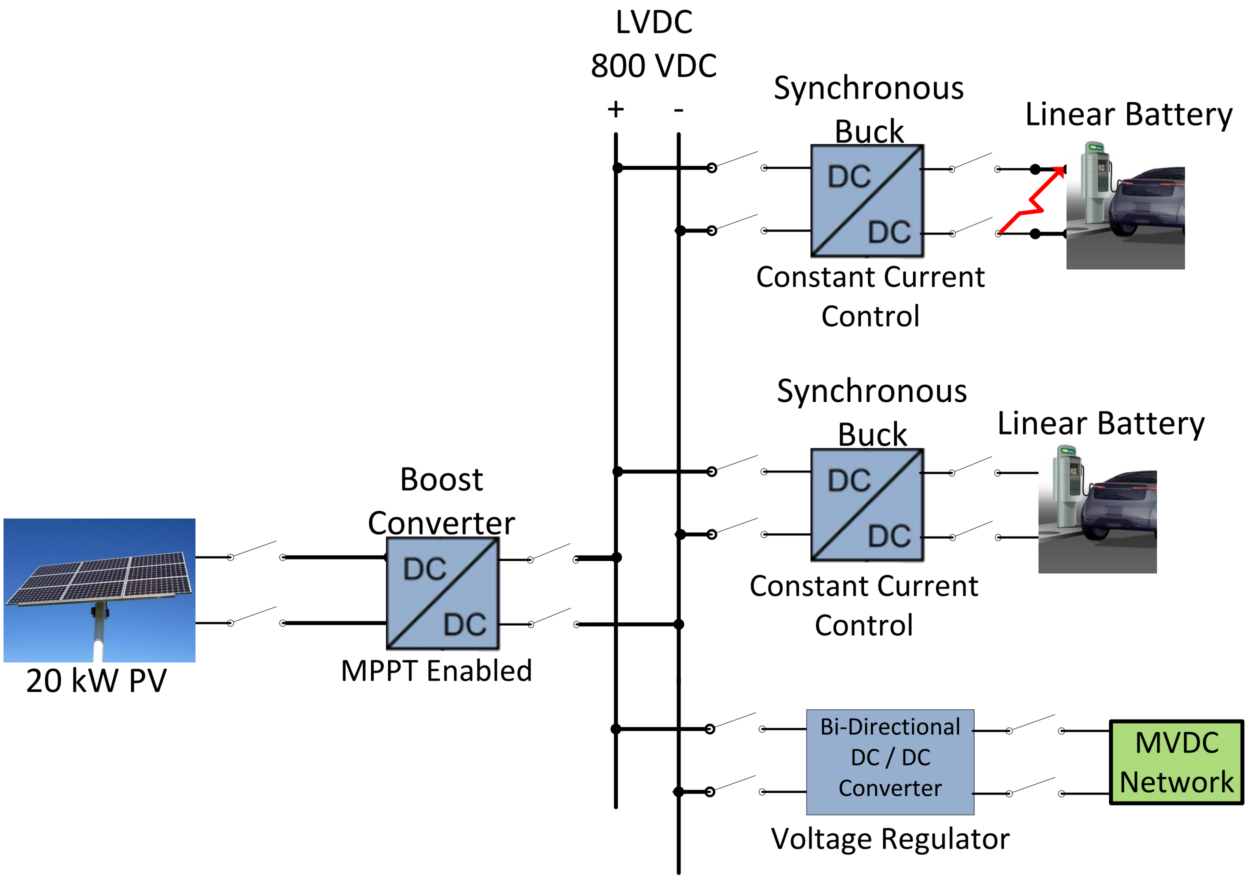

Figure 5-5. Line to Line Fault Applied to Terminal of EV During Charging

Table 9. Operating Regime for EVCS Fault Test

Time (Seconds)	Operation
0.5	Line-to-line fault on EV battery 1 terminals
0.6	Synchronous buck converter stops operation
0.7	Fault clears
0.8	Synchronous buck converter resumes operation

Figure 5-6 shows the power flow in the EVCS model at steady state conditions and during the fault. The figure is scaled to show between 0.4 and 1 second highlighting the effect of the fault on the system. When the fault begins at 0.5 seconds, the system is at steady state conditions. The fault begins at 0.5 seconds and causes the power supplied to battery 1 to drop to 37.5 kW. The grid is feeding the fault due to the fact that the synchronous buck converter utilizes constant current control, meaning the synchronous buck converter continues to provide $125A_{DC}$ of current to the battery fault at a reduced voltage. At 0.6 seconds the converter identifies the fault and stops power electronic switching, isolating fault from the LVDC bus. At 0.7 seconds the fault clears and then at 0.8 seconds the synchronous buck converter resumes steady state operation supplying 50 kW of power to the EV battery.

Figure 5-7, shows the LVDC bus and the synchronous converters output voltage during the fault. The synchronous buck converter utilizing constant current control and appropriate isolation techniques is to prevent the fault from collapsing the LVDC bus voltage so that other components can continue operation. For the duration of the fault (0.5 to 0.7 seconds) the synchronous buck converters output is reduced to 300 V from the steady state value of 400 V. The 300V output voltage is caused by the reduced battery terminal voltage during short circuit conditions, and is consistent with information found in literature [65].

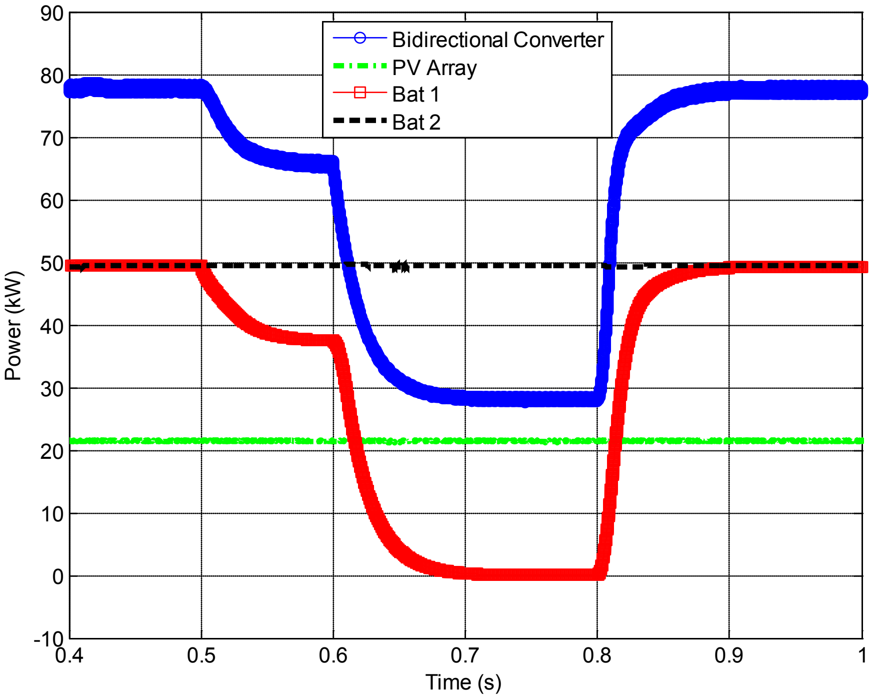

Figure 5-6. EVCS Component Absorbed and Received Power During Fault Operation

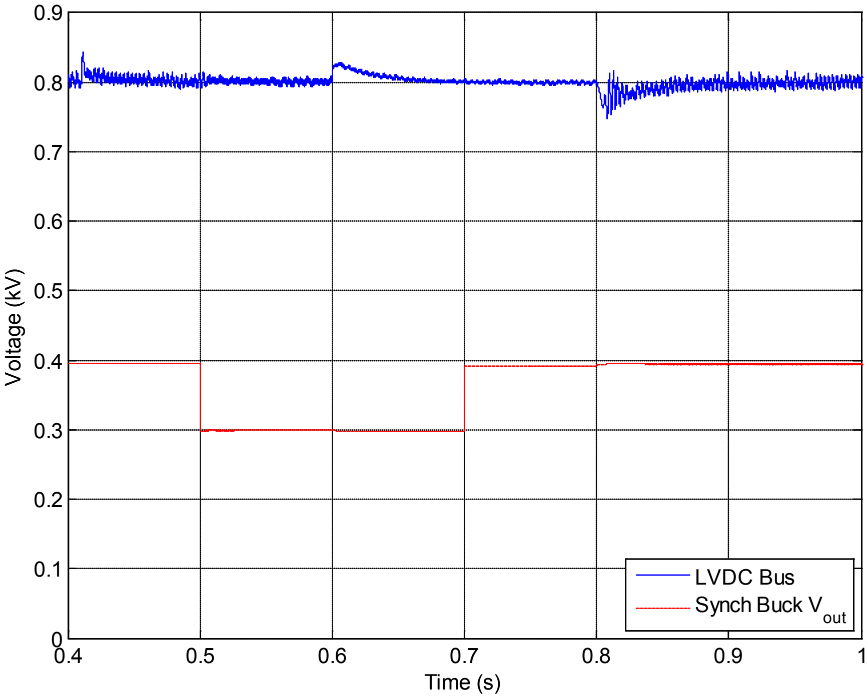

Figure 5-7. LVDC Bus Voltage and Synchronous Buck Converter Output Voltage During Fault Operation

Figure 5-8 and Figure 5-9 show the synchronous buck converters output current (I_{out}) and power (P_{out}) respectively during the fault. Notice that during the beginning of the fault between 0.5 and 0.6 seconds the synchronous buck converter continues to feed the fault by providing 125 A at a reduced power output of 37.5 kW via the constant current feedback control regulator. The use of constant current controls limits the amount of current that the LVDC bus can supply to the battery fault. At 0.6 seconds, the synchronous buck converter detects the fault and stops gating which causes the output current and power to drop to 0 A and 0 kW respectively.

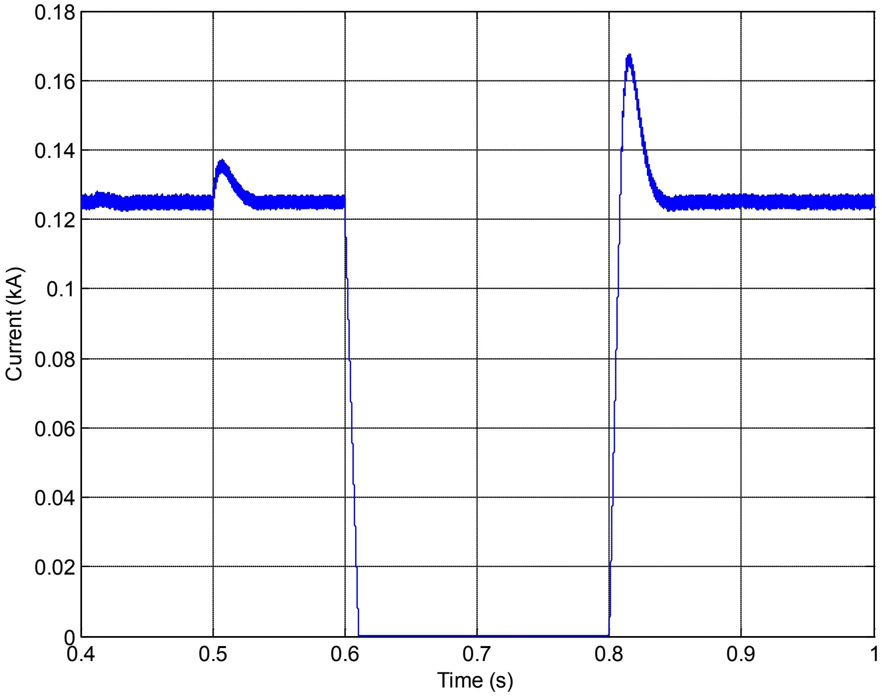

Figure 5-8. Synchronous Buck Converter Output Current During Fault Operation

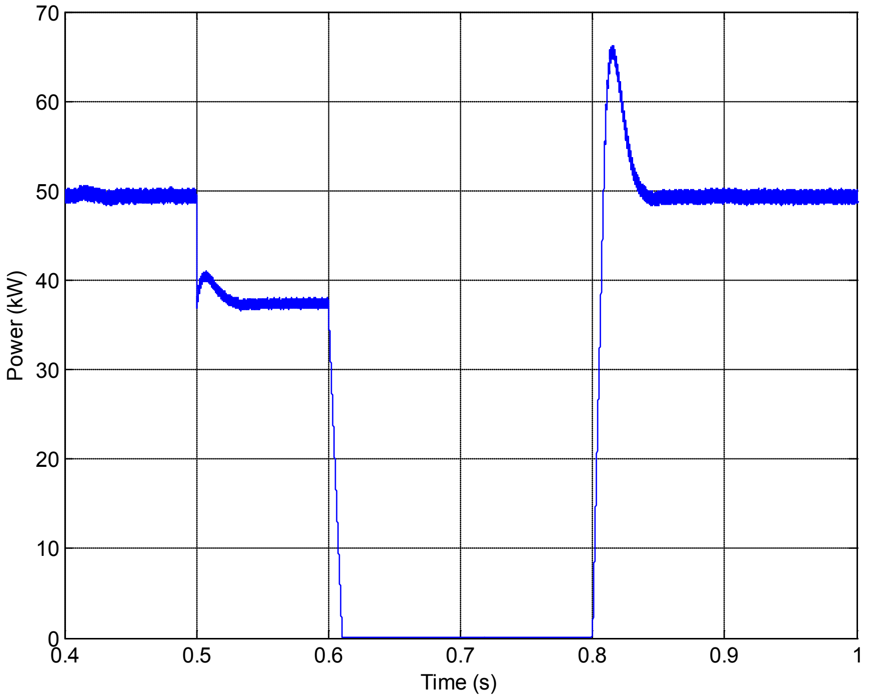

Figure 5-9. Synchronous Buck Converter Output Power During Fault Operation

Figure 5-10, shows the fault current and contributing sources during the transient. During steady state operation the synchronous buck converter output current (I_{out}) is equal to negative battery charging current ($-I_{bat}$) of 125A, as seen between 0.4 seconds and 0.5 seconds. During the short circuit the fault current (I_{Fault}) is approximately 100 times the steady state current at 11.8 kA. The battery current makes up the majority of the fault current however, between 0.5 and 0.6 seconds the synchronous buck converter contributes to the fault current. The synchronous buck converters contribution to the battery short circuit fault is limited through the use of constant current control. Between 0.6 and 0.7 seconds once the synchronous buck converter turns off the fault current is supplied by only the battery. Battery short circuit current can reach up 100 times steady state current, and does not always results in a battery terminal voltage of 0 V as described in literature [65].

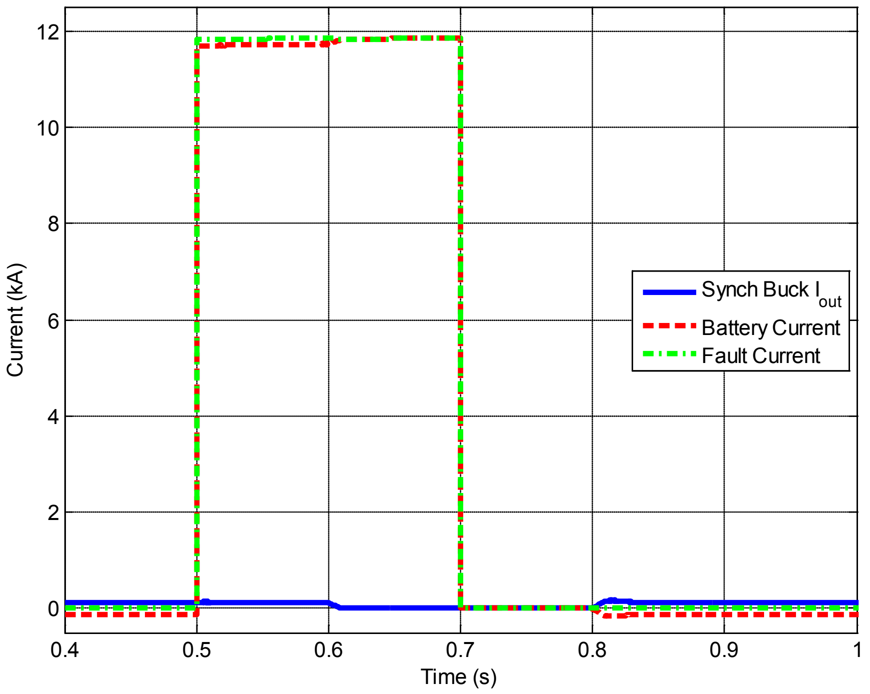

Figure 5-10. Fault Current and Contributing Sources

5.3 CCM / DCM BUCK MODE OPERATION OF BIDIRECTIONAL DC-DC CONVERTER

To this point all converter analysis performed assumed that the converter is operating in the continuous conduction mode (CCM); however, in this section the discontinuous conduction mode (DCM) operation of the bidirectional DC-DC converter is explored. Put most simply, the DCM arises when the current through the inductor reaches zero. In order for the inductor current to reach zero, the inductor current ripple (Δi_L) must be larger than the average current through the inductor (i_L). Since, the inductor current ripple is of the same order of magnitude and larger than the average inductor current, the small ripple approximation utilized in CCM analysis is no longer valid and thus traditional CCM analysis is no longer valid. The CCM/DCM boundary is proportional to the converters switching inductance (*L*) and inversly proportional to the converters switching frequency (T_S) and load resistance (R). Meaning an increase in inductance, or a decrease in switching frequency / load resistance can push a converter operating in the CCM into the DCM.

The DCM operation adds a third switching interval to each switching period (T_S). In the CCM you only have the D and the D' intervals of the switching period, and the length of both is directly controllable by setting the duty cycle (*D*). DCM operation contains *D*, D_2, and D_3 where $D_2+D_3=D'$, and the length of D_2 and D_3 are uncontrollable.

Figure 5-11, presents the inductor current for a buck converter in CCM operation. Between 0 and DT_S, the conducting device is the controlled switch (Q_1). The length of this interval of the switching period is controllable, and then the second half of the switching period between DT_S and T_S (*D'*) is the uncontrolled interval. However, in CCM operation while uncontrolled it is technically controlled since the second interval *D'* is just *1-D*.

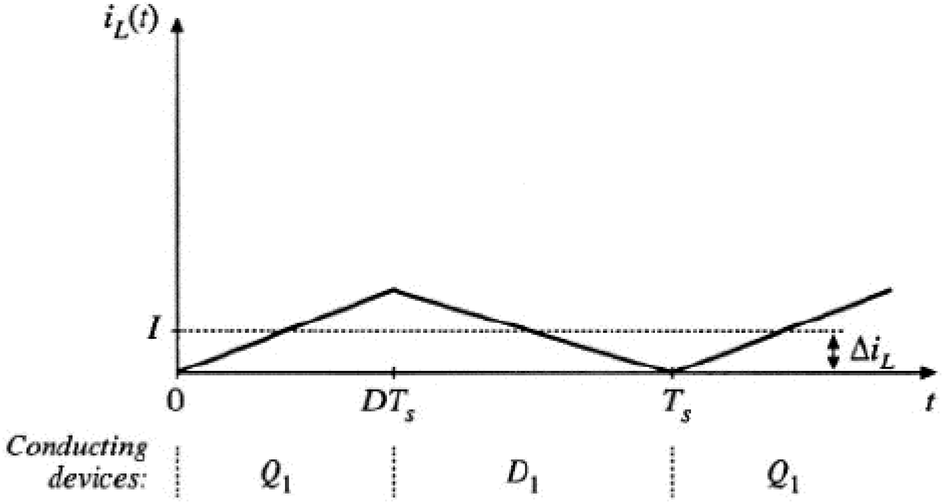

Figure 5-11. Buck Converter CCM Inductor Current Ripple [58]

Figure 5-12, displays the buck converter inductor current during DCM operation. Notice the addition of the third interval to the switching period D_3T_S. This occurs when the inductor current reaches zero. During the third interval D_3T_S all conducting devices are off. When comparing Figure 5-12 and Figure 5-11 it should be noted that in the DCM the average inductor current I is lower than in CCM mode. This is one of the benefits of DCM operation.

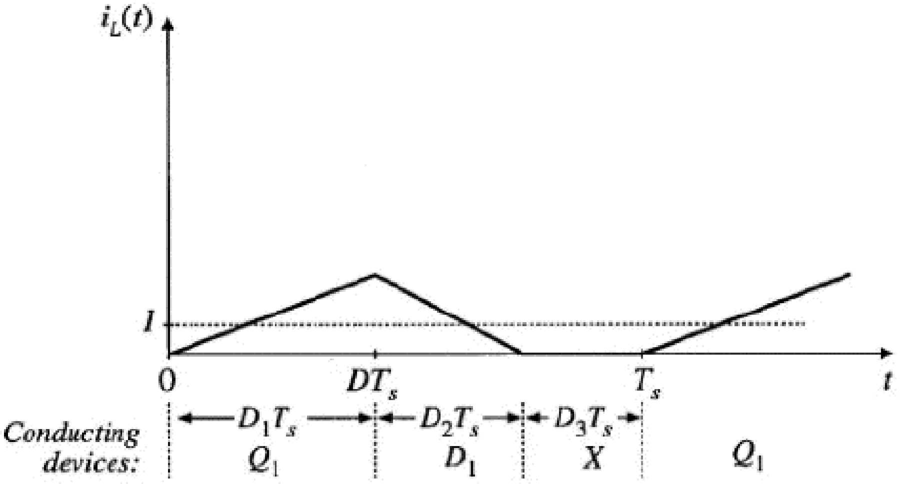

Figure 5-12. Buck Converter DCM Inductor Current Ripple [58]

In the case of the bidirectional DC-DC converter operating within the non-interconnected model, the DCM-CCM operation is most easily controlled by the varying of the switching frequency (*fs*). When the *fs* is set to 2 kHz as it is normally, the converter operates in the CCM; however, changing the *fs* to 1 kHz forces it into DCM operation. Figure 5-13 shows the current I_L in the choke inductor which is the main energy storage component in the bidirectional DC-DC converter. The solid blue line shows I_L at a switching frequency (*fs*) of 2 kHz. The average value of the current is negative because the measurement defines the positive current direction as 'into the converter.' The dashed line shows the inductor current at a switching frequency of 1 kHz. At *fs* equal to 1 kHz the converter is in DCM operation, as illustrated by I_L reaching 0 A_{DC}.

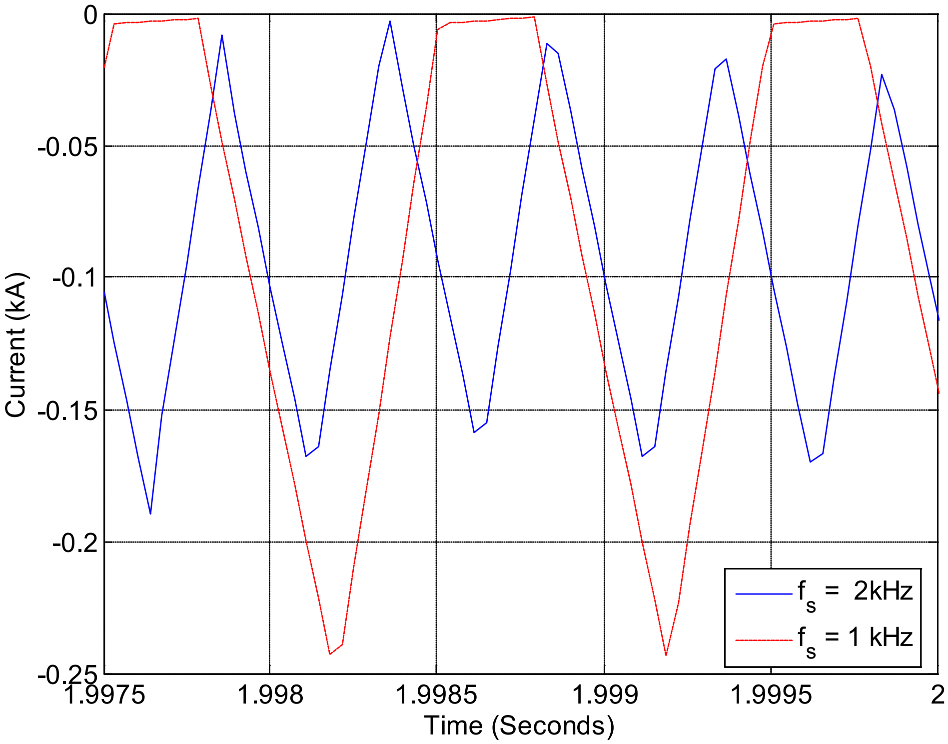

Figure 5-13. Choke Inductor Current (I_L) at Various f_S

Figure 5-14, shows the transformer primary voltage (E_p) at a switching frequency of 2 kHz (solid blue line) and 1 kHz (dashed red line). At 2 kHz the converter is in CCM and the transformer primary has three voltage levels, +V, 0 and -V. In DCM operation at a switching frequency of 1 kHz, the transformer primary voltage has five levels, +V, 0, -½V, -V, and +½V. The +/- ½V occur when the inductor current (I_L) reaches 0 during the uncontrolled D_2 interval of operation. It should be noted that in DCM operation the bidirectional DC-DC converter still operates and regulates voltage properly.

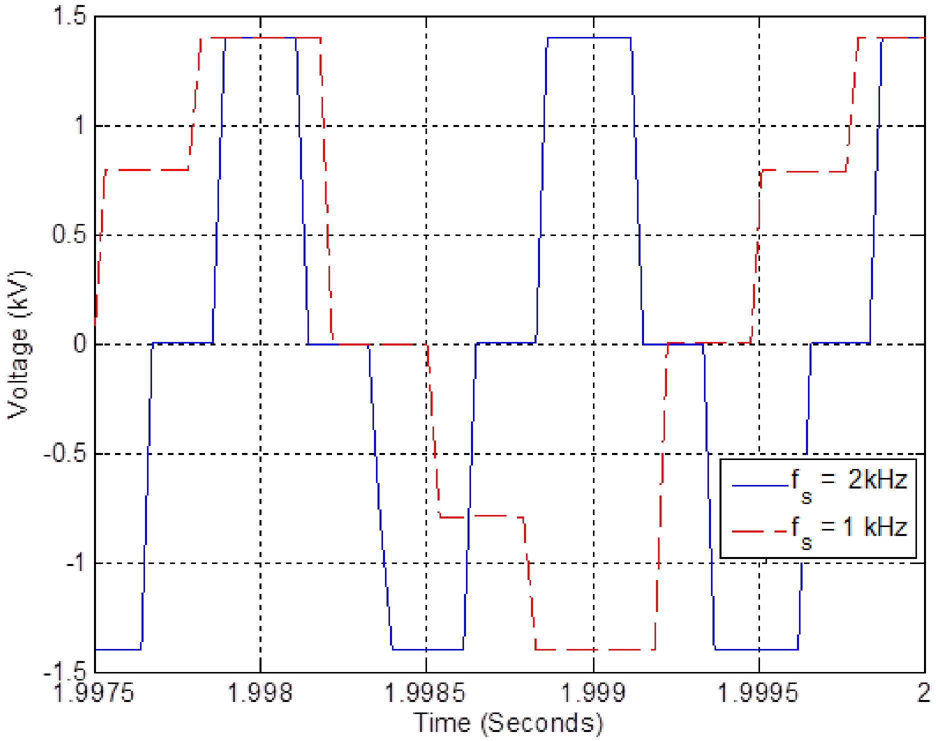

Figure 5-14. Transformer Primary Voltage (E_P) at Various f_S

6.0 CONCLUSIONS AND FUTURE WORK

At the turn of the 20th century AC won the war of the currents for all the right reasons at the time; however, at the turn of the 21st century with advances in power electronic conversion devices, increased population densities, distribution networks at maximum capacity, increasing fuel prices, and a need for increased reliability; perhaps the time is right to rethink AC versus DC? This thesis presented a common DC bus electric vehicle charging station architecture and examined its interaction when connected to a medium voltage DC network interconnecting renewable generation and next generation end use loads. The EVCS is a unique application in that it can be generalized to represent many common systems. It contains, load side generation (PV), storage (EVs), and high power loads (Charging EVs).

A literature survey of grid level battery energy storage systems and an analysis of the price, penetration and general computer modeling of battery energy storage systems has been provided. A better understanding of battery energy storage systems is necessary in order to properly understand the electric vehicle market and the major hurdle it must overcome, reducing battery cost to a point where it makes economic sense for the average consumer to own an electric vehicle.

A literature survey of state of the art power electric converters for use within the medium voltage DC and electric vehicle charging station networks have been presented. With this literature survey, comes the theory and design of the various devices and associated control for use in simulation.

The operation of the EVCS when interconnected with the MVDC network and when powered via an ideal voltage source was compared. The operation of the EVCS was identical regardless of the source; due to the isolation capabilities of the bidirectional DC-DC converter. Through the use of limited power sources in the MVDC network case limitations of the bidirectional DC-DC converter were identified. In particular, the need to add a pre-charge circuit was highlighted.

The ability of the synchronous buck converter to isolate faults in next generation DC power systems was explored. A battery short circuit test was performed during full power charging of an electric vehicle. Due to the nature of the battery short circuit and the constant current control utilized by the battery charger (synchronous buck converter) the EVCS provided minimal current to the battery fault; however, it still contributed. In order to clear the appropriate metering and controls are necessary to detect battery faults and stop operation of the battery charger isolating the battery fault from the rest of the EVCS.

Through the research presented in this thesis, future work in EVCS and MVDC development is definitely necessary and valuable. Proposed future work initiatives include:

- System operation standards to create a ‘plug and play’ grid of standalone power electronic converters that operate seamlessly and autonomously in all modes of operation.
- Identification of ideal bus voltage levels for optimal system performance.
- Development of advanced battery technologies to reduce cost and increase performance and life time.

- Determination of efficiency and reliability benefits of DC networks over comparable AC networks.
- Investigation of MVDC network architecture as component in a future intermeshed AC/DC distribution network.

BIBLIOGRAPHY

[1] G. F. Reed, P. A. Philip, A. Barchowsky, C. J. Lippert, and A. R. Sparacino, "Sample survey of smart grid approaches and technology gap analysis," in *Innovative Smart Grid Technologies Conference Europe (ISGT Europe), 2010 IEEE PES*, 2010, pp. 1-10.

[2] J. L. Arrillaga, Y.H. ; Watson, N.R., *Flexible Power Transmission: The HVDC Options*: John Wiley & Sons Ltd, 2007.

[3] T. Ericsen, "Engineering "Total Electric Ship"," in *Petroleum and Chemical Industry Technical Conference, 2007. PCIC '07. IEEE*, 2007, pp. 1-6.

[4] G. F. Reed, B. M. Grainger, A. R. Sparacino, R. J. Kerestes, and M. J. Korytowski, "Advancements in medium voltage DC architecture development with applications for powering electric vehicle charging stations," in Energytech, 2012 IEEE, 2012, pp. 1-8.

[5] U. S. E. I. Administration, "Annual Energy Outlook 2011 with projections to 2035," 2011.

[6] D. o. Energy, "One Million Electric Veicles by 2015 - February 2011 Status Report," 2011.

[7] L. Dickerman and J. Harrison, "A New Car, a New Grid," *Power and Energy Magazine, IEEE,* vol. 8, pp. 55-61, 2010.

[8] E. Taylor, "Comparative Analysis of Datacenter Electrical Distribution Architectures," Masters of Science, Electrical and Computer Engineering, University of Pittsburgh, 2012.

[9] E. P. R. I. (EPRI), "Electricity Energy Storage Technology Options. A White Paper Primer on Applications, Costs and Benefits," 2010.

[10] S. Vazquez, S. M. Lukic, E. Galvan, L. G. Franquelo, and J. M. Carrasco, "Energy Storage Systems for Transport and Grid Applications," *Industrial Electronics, IEEE Transactions on,* vol. 57, pp. 3881-3895, 2010.

[11] I. KEMA, "ES-Selectred^{TM} - A Decision-Support Tool," I. KEMA, Ed., ed, 2011.

[12] D. Chen, S. Wang, M. Xiao, and Y. Meng, "Preparation and properties of sulfonated poly(fluorenyl ether ketone) membrane for vanadium redox flow battery application," *Journal of Power Sources,* vol. 195, pp. 2089-2095, 2010.

[13] T. R. Crompton, *Battery Reference Book*, Third ed. Woburn: Newnews, 2000.

[14] E. P. R. I. (EPRI), "Chino Battery Energy Storage Power Plant: First Year of Operation," 1992.

[15] D. H. B. Daoughty, P.C.; Akhil, A.A. (2010) Batteries for Large-Scale Stationary Electrical Energy Storage. *The Electrochemical Society Interface*.

[16] A. Esmaili and A. Nasiri, "Energy storage for short-term and long-term wind energy support," in *IECON 2010 - 36th Annual Conference on IEEE Industrial Electronics Society*, 2010, pp. 3281-3286.

[17] E. P. R. I. (EPRI), "Golden Valley Electrical Association Battery Energy Storage System," 2010.

[18] L. NGK Insulators. (September 14, 2011). *NAS Batteries: Principle*. Available: http://www.ngk.co.jp/english/products/power/nas/principle/index.html

[19] E. P. R. I. (EPRI), "AEP Sodium-Sulfur (NAS) Battery Demonstration," 2005.

[20] (2009, April 14, 2011). *NGK Insulators Sodium Sulfur Batteries for Large Scale Grid Energy Storage*. Available: http://energystoragenews.com/NGK%20Insulators%20Sodium%20Sulfur%20Batteries%20for%20Large%20Scale%20Grid%20Energy%20Storage.html

[21] Y. Bo, Y. Makarov, J. Desteese, V. Viswanathan, P. Nyeng, B. McManus, and J. Pease, "On the use of energy storage technologies for regulation services in electric power systems with significant penetration of wind energy," in *Electricity Market, 2008. EEM 2008. 5th International Conference on European*, 2008, pp. 1-6.

[22] W. Zhaoyin, "Study on Energy Storage Technology of Sodium Sulfur Battery and it's Application in Power System," in *Power System Technology, 2006. PowerCon 2006. International Conference on*, 2006, pp. 1-4.

[23] B. Tamyurek, D. K. Nichols, and O. Demirci, "The NAS battery: a multifunction energy storage system," in *Power Engineering Society General Meeting, 2003, IEEE*, 2003, p. 1996 Vol. 4.

[24] A. Nourai, "Installation of the First Distributed Energy Storage System (DESS) at American Electric Power (AEP)," S. N. Laboratories, Ed., ed, 2007.

[25] A. Bito, "Overview of the sodium-sulfur battery for the IEEE Stationary Battery Committee," in *Power Engineering Society General Meeting, 2005. IEEE*, 2005, pp. 1232-1235 Vol. 2.

[26] M. B. Yoshio, R.J.; and A. Kozawa, *Lithium-Ion Batteries: Science and Technologies*: Springer, 2009.

[27] S. X. Chen, K. J. Tseng, and S. S. Choi, "Modeling of Lithium-Ion Battery for Energy Storage System Simulation," in *Power and Energy Engineering Conference, 2009. APPEEC 2009. Asia-Pacific*, 2009, pp. 1-4.

[28] E. A. Committee, "Energy Storage Activities in hte United States Electricity Grid," United States Department of Energy2011.

[29] D. Rakhmatov, S. Vrudhula, and D. A. Wallach, "A model for battery lifetime analysis for organizing applications on a pocket computer," *Very Large Scale Integration (VLSI) Systems, IEEE Transactions on,* vol. 11, pp. 1019-1030, 2003.

[30] R. Peng and M. Pedram, "An analytical model for predicting the remaining battery capacity of lithium-ion batteries," in *Design, Automation and Test in Europe Conference and Exhibition, 2003*, 2003, pp. 1148-1149.

[31] P. E. Pascoe and A. H. Anbuky, "VRLA battery discharge reserve time estimation," *Power Electronics, IEEE Transactions on,* vol. 19, pp. 1515-1522, 2004.

[32] C. Min and G. A. Rincon-Mora, "Accurate electrical battery model capable of predicting runtime and I-V performance," *Energy Conversion, IEEE Transactions on,* vol. 21, pp. 504-511, 2006.

[33] L. Song and J. W. Evans, "Electrochemical-Thermal Model of Lithium Polymer Batteries," *Journal of The Electrochemical Society,* vol. 147, pp. 2086-2095, 2000.

[34] P. M. Gomadam, J. W. Weidner, R. A. Dougal, and R. E. White, "Mathematical modeling of lithium-ion and nickel battery systems," *Journal of Power Sources,* vol. 110, pp. 267-284, 2002.

[35] D. W. Dees, V. S. Battaglia, and A. Bélanger, "Electrochemical modeling of lithium polymer batteries," *Journal of Power Sources,* vol. 110, pp. 310-320, 2002.

[36] S. Barsali and M. Ceraolo, "Dynamical models of lead-acid batteries: implementation issues," *Energy Conversion, IEEE Transactions on,* vol. 17, pp. 16-23, 2002.

[37] M. Ceraolo, "New dynamical models of lead-acid batteries," *Power Systems, IEEE Transactions on,* vol. 15, pp. 1184-1190, 2000.

[38] K. Yoon-Ho and H. Hoi-Doo, "Design of interface circuits with electrical battery models," *Industrial Electronics, IEEE Transactions on,* vol. 44, pp. 81-86, 1997.

[39] Z. F. Hussien and L. W. M. Cheung, M. F. Ismail, A. B., "Modeling of Sodium Sulfur Battery for Power System Applications," 2007.

[40] Z. Chen, M. Ding, and J. Su, "Modeling and control for large capacity battery energy storage system," in *Electric Utility Deregulation and Restructuring and Power Technologies (DRPT), 2011 4th International Conference on*, 2011, pp. 1429-1436.

[41] D. Cadar, D. Petreus, I. Ciocan, and P. Dobra, "An improvement on empirical modelling of the batteries," in *Electronics Technology, 2009. ISSE 2009. 32nd International Spring Seminar on*, 2009, pp. 1-6.

[42] J. R. Bumby, P. H. Clarke, and I. Forster, "Computer modelling of the automotive energy requirements for internal combustion engine and battery electric-powered vehicles," *Physical Science, Measurement and Instrumentation, Management and Education - Reviews, IEE Proceedings A,* vol. 132, pp. 265-279, 1985.

[43] B. M. Grainger, "Medium Voltage DC Network Modeling and Analysis with Preliminary Studies for Optimized Converter Configuration Through PSCAD Simulation Environment," ed, 2011.

[44] S. J. Chapman, *Electric Machinery Fundamentals*, 4 ed. New York: McGraw Hill, 2005.

[45] M. de Freige, M. Ross, G. Joos, and M. Dubois, "Power & energy ratings optimization in a fast-charging station for PHEV batteries," in *Electric Machines & Drives Conference (IEMDC), 2011 IEEE International*, 2011, pp. 486-489.

[46] G. Joos, M. de Freige, and M. Dubois, "Design and simulation of a fast charging station for PHEV/EV batteries," in *Electric Power and Energy Conference (EPEC), 2010 IEEE*, 2010, pp. 1-5.

[47] M. de Freige, G. Joos, and M. Dubois, "Energy management & scheduling in a fast charging station for PHEV batteries," in *Power and Energy Society General Meeting, 2011 IEEE*, 2011, pp. 1-5.

[48] I.-Y. Chung, W. Liu, K. Schoder, and D. A. Cartes, "Integration of a bi-directional DC–DC converter model into a real-time system simulation of a shipboard medium voltage DC system," *Electric Power Systems Research,* vol. 81, pp. 1051-1059, 2011.

[49] D. Dong, "Ac-dc Bus-interface Bi-directional Converters in Renewable Energy Systems," Ph.D., Electrical Engineering, Virginia Polytechnic Institute and State University, Blacksburg, 2012.

[50] M. E. Baran and N. R. Mahajan, "DC distribution for industrial systems: opportunities and challenges," *Industry Applications, IEEE Transactions on,* vol. 39, pp. 1596-1601, 2003.

[51] D. Salomonsson, L. Soder, and A. Sannino, "Protection of Low-Voltage DC Microgrids," *Power Delivery, IEEE Transactions on,* vol. 24, pp. 1045-1053, 2009.

[52] C. S. CCJ Digital. (2011). *Eaton Research Facility Adds EV Charging Stations*. Available: http://www.ccjdigital.com/eaton-research-facility-adds-ev-charging-stations/

[53] ABB. *Electric Vehicle Infrastructure - DC Fast Charge Station*. Available: http://www04.abb.com/global/seitp/seitp202.nsf /0/ece78ade16a31d2ec125784800406d01/$file/DC+Fast+Charge+Station+100211.pdf

[54] M. C. Kisacikoglu, B. Ozpineci, and L. M. Tolbert, "Reactive power operation analysis of a single-phase EV/PHEV bidirectional battery charger," in *Power Electronics and ECCE Asia (ICPE & ECCE), 2011 IEEE 8th International Conference on*, 2011, pp. 585-592.

[55] S. Inoue and H. Akagi, "A Bi-Directional DC/DC Converter for an Energy Storage System," in *Applied Power Electronics Conference, APEC 2007 - Twenty Second Annual IEEE*, 2007, pp. 761-767.

[56] S. Inoue and H. Akagi, "A Bi-Directional Isolated DC/DC Converter as a Core Circuit of the Next-Generation Medium-Voltage Power Conversion System," in *Power Electronics Specialists Conference, 2006. PESC '06. 37th IEEE*, 2006, pp. 1-7.

[57] C. Il-Yop, L. Wenxin, M. Andrus, K. Schoder, L. Siyu, D. A. Cartes, and M. Steurer, "Integration of a bi-directional dc-dc converter model into a large-scale system simulation of a shipboard MVDC power system," in *Electric Ship Technologies Symposium, 2009. ESTS 2009. IEEE*, 2009, pp. 318-325.

[58] R. M. Erickson, D., *Fundamentals of Power Electronics*, 2 ed. New York, 2004.

[59] Q. Zhao and G. Stojcic, "Characterization of Cdv/dt induced power loss in synchronous buck DC-DC converters," in *Applied Power Electronics Conference and Exposition, 2004. APEC '04. Nineteenth Annual IEEE*, 2004, pp. 292-297 Vol.1.

[60] J. Traube, L. Fenglong, and D. Maksimovic, "Electric vehicle DC charger integrated within a photovoltaic power system," in *Applied Power Electronics Conference and Exposition (APEC), 2012 Twenty-Seventh Annual IEEE*, 2012, pp. 352-358.

[61] Kyocera, "KC125G - High Efficiency Multicrystal Photovolatic Module - Data Sheet," ed, 2009, pp. 1-4.

[62] V. Salas, E. Olías, A. Barrado, and A. Lázaro, "Review of the maximum power point tracking algorithms for stand-alone photovoltaic systems," *Solar Energy Materials and Solar Cells,* vol. 90, pp. 1555-1578, 2006.

[63] L. Bangyin, D. Shanxu, L. Fei, and X. Pengwei, "Analysis and Improvement of Maximum Power Point Tracking Algorithm Based on Incremental Conductance Method for Photovoltaic Array," in *Power Electronics and Drive Systems, 2007. PEDS '07. 7th International Conference on*, 2007, pp. 637-641.

[64] Z. Minxin, Q. Bojin, and D. Xiaowei, "Dynamic model for characteristics of Li-ion battery on electric vehicle," in *Industrial Electronics and Applications, 2009. ICIEA 2009. 4th IEEE Conference on*, 2009, pp. 2867-2871.

[65] C. Kallfab, C. Hoch, A. Hilger, and I. Manke, "Short-circuit and overcharge behaviour of some lithium ion batteries," in *Systems, Signals and Devices (SSD), 2012 9th International Multi-Conference on*, 2012, pp. 1-5.